Microwave and Far-infrared Spectroscopy of Water-containing, Hydrogen-bonded Dimers: Vibrational, Rotational, and Tunneling Dynamics

Thesis by

Paul Alan Stockman

In Partial Fulfillment of the Requirements

for the Degree of

Doctor of Philosophy

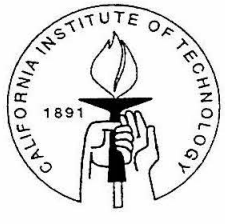

California Institute of Technology

Pasadena, California

1996

(Submitted 28 September 1995)

Acknowledgements

Writing this thesis has been an inherently solitary and self-reflective time for me, and it is refreshing at the end of this process to recall the individuals who have had much-appreciated, positive and supportive roles in my education here at Caltech.

Foremost among these is my advisor Geoff Blake, whose contagious enthusiam for all science and limitless supply of ideas and encouragement are well-balanced by a healthy respect for self-achievement and individuality. Geoff never failed to offer sound, insightful advice when requested and was benignly absent when I needed to think for myself. He has also served as a human spectroscopic data base, rattling off transitions to six or seven figures, and has expanded my graduate education to include astronomy, geology, and biology among others. Beyond this, he has had a genuine concern for my general education and well-being, and certainly will serve as a role model in the years to come.

I owe much to my friend, labmate, and far-infrared co-mechanic of the last six years Sakae Suzuki. He has unselfishly shared the responsiblity and effort necessary to maintain the spectrometer and other equipment in the lab (and on the roof) as well as the experimental time available to us whenever things were working. Sakae's unflaggingly positive attitude and good company have made even the most arduous and daunting repair tasks enjoyable, and he was ever-patient to remind me that the hammer is the final, not the first, resort.

Much of my practical training in spectroscopy came from the first two years I spent working with Roger Bumgarner. His careful and concerned tutelage (including a tour of the lab with invoices in hand, explaining how much everything cost) was responsible for bringing me quickly up to speed in the field. Much of Roger's hard work and skill remains with the group in the form of computer programs used for data analysis and instrumental control—these contributions have been oft' used and appreciated by me, and have also been a helpful model in my own programming. Peter

Green was also willingly available to me during those first two years, answering many scientific and hardware questions, as well as sharing his experiences and photographs of high-altitude locales which I, sensibly, will never visit. Roger, along with Peter and summer student Janet Bowen, collected most of the rotational-tunneling data for Chapter 3, and Roger was also responsible for generating the corresponding *ab initio* surfaces.

My other groupmates—Pin Chen, Dave Rodham, and Sheng Wu—have contributed to broadening my perspective in chemical physics beyond the realm of the far-infrared. They have freely shared equipment and advice, and have made the Blake group an interesting place to work. Our group secretary Jan Haskell has provided gracious help in overcoming what small bureaucracy exists at Caltech. Equally important, she has been the person most able to answer the questions, "Where's Geoff; when is he coming back?"

Our group has maintained a collaborative relationship with several staff scientists at NIST in Gaithersburg, MD, and they have also kindly served as additional mentors to me. Frank Lovas and Rick Suenram are consumate spectroscopists whose long tenures in the field of weakly bound complexes have manifested themselves to me in a wealth of practical advice. Frank and Rick have also directly contributed to much of the seminal microwave work upon which our FIR studies built. Gerry Fraser has given helpful and experienced advice, particularly about the treatments of internal rotations. Finally, Jon Hougen has served as an instructor in PI group theory and has instilled in several of us an enthusiasm and insight for an otherwise esoteric field.

The work which supports this thesis has a large practical component that often goes unmentioned in the published reports. The staff at Caltech are truly student-oriented, and have enriched my time here and taught me valuable skills. I would specifically like to thank the staff of the chemistry machine shop—Guy Duremberg, Ray Garcia, Tony Stark, and more recently Mike Roy—who have taught me everything I know about machining and have also provided quick and professional service for the projects which passed through their skillful hands. Our glassblower, Rick Gerhart, has also provided a quick and professional response to the myriad of requests

asked of him. Tom Dunn has been a patient and insightful resource for my semiliterate electronic questions, and has often loaned me much-needed equipment. Finally, I would like to thank Dian Buchness for consistently serving as the chemistry graduate student's best friend. Her organization and thoughtfulness have virtually eliminated any hassle associated with being a graduate student here for me, and she has added a much-appreciated air of pleasantness to any "official" business.

My research at Caltech has been funded through grants and fellowships provided to my advisor from both public and private sources. These include the Beckman Institute of Caltech, the National Science Foundation, the Sloan Foundation, the Packard Foundation, and the Donors of the Petroleum Research Fund, which I gratefully acknowledge. I am increasingly aware of the opportunities which have been afforded me, in part because of my nationality, and I am very grateful for the priorty the US government has given to public education and to scientific research and training and for the ability of its citizens to support it through their tax dollars.

Finally, I am thankful for the tremendous amount of personal support and encouragement given to me during my graduate study and throughout my formal education. My parents, Bruce and Peggy Stockman, have provided me with educational opportunities and experiences ever since I can remember, often beyond their means, and always invested with their love and support. My in-laws, Dick and Harriet Zook, have also offered their unconditional support during my graduate study and given welcome respites of familiy hospitality. My wife Kirsten has been my mainstay for my entire adult life, a constant friend, and a supportive partner. Along with our son Hans, she has provided me with all of the love and encouragement I have ever needed, and it is to her that I lovingly dedicate this thesis.

Abstract

Microwave and far-infrared high-resolution spectroscopies have been used to investigate the vibrational, rotational, and tunneling dynamics of water-containing, hydrogen-bonded dimers, towards the goal of converting the recorded spectra into intermolecular potential energy surfaces (IPSs). Such intermolecular interactions are the basis for much of biological structure and function, as well as reaction and solution dynamics, and a comprehensive set of key IPSs can form the basis set for molecular modeling of these complex phenomena. Specifically studied in this work are the following dimers and some of their isotopomers: $N_2 \cdots H_2O$, $OC \cdots H_2O$, $H_3N \cdots H_2O$, $CH_3OH \cdots H_2O$. These dimers constitute a series of increasing binding energy, dynamical complexity, and chemical and biological importance.

The dimers of water with isoelectronic N_2 and CO are treated jointly because of their similar properties and level of study. The b-type $K = 0 \rightarrow 1$ rotational spectra for $N_2 \cdots H_2O$ and $OC \cdots H_2O$, as well as isotopomers containing HOD, D_2O, and ^{13}CO, were recorded between 325 and 661 GHz, and measurements were also extended for the a-type spectra of the $N_2 \cdots H_2O$ and $OC \cdots H_2O$ isotopomers. Each rotational transition was split by the effects of large-amplitude tunneling of the hydrogen and nitrogen nuclei, and the number of tunneling components corresponded with that predicted from PI theory. After the effects of tunneling had been removed from the rotational constants, the structures of the two different complexes were fit to the rotational moments of inertia. These structures correspond to a nearly linear hydrogen bond and alignment of heavy atoms. The tunneling selection rules for $OC \cdots H_2O$ were confirmed to be "top-to-bottom, bottom-to-top,"and the tunneling splittings were obtained from the difference in the A_{eff} rotational constants. Using two- and three-term Fourier expansions, the one-dimensional tunneling coordinate was fit to the tunneling splittings for $OC \cdots H_2O$ and $OC \cdots D_2O$. *Ab initio* surfaces are used both to visualize the tunneling modes and as a basis for normal mode anal-

yses. A reasonable and justified normal mode separation is presented, with the five intermolecular degrees of freedom separated into geared and anti-geared in-plane and out-of-plane motions of the the subunits as well as the intermolecular stretch. Finally, partial VRT spectra for both complexes recorded between 42 and 53 cm^{-1} are presented and preliminarily assigned to the in-plane geared motion.

Microwave and far-infrared spectra of the $H_3N\cdots H_2O$ dimer were recorded from 36 to 86 GHz and 520 to 800 GHz. The a-type pure rotational microwave data extend the previous $m = 0, K = 0$ A-symmetry manifold measurements of Herbine and Dyke [*J. Chem. Phys.* **83**, 3768 (1980)] to higher frequency and also provide an additional set of microwave transitions in the $mK = +1$ E symmetry manifold. Two sets of five b-type rotation-tunneling bands, one set shifted from the other by an approximately constant 113 MHz, were observed in the far-infrared. The splitting into two sets arises from water tunneling, while the overall band structure is due to internal rotation of the ammonia top. Non-linear least-squares fits to an internal rotor Hamiltonian provided rotational constants, and an estimation of V_3=10.5 $\pm$5.0 cm^{-1} for the barrier height to internal rotation for the NH_3 monomer. A non-linear *equilibrium* hydrogen bond is most consistent with the vibrationally averaged rotational constants; with the angle $\cos^{-1}[\langle\lambda_z\rangle]$ determined from $\langle\lambda_z\rangle$, the projection of the ammonia's angular momentum onto the framework. The water tunneling splitting and observed selection rules place constraints on the barrier height for proton exchange of the water as well as the most feasible water tunneling path along the intermolecular potential energy surface. An estimated barrier of 700 cm^{-1} was derived for the water tunneling motion about its c axis.

Finally, microwave spectra of $CH_3OH\cdots H_2O$ and $CH_3OD\cdots D_2O$ were recorded between 20 and 60 GHz, along with data from our collaborators at the National Institute for Science and Technology for $CH_3OH\cdots H_2O$, $^{13}CH_3OH\cdots H_2O$, $CH_3OH\cdots DOH$, $CD_3OH\cdots H_2O$, and $CH_3OD\cdots D_2O$ between 7 and 24 GHz. Because CH_3OH and H_2O are both capable of accepting and donating hydrogen bonds, there existed some question as to which donor-acceptor pairing of the molecules was the lowest energy form. This question is further emphasized by the ambiguity and variety present in

previous experimental and computational results. Transitions from the methyl torsional A state were assigned for the various isotopomers. The fit of the structure to the rotational constants gave unambiguous confirmation that the only conformation observed in the supersonically cooled molecular beams corresponded to a water-donor, methanol-acceptor complex.

Contents

List of Figures

List of Tables

Abbreviations

A—H···B	hydrogen bond: A—H = donor and B = acceptor
BSSE	basis set superposition error
cw	continuous wave—to refer to any quantity that flows or emits continuously, as opposed to pulsed, such as fluids and light
DMC	Diffusion Monte Carlo
FIR	far-infrared
FM	frequency modulation
FT	Fourier transform
GPB	gas phase basicity
HX	hydrogen halide
IPS	intermolecular potential energy surface
IR	infrared
MBER	molecular beam electric resonance
MMC	molecular mechanics for clusters
MW	microwave
M···W	$CH_3OH\cdots OH_2$, methanol-water dimer: methanol donor, water acceptor
NIST	National Institute of Standards and Technology
Rg	rare gas
PA	proton affinity
PI	permutation inversion
slm	standard liters per minute
SS	Dr. Sakae Suzuki's Ph.D. thesis, Caltech, 1996
vdW	van der Waals
VRT	vibration-rotation-tunneling
W···M	$CH_3O(H)\cdots H_2O$, methanol-water dimer: water donor, methanol acceptor

Chapter 1 Introduction

1.1 Introductory remarks

The ability of water to form hydrogen bonds to itself and other molecules is a long recognized phenomenon [1], and characterization of these hydrogen bonds is a necessary component in current studies of solvation, reaction dynamics, and functional and structural biology. These characterizations can be neatly contained in an intermolecular potential energy surface (IPS), a mathematical description of the non-covalent attractive and repulsive forces exerted by molecules upon one another, which can be obtained by inverting experimental data to conform to predetermined mathematical functions. In turn, the IPS can predict all observable quantities of the dimer, and the quality of the predictions is dependent upon the quality and breadth of the original data and functional form.

Towards this end, this thesis describes a series of experiments to obtain the microwave and far-infrared (FIR) spectra of water-containing, hydrogen-bonded dimers which probe their intermolecular vibrations, rotations, and tunneling dynamics. While it is not within the purpose or scope of this thesis to provide a complete review of intermolecular forces, placing my work within the context of past achievements and current efforts may be helpful to the reader and is instructive to the author, and so the remainder of this chapter will give an overview of a few, pertinent topics. Specifically, I will present definitions of hydrogen bonds (and weaker bonds) in terms of electrostatics and experimental observables; compare hydrogen bonds with covalent ones; review a few historical treatments of hydrogen bonding, highlighting significant changes in thought while emphasizing current levels of understanding and accomplishment; and use the the study of the $Ar\cdots H_2O$ dimer as a map of progress for spectroscopic and computational efforts. At the end of the chapter, I will give an overview of the results contained in this thesis and discuss the individual experiments

in terms of complexity and the degree of information obtained, with a particular focus on the role of tunneling interchange between equivalent frameworks.

1.2 Definition of a hydrogen bond

Apart from covalent bonds, whose strength is derived primarily from quantum mechanical exchange, or the donation of electron valency, and from ionic bonds, there exists a third set of bonds whose strength is derived from neutral electrostatic interactions and weaker quantum mechanical interactions which do not involve the exchange or donation of electron valency. For the purpose of this thesis, I will group all bonding interactions of the third category under the label of van der Waals (vdW) interactions; hydrogen bonds will be later defined as a subset of these (containing hydrogen, of course, but also including more restrictive criteria). But first, it will be useful to characterize the electrostatic and quantum mechanical forces involved in vdW bonding. Concentrating on just the long range attractive electrostatic contributions, classical distributions of static charge have two levels of interaction, those of permanent and induced multipoles. Permanent multipole moments can react both attractively and repulsively with each other, and because the inherent charge separation in multipoles gives rise to local electric fields there is also induction of multipoles in nearby molecules. In addition to static charge interactions, the quantum mechanical motions of protons and electrons produce instantaneous multipoles which interact with other permanent, induced, and instantaneous multipoles. These are termed dispersion forces. Finally, there exists a second, non-covalent quantum mechanical interaction which favors the correlation of electron spins of neighboring molecules. Summing all of these, we have

$$\begin{aligned} E_{\text{vdW}}^{\text{attractive}} &= E_{\text{permanent}}(r^{-2}, r^{-3}, \ldots) + E_{\text{induced}}(r^{-4}, r^{-6}, \ldots) + \\ & \quad E_{\text{dispersion}}(r^{-6}, r^{-8}, \ldots) + E_{\text{spin correlation}} \end{aligned} \tag{1.1}$$

More rigorous and detailed discussions of these electrostatic and weak quantum mechanical forces can be found elsewhere [2], and a particularly useful derivation of the individual terms for different dimer geometries is given by Hobza and Zahradník [5]. Equation (1.1) also ranks the four terms in their usual order of strength for most hydrogen-bonded complexes; however, for weaker vdW bonds, the quantum mechanical terms to the right may dominate the total energy expression. The total IPS is the attractive forces represented by Equation (1.1) plus short range repulsive forces.

Just as it is difficult to define small hills in the midst of tall mountains, providing a rigorous and lasting definition for hydrogen bonds in the context of larger, stronger covalently-bonded systems has eluded researchers. It is generally accepted that hydrogen bonds take the form A—H···B, where A is not a hydrogen atom and A and B are usually more electronegative than hydrogen. Beyond this basic agreement, however, researchers in different fields have applied additional criteria which reflect a bias to restrict the definition of hydrogen bond to interactions of their own interests. For example, a biochemist may wish to restrict hydrogen bonds to a short list of functional groups for A—H and B, a protein structuralist may be more concerned about the angle and separation of A—H and B as opposed to their identity, and a solvation modeler may only be concerned with the strength of interaction between A—H and B. While absolute rules have been given, dictating which functional groups may participate in hydrogen bonds as acceptors or donors and what geometries they may assume and how strong the interactions must be, a broader, more amendable definition best suits the work discussed in this thesis. Indeed, the set of hydrogen bond acceptors covered will span a large range of functionality, electronegativity, dimer geometry and binding strength. In this vein, a very useful definition was put forward by Pimentel and McClellan in their landmark monograph on the subject, which is equally appropriate here [4]. They define the term as follows.

A hydrogen bond is said to exist when:

1. *there is evidence of a bond, and*

2. *there is evidence that this bond specifically involves a hydrogen atom already*

bonded to another atom.

Beyond further semantics in defining *bond*, this definition will cover all of the species discussed here.

Pimentel and McClellan also listed certain operational criteria, or measurable effects, of hydrogen bonding that were observable with the techniques employed in the late 1950's. For the high-resolution vibration-rotation-tunneling (VRT) spectra presented in this work, there are also operational criteria that will be useful in identifying and characterizing hydrogen bonds. Specifically,

1. Rotational constants of isotopically substituted species reveal the geometry of the complex averaged over the intermolecular degrees of freedom;

2. Deuterium bonds are stronger as seen by the preference to form HO—D$\cdots$B complexes;

3. Permutation-inversion (PI) theory predicts qualitatively tunneling splittings and selection rules observed in spectra; and

4. Intermolecular VRT modes are intimately, and sometimes inseparably, coupled.

These four criteria will been seen repeatedly in the complexes examined herein.

Finally, a word about the notation of bonding interactions used in this thesis. In symbolic formulas, a centered ellipsis ($\cdots$) denotes a vdW bond and a long dash (—) denotes a covalent bond, as already used in the general notation A—H$\cdots$B. When two equivalent nuclei in a complex can rapidly interconvert, the degeneracy in donor and/or acceptor sites will be acknowledged: for example, $N_2\cdots H_2O$, as opposed to $^{14}N^{15}N\cdots$DOH. In a written formula, a short dash (-) will denote a vdW bond between two molecules: nitrogen-water.

1.3 Examples of hydrogen bonds

Because the dissociation energy of most vdW bonds is easily accessed by an ensemble of molecules at ambient temperatures, these bonds are reponsible for much of the

chemistry we experience everyday. Along with covalent and ionic bonds, vdW bonds *are* chemistry. They occur in all different forms of matter and obey the same macroscopic laws of thermodynamics as do stronger bonds. As with many experiments in chemical physics, gas phase analogs, such as water-containing, hydrogen-bonded dimers, provide a first approximation to the complex and less accessible chemistry of the condensed phases. The examples of hydrogen bonding interactions of water shown here are meant to highlight the diversity and importance of hydrogen bonds and also to motivate the interactions and dynamics which can be observed in the dimer pairs.

The condensed phases of water itself provide excellent examples of extended hydrogen-bonding systems. Figure 1.1a illustrates the near tetrahedral coordination of hydrogen bonds in the ice lattice. Each water molecule is both the donor and the acceptor of two hydrogen bonds. At normal climatic pressures and temperatures, the ice lattice has an extended hexagonal symmetry designated as I_h. Because the equilibrium bond angle of water, 104.5°, differs slightly from true tetrahedral symmetry, 109.5°, the packing of water molecules within the lattice introduces a small amount of strain. In addition to the I_h ice formed at ambient conditions, the accomodation of this strain results in a large number of lattice symmetries for ice formed under different temperatures and pressures [5].

Though liquid water at room temperature has only a slightly smaller coordination of 3.3 [6], transport through water is important for innumerable biological and electrochemical processes. Relatively low viscosity is possible because of the transient nature of hydrogen bonds at room temperature. Ice itself is an important reaction medium for the stratospheric processing of chlorine- and nitrogen-containing species in the polar regions [7, 8, 9]. Ice and water are therefore good homomolecular mediums to begin modeling the extended effects of hydrogen bonding. High-resolultion spectroscopic studies have begun to probe the energetics and dynamics of water dimer [24, 11, 12, 3, 5] and water trimer [4, 6, 7], as well as higher accuracy computations on somewhat larger clusters [18, 19, 20, 21].

Water's role as solvent in biological and geological processes, as well as in the labo-

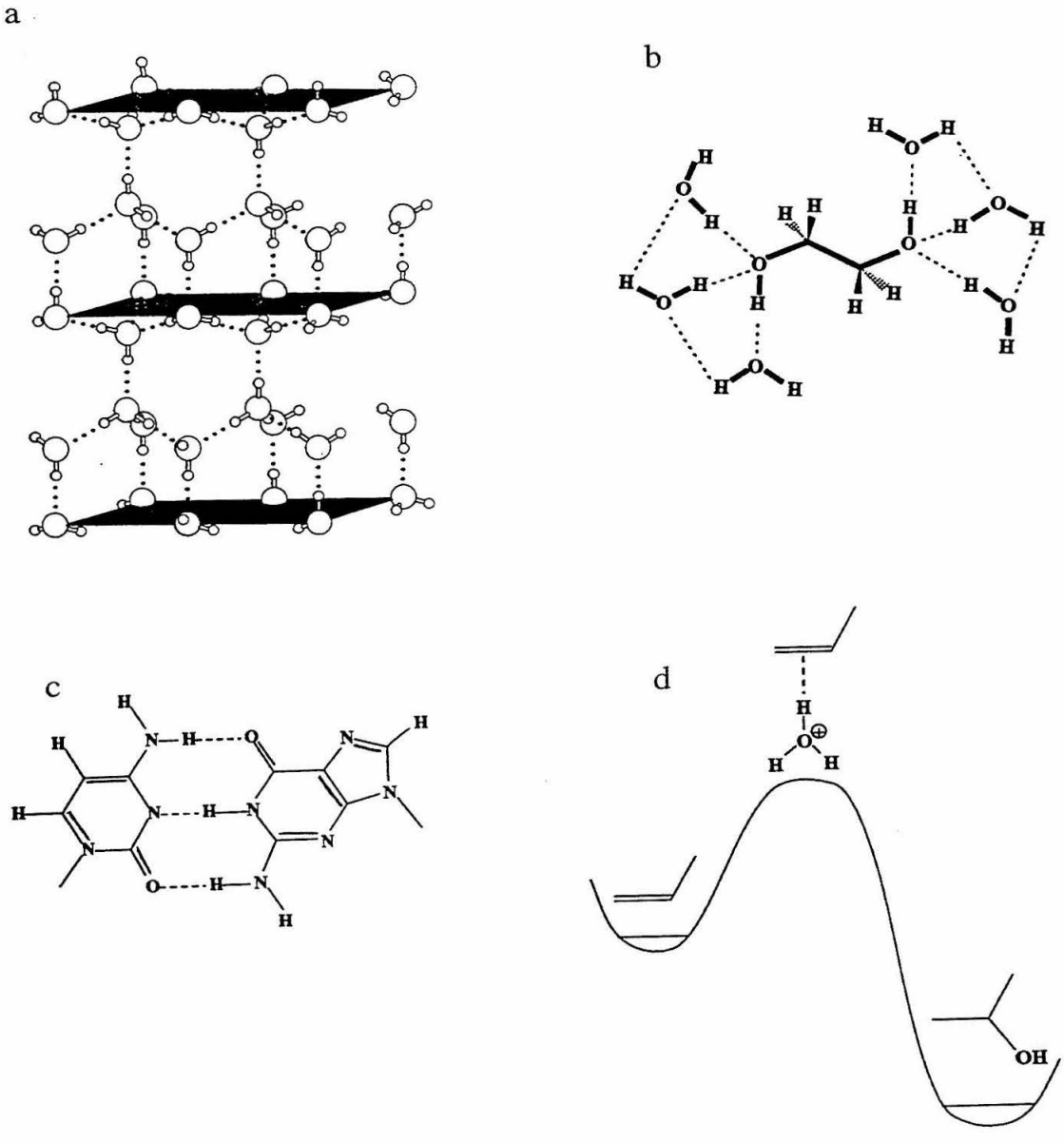

Figure 1.1: Four examples of hydrogen bonding in the condensed phase: a) crystalline ice lattice, b) aqueous solvation of ethylene glycol, c) cytosine-guanine base pair, and d) reaction surface of propene + $H_2O \rightleftharpoons$ 1-propanol.

Table 1.1: Solubilities of n-alcohols in water.

Alcohol	n	Solubility in water, wt %
methanol	1	miscible
ethanol	2	miscible
n-propanol	3	miscible
n-butanol	4	7.7
n-hexanol	6	0.58
n-octanol	8	0.05

ratory and industry, underlies the importance of hydrogen bonding in solvation. One concrete example for chemists of hydrogen bonding is the miscibility or immiscibility of different pairs of solvents. This is dramatically illustrated by the solubility of the n-alcohols listed in Table 1.1. Methanol, ethanol, and n-propanol are all completely miscible in water, while the solubility drops by an order of magnitude for each two methylene groups added thereafter: the ability of water to form a complete solvent shell around the hydrocarbon portion of the alcohol molecule determines its aqueous solubility. Recent computational studies by Dykstra indicate that nearly all of the many-body effects of solvation can be accounted for by the first solvation shell [22]. Experimentally, work has begun with a more tractable solvent, argon, in elucidating three-body and higher order effects on the IPS in the gas phase for the systems $Ar_2 \cdots HCl$ [3] and $Ar_{2-4} \cdots HF$ [24, 25].

The structure and function of many biological molecules depend upon multiple hydrogen-bonding interactions—the structure of DNA, as well as its ability to replicate; protein folding and host-guest recognition; the senses of taste and smell [26]; the function of anethesia. Shown in Figure 1.1c are the three hydrogen bonds formed from the coupling of the cytosine and guanine base pairs of DNA. While individually these bonds contribute only 3–4 kcal/mol apiece, summed over an entire chromosome they can represent 10–20 pJ for a single macromolecular dimer. Importantly though, because the binding energy comes in such small and discrete units, the entire chromosome can be unzipped in a matter of seconds during meitotic replication. Hydrogen bonds also provide non-covalent pathways for electron transfer in proteins, circum-

venting the inherent linear covalent structure in important redox centers [27]. Unique hydrogen bond geometries allow for the specificity of host-guest hydrolytic activity in proteins such as trypsin and chymotrypsin, which act on different sets of amino acids. Studies in our lab of benzene-ammonia and benzene-water complexes quantify these important aromatic-amine and aromatic-hydroxyl interaction on a molecular level [2, 11], and along with the study of many other complexes, such as ammonia-water and methanol-water discussed in this thesis [9, 31], seek to provide a comprehensive set of IPSs for incorporation into protein modeling routines. Recently, high resolution infrared (IR) spectra have been obtained for uracil in the gas phase in the anticipation of measuring intermolecular vibrations of uracil dimers, which will aid in understanding the important morphological features of DNA [32].

Hydrogen bonds also contribute directly to reaction dynamics. Figure 1.1d illustrates the reaction potential for the hydration of propene. Key to the reaction is the formation of a hydrogen bonded cluster between the reactants at the saddle point of the potential. These complexes contribute thermodynamically to carry the reactants to products. First, the geometry of the hydrogen bond aligns the two reactants in a favorable geometry. The energy of hydrogen bond then adds to the total available energy to overcome the barrier. In the gas phase, hydrogen-bonded complexes such as $HBr\cdots I_2$ [33] and $CO_2\cdots HBr$ [34] have been used as oriented precursors for time-resolved reaction dynamics studies. By photodissociating the H—Br bond in these complexes, reactive Br and H are generated.

1.4 Hydrogen bonds *vs.* covalent bonds

It is useful to compare hydrogen bonds to covalent bonds, both because hydrogen bonds are often found embedded in the context of stronger covalent bonds, and because the quantitative study of covalent bonds has preceded that of hydrogen bonds, meaning that much of the framework used to analyze hydrogen bonds is a modification of that developed for covalent ones. Figure 1.2 depicts the one-dimensional stretching potential for the covalent H—F bond and for the hydrogen bonded HF

dimer. Both of these are strong examples of the two different kinds of bonding discussed here. The most noticeable disparity between the two potential wells is the bond strengths: 136 kcal/mol for H—F and only 3 kcal/mol for the HF···HF bond. At room temperature, the hydrogen bonds are rapidly broken and reformed, while HF itself remains stable. The position of the equilibrium bond length $\langle R_e \rangle$ also varies greatly between the two examples. HF is covalently bound, which means that H and F share electrons between them. In order for this to occur, the two nuclei must be close enough to allow for non-zero orbital overlap, 0.97 Å for HF in its ground vibrational state. In hydrogen bonds, individual monomer units retain their valent electrons, and electronic repulsions balance with the long range attractive forces of Equation (1.1), resulting in bond lengths of 2–4 Å, specifically 2.79 Å for HF···HF. The third difference in the potential wells is in the potential form. Like most covalent bonds, the HF monomer bond is well-characterized by a harmonic oscillator potential in the lower half of the potential well, which means that its vibrational levels are nearly evenly spaced and selection rules make overtones very weak. However, hydrogen bonds show large anharmonicities throughout their shallow wells: vibrational levels are irregularly spaced, and the molecule can experience large deviations from $\langle R_e \rangle$ even in the ground vibrational state.

All three of the above factors sum to make the vibrational spectroscopy of hydrogen bonds much different from that of covalent bonds. Covalent bonds typically stretch and bend at frequencies between 400 and 4000 cm^{-1} in the heart of the infrared (IR). Direct absorption spectroscopy, and more recently Fourier transform spectroscopy, with black body sources has been successful in measuring IR active vibrational spectra. However, due to the shallow and broad potentials of hydrogen bonds, intermolecular modes usually occur between 10 and 400 cm^{-1}, in a range where black bodies, whose spectral intensity is proportional to the cubic power of the frequency, are inefficient sources. Moreover, the anharmonic IPSs allow strong coupling with other intermolecular vibrational modes and even high frequency rotational motion. These challenges will be addressed in the following chapters.

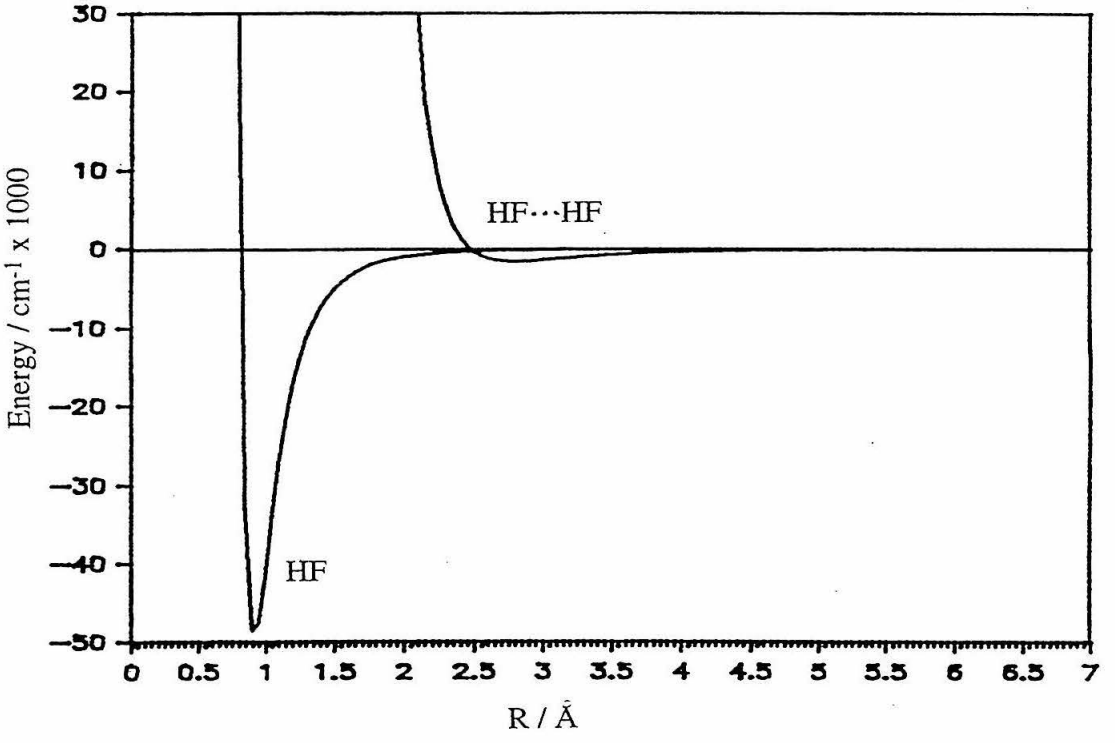

Figure 1.2: Comparison of radial potential energy surfaces for covalent H—F and hydrogen bonded HF···HF. Note the difference in binding energies, equilibrium bond lengths, and the anharmonic nature of the HF···HF potential.

1.5 Treatments of hydrogen bonds

In this section, a few levels of approach to quantifying hydrogen bonds, making better and better approximations to the true IPS, will be discussed. The purpose here is not to present a comprehensive review, but rather to give some sense of the refinement process necessary to obtain a quantitative IPS. Some such reviews will be cited.

One of the earliest formulations of non-covalent, non-ioninc bonding interactions, and certainly one of the most well-known, was by Johannes van der Waals [35]. His equation of state,

$$(P + \frac{a}{V_m^2})(V_m - b) = RT \ , \tag{1.2}$$

accounted for observed deviations from the ideal gas law derived from thermodynamic principles. Here, the quantity a represents the long range attractive force of the IPS and b represents an excluded volume or repulsive force. While a and b are molecule specific, they are completely isotropic in nature. Figure 1.3a shows the water-carbon monoxide dimer with hard sphere radii drawn around the monomer units calculated from virial coefficients.

Another name strongly associated with hydrogen bonds is Linus Pauling. By recording the distances between different atoms and functional groups in crystalline solids via x-ray crystallography, he determined specific van der Waal radii, or contact distances, for atoms and functional groups [36]. While locally isotropic, these atomic radii can be joined to form a global, anisotropic vdW surface about a molecule. Such surfaces are shown in Figure 1.3b for water- carbon monoxide dimer. The orientation chosen in the figure is somewhat arbitrary, attempting a closest approach geometry. Although the directionality of vdW forces was certainly recognized by Pauling in 1930 [37], there was not the level of detail available to predict the averaged geometry of a cluster such as $OC\cdots H_2O$.

A decade later, the development of the Hellman-Feynman theorem gave proof that the IPS and observables were directly related and interconvertable [38]. Specifically, it relates the distribution of electronic charges and the quantum mechanical forces which govern electrons and nucleons. In turn, the electronic distribution is directly related

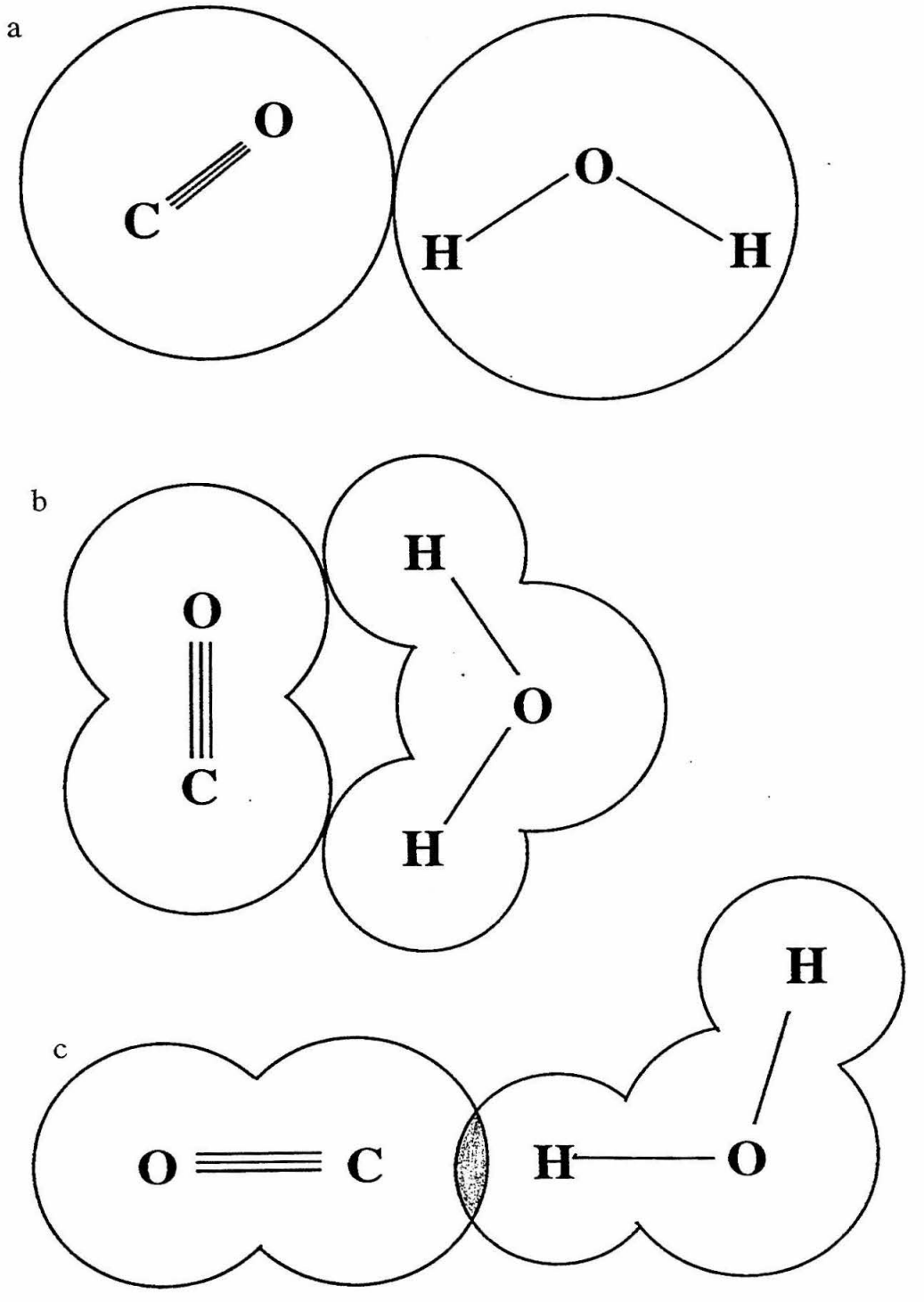

Figure 1.3: Three different binding descriptions fo the carbon monoxide-water dimer: a) with molecular virial coeffiecients, b) with vdW radii, and c) with vdW radii overlap and true equilibrium geometry.

to the IPS. Thus, the link between observables and the IPS is firmly established and it is bidirectional. By measuring a set of observables which completely probes all portions of the IPS, an accurate IPS for the system can, in principle, be obtained.

As stated earlier, the work represented by thesis is part of a much larger effort to measure high-resolution spectra of vdW clusters in order to invert them to IPSs. Work from the first half of this century measured many bulk properties hydrogen-bonding substances—*e.g.*, virial coefficients, dielectric constants, dipole moment enhancements, melting and boiling point anomalies, mixing heats, blue and red shifting of IR spectra—which provided some information about the attractive and repulsive portions of IPSs, but which was obscured by the many-bodied effects of the bulk. Very comprehensive reviews of this work have been authored by Hirschfelder, Curtiss, and Bird [39] and Pimentel and McClellan [4]. Much of the limitations of this era stemmed from the inability to cool and isolate weak hydrogen bonds. Hence, much of the bound region of the IPS remained unexplored. With the advent of molecular beams, rotationally and vibrationally cooled molecular clusters could be formed and probed. Since the potential well of strongly-bound dimers can be as deep as 8 kcal/mol for carboxylic acid dimers, different spectral probes are needed in order to cover the entire IPS. High resolution radiowave, microwave, FIR, and IR spectroscopies span this region, and all of these have been employed, as well as higher energy IR and electronic techniques. Reviews by Ewing [40, 41], Dyke [42], and Saykally and Blake [43] chronicle the state-of-the-art accomplishments at various intervals. In addition, a bibliography maintained by Novick catalogs all high resolution spectra of vdW clusters [44].

1.6 Ar···H_2O: the simplest water-containing, hydrogen-bonded dimer

Prior to the beginning of the experiments discussed in this work, efforts to measure the VRT spectra of Ar···H_2O and incorporate the results into a multidimensional IPS

were underway. Ar$\cdots$$H_2O$ is the simplest example of water donating a hydrogen bond to another species, and so is a logical place to begin a discussion of water-containing, hydrogen bonded dimers. From this example, much of the complexity associated with larger dimer pairs can be anticipated, and because the donor is an atom rather than a molecule, the dynamical information obtained is simplified to reflect the behavior of the water molecule in the presence of a point source perturbation.

The degree of information contained in an IPS, and hence also the degree of difficulty in obtaining it, scales with the number of intermolecular modes of the complex. For a dimer formed by two molecules M and N, the number of intermolecular modes, v_{im}, is calculated as follows:

$$v_{im} = 3(m+n) - 3^{translation} - 3^{rotation} - v_m - v_n \ , \tag{1.3}$$

where m and n are the number of atoms in M and N, and v_m and v_n are the corresponding number of intramolecular vibrational modes. Figure 1.4 summarizes the six scenarios possible for dimers formed from rare gas (Rg) atoms, diatomics (AB), and polyatomics (here represented by water). As shown, water complexes with Rg have three intermolecular modes, with diatomics five, and with polyatomics six. Ar$\cdots$$H_2O$, with only three intermolecular modes, is therefore a much less complicated example of water hydrogen bonding than all other non-Rg containing dimers. When Rg$\cdots$AB and AB$\cdots$AB complexes are aligned linearly, they have only two degrees of rotational freedom, and hence an extra intermolecular vibrational mode.

Another consideration in the example of Ar$\cdots$$H_2O$ is the partitioning of the rotational wavefunction into ortho and para nuclear spin states. Just like a freely rotating hydrogen molecule, the chemically identical hydrogen atoms of H_2O and D_2O, when free to interchange, must pair rotational and nuclear spin wavefunctions in order to satisfy the Pauli exclusion principle. For the case of protium, which is a fermion, the symmetry of the product $\psi_{exchange}$ of the rotational and nuclear spin wavefunctions, ψ_{rot} and ψ_{ns}, must be antisymmetric (–) with respect to exchange; for deuterium, a boson, it must be symmetric (+). In non-linear molecules, the total rotational wave-

M	N	m	n	ν_m	ν_n	ν_{im}
Ar	Ar	1	1	0	0	1
Ar	AB	1	2	0	1	2
Ar	H_2O	1	3	0	3	3
AB	AB	2	2	1	1	4
AB	H_2O	2	3	1	3	5
H_2O	H_2O	3	3	3	3	6

Figure 1.4: Intermolecular degrees of freedom for all possible pairings of rare gas, diatomic, and polyatomic molecules. Numbers refer to variables of Equation (1.3).

function must be further divided into the product of the overall rotational angular momentum wavefunction, ψ_J, and the wavefunction which represents the component of angular momentum parallel to the limiting symmetry axis, ψ_K. Because water is not a symmetric top, K is not a good quantum number, and the rotational eigenstates are labelled according to their connections to *both* the prolate and oblate limiting cases. The symmetry of ψ_K for these eigenstates is determined by the values of K_P and K_O and the axis about which the molecule is rotating. Exchanging hydrogens in water is a b-type rotation, and symmetry considerations dictate that $\psi_{K_PK_O}$ is symmetric when $K_P + K_O$ is even and antisymmetric for the odd sum. The whole product is then

$$\psi_{exchange} = \psi_J \otimes \psi_{K_PK_O} \otimes \psi_{ns}. \tag{1.4}$$

(A more detailed explanation of the symmetry with respect to exchange for asymmetric top molecules is given in reference [45]). As a consequence, half of the rotational eigenstates of water are paired with ortho water and half with para water, according to the rules laid out above. Since ortho and para states do not rapidly interconvert in the gas phase, this pairing leads to metastable energy states when the molecules are rotationally cooled, as in a molecular beam. Finally, the spin statistics for forming ortho and para wavefunctions give statistical weights for ortho and para states—1:3 for H_2O and 2:1 for D_2O.

When two molecules combine to form a dimer, their individual translational and rotational degrees of freedom give rise to the translational and rotational degrees of freedom of the complex as well as the newly formed intermolecular modes. This was illustrated in Figure 1.4. Depending upon how strongly the two molecules interact, these new modes can best be described either as slightly hindered rotations of the substituent monomers, in the weakly-bound limit, or as intermolecular vibrations, for strongly bound dimers. Due to its weak level of electrostatic interaction, $Ar\cdots H_2O$ lies in the former limit. Figure 1.5 shows the effect of the perturbation of the energy levels of freely rotating water by the hydrogen bond acceptor Ar. Notice that the effect is to break the M = 2J + 1 spatial degeneracy in the water monomer into separate

energy levels. Also shown is the pairing of the ortho and para wavefunctions with the different rotational eigenstates to form two separate manifolds, with the lowest energy ortho state $\Sigma(1_{01})$ lying approximately 20 cm^{-1} above the $\Sigma(0_{00})$ para ground state. The two unique rotations, θ and ϕ, of the water molecule with respect to the Ar-water center-of-mass axis are shown in Figure 1.6. The intermolecular stretch ν_s constitutes the third degree of intermolecular freedom (R_{cm}), and provides a vibrational manifold upon which the rotational manifolds build.

Quite an abundant amount of high resolution VRT spectra have been recorded for the argon-water complex. Primary among these are the nine FIR bands measured by Cohen and coworkers, which sample all three intermolecular modes for $Ar\cdots H_2O$ [46, 47, 48]. The microwave spectra of the rovibrational ground states, ortho and para, of the natural isotopomer were measured by Fraser *et al.* [49], while experiments in our lab [50] and in Nijmegen [51] recorded 2 bands each for the $Ar\cdots D_2O$ species in the para and ortho manifolds, respectively. In addition, important energy spacings were measured by Lascola and Nesbitt for the $\Sigma(1_{01}) - \Pi(1_{01})$ degeneracy splitting in the $Ar\cdots H_2O$ complex by combination bands of the O—H asymmetric stretch [52], and ortho and para manifolds were linked together with the $Ar\cdots DOH$ band $\Sigma(0_{00}) \leftarrow \Sigma(1_{01})$ measured by Suzuki *et al.*, which is allowed because there are no ortho/para spin pairings for HOD [50]. Taken together, these data represent the most comprehensive set of measurements for an IPS calculation, sampling 55% of the entire IPS phase space [48, 53].

Using the above data set, Cohen and Saykally derived two IPSs for $Ar\cdots H_2O$: AW1 with a partial data set [54], and AW2 with the complete set [1]. Two-dimensional slices through the three-dimensional AW2 surface are shown in Figure 1.7a and b. Cohen and Saykally chose to use a collocation method, developed by Yang and Peet [56], which simplifies the treatment of the coupling of intermolecular degrees of freedom by fitting the surface to a grid of points whose number, n, and location corresond to a discretely parameterized basis set. It should be noted that in the study of $Ar\cdots H_2O$, the construction of the IPS was driven almost entirely by experimental results, and not by *ab initio* or semi-empirical computations. This is significantly

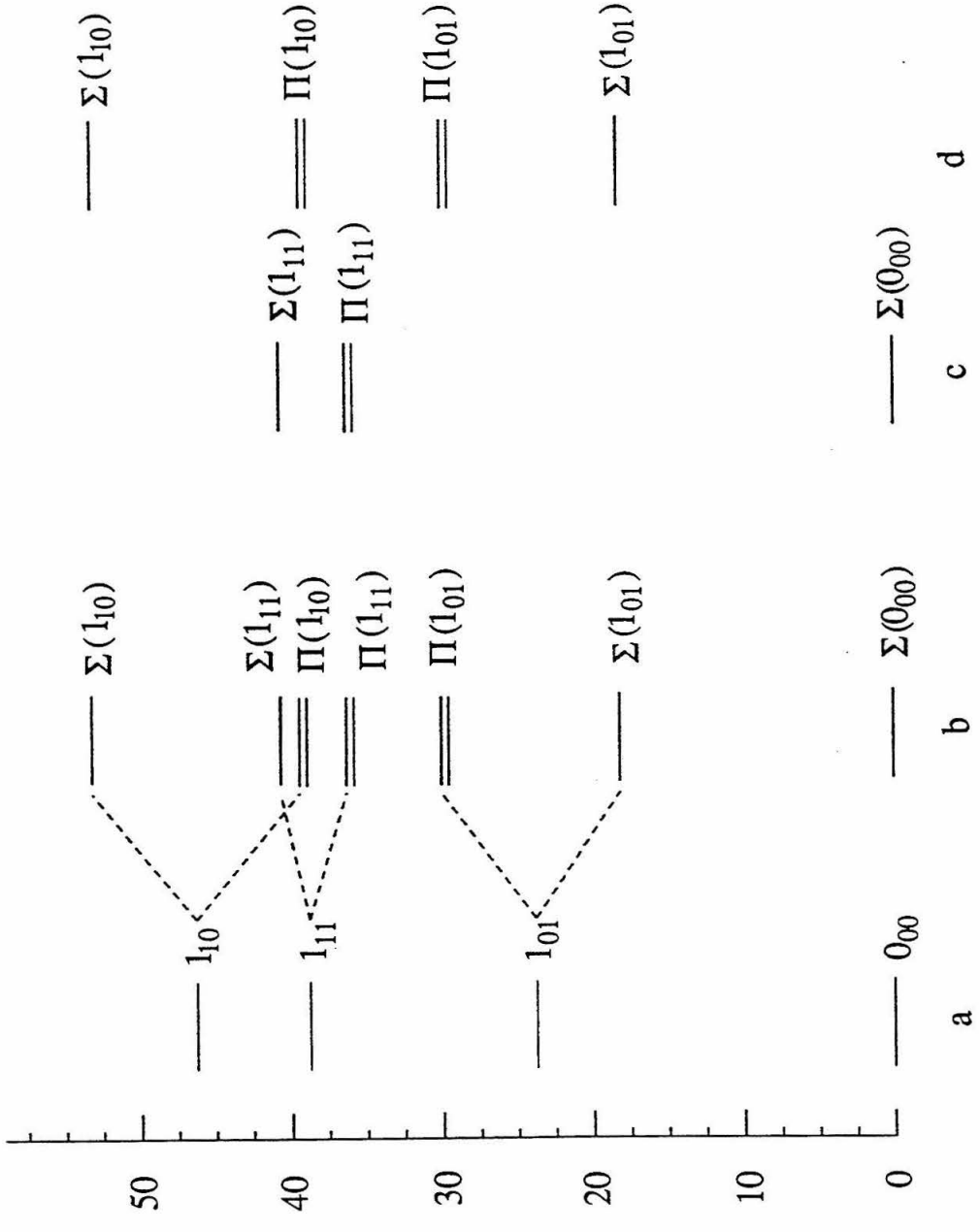

Figure 1.5: Rotational manifold for Ar···H_2O showing slight hindering perturbation of Ar upon the H_2Ofree-rotor energy levels: a) water free-rotor energy levels, b) effect of slight hindering perturbation, and pairing of Ar···H_2O rotational eigenstates with c) para and d) ortho water nuclear spin functions.

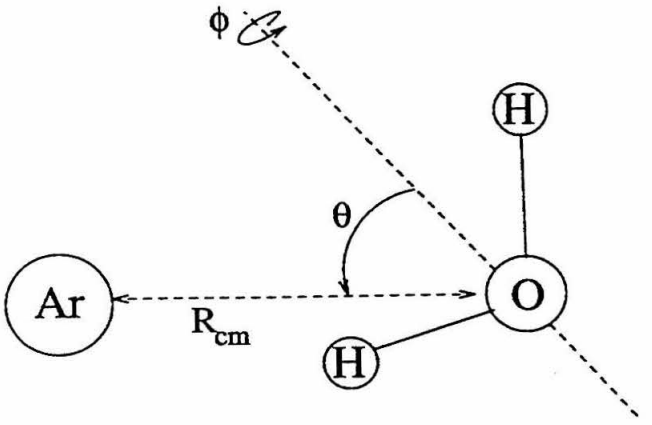

Figure 1.6: Intermolecular coordinates for Ar···H_2O.

different from earlier efforts to obtain the spectra and IPS for the two-dimensional Ar···HCl hydrogen-bonded dimer [57, 58, 59]. Here, theory played a large role in both the prediction of FIR spectra and the construction of the correct IPS form [60, 61, 62]. Because the intermolecular modes of vdW complexes are inherently coupled with each other, it is difficult to predict *a priori* the nature of an efficient and effective Hamiltonian to describe them. It may well be the trend, at least in the near future, that experiment will lead theory in the development of IPSs for clusters with many degrees of freedom.

Results from the AW2 surface elucidate the nature of the hydrogen-bonding interaction between argon and water. Although there exists a global minimum on the surface at approximately $\theta = 90°, \phi = 0°$, the lowest eigenstate $\Sigma(0_{00})$ floats on 45 cm^{-1} of zero point energy above the surfaces shown in Figure 1.7a and b. With this amount of energy, the Ar···H_2O cluster can access all possible (θ,ϕ) geometries: the model of water as a slightly hindered rotor in the presence of argon is correct. Thus, the notion of defining an equilibrium geometry for this cluster is moot, and the importance of relying on an IPS to describe the cluster becomes apparent. Also

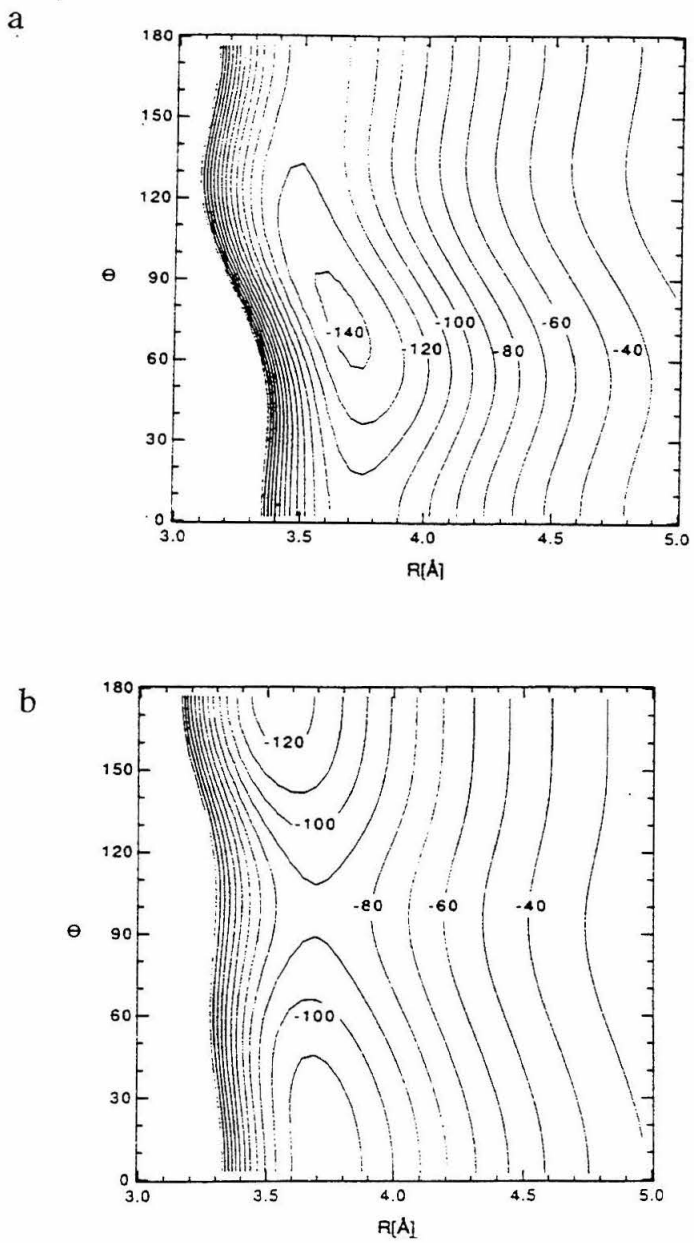

Figure 1.7: IPS contours for Ar$\cdots$H$_2$O from AW2 of Cohen and Saykally: a) θ *vs.* R, $\phi = 0°$; b) θ *vs.* R, $\phi = 90°$.

following from the surface potential cuts is the high degree of angular-radial coupling present. R_{min} varies by 0.3 Å over a range of 50° of θ from 3.5 Å at $\theta = 110°$ to 3.8 Å at $\theta = 60°$. This is also true to a smaller extent in the ϕ coordinate. If one relies on Equation (1.1) to represent the features of the AW2 surface, a large number of terms is needed in order to recreate the complexity exhibited. Indeed, Cohen and Saykally found that both the repulsive and attractive forces were strong and anisotropic [1].

The lesson from AW2 is that much work needs to be done in order to charcterize the IPSs of vdW clusters, and that in turn, these IPSs are necessary for a correct and complete understanding of intermolecular dynamics. Also learned was the need for true multi-dimensional calculations to arrive at a truthful IPS; attempts to the contrary yielded an IPS which did not reproduce all of the experimental data [52].

What are the implications for further work with water-containing, hydrogen-bonded dimers? Of course, this question is asked with the hindsight of the work that follows, but it is useful to consider the expectations stemming from this initial and thorough study. Listed below are six corollaries from $Ar\cdots H_2O$ that will frame the study of vdW clusters of water with larger molecules.

1. The hydrogen bonds donated by water to neutral, non-Rg molecules are undoubtedly stronger than the 0.41 kcal/mol of the the $Ar\cdots H_2O$ dimer. Having no large electrostatic moments, Rg atoms are the weakest hydrogen bond acceptors. A good comparison is the strong hydrogen bond formed between two water molecules, which has been measured as 5.4 kcal/mol [63].

2. Due to the increased electrostatic and molecular structure of the acceptor, these complexes have a more localized structure than $Ar\cdots H_2O$. Molecular dipole and quadrupole moments of these acceptors tend to align themselves with the similar moments of water, and heteronuclear acceptor partners have a distinct chemical preference for which moiety is the best hydrogen bond acceptor.

3. This increased anisotropy affects the framework upon which the IPS is built. Because the internal rotations of the monomers within the complex are more restricted, intermolecular degrees of freedom are better modeled as vibrations

rather than hindered rotations.

4. When the exchange of indentical nuclei by internal rotation is restricted by stronger IPSs, quantum mechanical tunneling becomes operative. This is a wholy separate phenomenon from rotations and vibrations, and does not have a classical mechanical analog. Just as with rotations, when identical nuclei are exchanged by tunneling, the symmetry of the tunneling wavefunction must pair correctly with the nuclear spin wavefunction in order to satisfy the Pauli exclusion principle. Acceptor as well as donor molecules can undergo tunneling.

5. With a more complex acceptor molecule comes a more complex IPS. In $Ar\cdots H_2O$, the three degrees of intermolecular freedom were defined as movements of the water subunit relative to the argon atom. When water binds to polyatomic molecules, they have their own intermolecular movements relative to water. Experimentally, there are more intermolecular modes to find and measure, and the motions of one subunit are often coupled with those of the other. Correctly describing these normal modes is challenging.

6. Calculationally, the inversion of the spectral data to determine the IPS scales as v_{im}^3 or v_{im}^4. Also, determining the appropriate reduced mass for these intermolecular motions is essential to account for the coupled intermolecular motions.

Considering these six corollaries will aid in organizing the subsequent work discussed in this thesis.

1.7 Overview of thesis work and results

The work presented in this thesis builds on the initial VRT study of $Ar\cdots H_2O$, seeking to extend this type of analysis to more complex and more chemically and biologically relevant intermolecular interactions. Challenges, both experimental and theoretical, were outlined above, and are addressed throughout the work. The organization for the remainder of the thesis is as follows.

Chapter 2 describes the experimental instrumentation used to record the FIR and microwave spectra of vdW complexes, and documents typical data collection parameters and procedures. Also included are practical fabrication and repair methods peculiar to the instrumentation or the way that it was used.

Chapter 3 begins the VRT study of water-containing, hydrogen-bonded vdW clusters with FIR data on rotational-tunneling states of $N_2 \cdots H_2O$, $OC \cdots H_2O$, and some common isotopomers. The phenomenon of quantum mechanical tunneling of identical and feasibly exchangeable nuclei is first addressed here as well as its effects on the spectra, and two- and three-term Fourier expansions are fit to the tunneling data. Using the rotational data from all of the isotopomers, a complete structural analysis is given. Several *ab initio* IPSs are used to illustrate the different available tunneling pathways and also to motivate the discussion of normal mode analysis for weakly-bound vdW complexes with wide-amplitude motions. Finally, some partial VRT spectra are presented, and their possible vibrational assignment is discussed.

In Chapter 4, ammonia is studied as a hydrogen acceptor from water. Both microwave and FIR VRT data are used to model the large-amplitude interal rotor and tunneling potentials of the complex. Of special spectroscopic concern is the coupling of the angular momenta between the internal NH_3 top and the overall complex rotation. This is shown to have a large displacement effect on the frequency of the b-type rotational spectra for the complex. Again, the rotational data are used to fit the structure of the complex.

Structure determination is the primary goal of Chapter 5, which studies the methanol-water complex. Both of these hydroxyl containing subunits have the amphoteric ability to accept and donate hydrogen bonds. The topology of the gas-phase complex is a test of common chemical assumptions about acid and base strengths, and allows assessment of the accuracy of various *ab initio* efforts. The structure of the polyfunctional dimer also provides the opportunity to assess the adaptability of the water dimer potential and VRT formalism to other complex systems.

Chapter 6 is a summary of the effort to date, including comparisons with the work recorded here and other water-containing, hydrogen-bonded dimers studied at this

level of detail and energy. Conclusions are drawn from trends in binding energy and vibrational frequencies. Finally, some future challenges and directions are outlined.

Bibliography

[1] W.L. Latimer and W.H. Rodebush. Polarity and Ionization from the Standpoint of the Lewis Theory of Valence. *J. Am. Chem. Soc.*, 42:1419, 1920.

[2] J.N. Murrell, S. Carter, S.C. Farantos, P. Huxley, and A.J.C. Varandas. *Molecular Potential Energy Functions.* John Wiley and Sons, New York, 1984.

[3] P. Hobza and R. Zahradník. *Intermolecular Complexes.* Elsevier, New York, 1988.

[4] G.C. Pimentel and A.L. McClellan. *The Hydrogen Bond.* W.H. Freeman and Co., San Francisco, 1960.

[5] N.H. Fletcher. *The Chemical Physics of Ice.* Cambridge University Press, New York, 1970.

[6] C.M. Davis and T.A. Litovitz. Two-state Theory of the Structure of Water. *J. Chem. Phys.*, 42:2563, 1965.

[7] M.J. Molina, T.-L. Tso, L.T. Molina, and F. C.-Y. Wang. Antarctic Stratospheric Chemistry of Chlorine Nitrate, Hydrogen Chloride, and Ice: Release of Active Chlorine . *Science*, 238:1253, 1987.

[8] M.A. Tolbert, M.J. Rossi, and D.M. Golden. Heterogeneous Interactions of Chlorine Nitrate, Hydrogen Chloride, and Nitric Acid with Sulfuric Acid Surfaces at Stratrospheric Temperatures. *Geophys. Res. Lett.*, 15:847, 1988.

[9] R.P. Turco, O.B. Toon, and P. Hamill. Heterogeneous Physicochemistry of the Polar Ozone Hole. *J. Geophys. Res.*, 94:16493, 1989.

[10] J.A. Odutola and T.R. Dyke. Partially Deuterated Water Dimers: Microwave Spectra and Structure. *J. Chem. Phys.*, 72:5062, 1980.

[11] R.D. Suenram, G.T. Fraser, and F.J. Lovas. Microwave Spectrum of $(D_2O)_2$. *J. Mol. Spect.*, 138:440, 1989.

[12] G.T. Fraser, R.D. Suenram, and L.H. Coudert. Microwave Electric-Resonance Optothermal Spectroscopy of $(H_2O)_2$. *J. Chem. Phys.*, 90:6077, 1989.

[13] N. Pugliano and R.J. Saykally. Measurement of the ν_8 Intermolecular Vibration of $(D_2O)_2$ by Tunable Far Infrared-Laser Spectroscopy. *J. Chem. Phys.*, 96:1832, 1992.

[14] N. Pugliano, J.D. Cruzan, J.G. Loeser, and R.J. Saykally. Vibrational and K_a' Dependencies of the Multidimensional Tunneling Dynamics in the 82.6 cm^{-1} Intermolecular Vibration of Water Dimer-d_4. *J. Chem. Phys.*, 98:6600, 1993.

[15] N. Pugliano and R.J. Saykally. Measurement of Quantum Tunneling between Chiral Isomers of the Cyclic Water Trimer. *Science*, 257:1937, 1992.

[16] K. Liu, J.G. Loeser, M.J. Elrod, B.C. Host, J.A. Rzepiela, N. Pugliano, and R.J. Saykally. Dynamics of Structural Rearrangements in the Water Trimer. *J. Am. Chem. Soc.*, 116:3507, 1994.

[17] S. Suzuki and G.A. Blake. Pseudorotation in the D_2O Trimer. *Chem. Phys. Lett.*, 229:499, 1994.

[18] K.S. Kim, M. Dupuis, G.C. Lie, and E. Clementi. Revisiting Small Clusters of Water Molecules. *Chem. Phys. Lett.*, 131:451, 1986.

[19] S. Kuwajima and A. Warshel. Incorporating Electric Polarizabilities in Water-Water Interaction Potentials. *J. Phys. Chem.*, 94:460, 1990.

[20] S. Saebø, W. Tong, and P. Pulay. Efficient Elimination of Basis Set Superposition Errors by the Local Correlation Method: Accurate *Ab Initio* Studies of the Water Dimer. *J. Chem. Phys.*, 98:2170, 1993.

[21] J.K. Gregory and D.C. Clary. Calculations of the Tunneling Splittings in Water Dimer and Trimer Using Diffusion Monte Carlo. *J. Chem. Phys.*, 102:7817, 1995.

[22] C.E. Dykstra. Model Calculations on a Collection of Weakly Bound Trimers. In *Abstracts of the 50th International Symposium on Molecular Spectroscopy*, 1995.

[23] M.J. Elrod, R.J. Saykally, A.R. Cooper, and J.M. Hutson. Nonadditive Intermolecular Forces from the Spectroscopy of van der Waals Trimers—Far-Infrared Spectra and Calculations on Ar_2–DCl. *Mol. Phys.*, 81:579, 1994.

[24] A. McIlroy, R. Lascola, C.M. Lovejoy, and D.J. Nesbitt. Structural Dependence of HF Vibrational Red Shifts in Ar_nHF, n=1–4, via High-resolution Slit Jet Infrared Spectroscopy. *J. Phys. Chem.*, 95:2636, 1991.

[25] A. McIlroy and D.J. Nesbitt. Intermolecular HF Motion in Ar_nHF Micromatrices (n=1,2,3,4)—Classical and Quantum Mechanical Calculations on a Pairwise Additive Potential Surface. *J. Chem. Phys.*, 97:6044, 1992.

[26] During the operation of the far-infrared laser as well as spectroctroscopic studies of the methanol-water dimer, I was able to clearly discern the smell of CH_3OD from CH_3OH. Just the change of the labile hydrogen from H to D makes methanol smell much sweeter.

[27] D.S. Wuttke, M.J. Bjerrum, I.J. Chang, J.R. Winkler, and H.B. Gray. Electron Tunneling in Ruthenium-modified Cytochrome-c. *Biochim. et Biophys. Acta*, 1101:168, 1992.

[28] D.A. Rodham, S. Suzuki, R.D. Suenram, F.J. Lovas, S. Dasgupta, W.A. Goddard, and G.A. Blake. Hydrogen-bonding in the Benzene Ammonia Dimer. *Nature*, 362:735, 1993.

[29] S. Suzuki, P.G. Green, R.E. Bumgarner, S. Dasgupta, W.A. Goddard, and G.A. Blake. Benzene Forms Hydrogen-bonds with Water. *Science*, 257:5072, 1992.

[30] P.A. Stockman, R.E. Bumgarner, S. Suzuki, and G.A. Blake. Microwave and Tunable Far-infrared Laser Spectroscopy of the Ammonia-Water Dimer. *J. Chem. Phys.*, 96:2496, 1992.

[31] P.A. Stockman, F.J. Lovas, R.D. Suenram, and G.A. Blake. Microwave Spectroscopy and Structure of the Methanol-Water Dimer. *J. Chem. Phys.*, 1995. in preparation.

[32] R.S. Fellers, R.P. McLaughlin, M.R. Viant, and R.J. Saykally. Infrared Spectroscopy of Jet Cooled Biological Molecules with Diode Lasers. In *Abstracts of the 50th International Symposium on Molecular Spectroscopy*, 1995.

[33] I.R. Sims, M. Gruebele, E.D. Potter, and A.H. Zewail. Femtosecond Real-time Probing of Reactions. 8. The Bimolecular Reaction Br + I_2. *J. Chem. Phys.*, 97:4127, 1992.

[34] S.K. Shin, C. Wittig, and W.A. Goddard. Photoinitiated H-atom Reactions in CO_2–HBr Complexes. *J. Phys. Chem.*, 95:8048, 1991.

[35] Johannes D. van der Waals. PhD thesis, Leiden University, 1873.

[36] L. Pauling. *The Nature of the Chemical Bond.* Cornell University Press, Ithaca, NY, 3rd edition, 1960.

[37] Indeed, Pauling and other scientists of that era clearly recognized the large electrostatic nature of hydrogen bonds and even the role of the newly discovered London dispersion forces (see *The Nature of the Chemical Bond*).

[38] R.P. Feynman. Forces in Molecules. *Phys. Rev.*, 56:340, 1939.

[39] J.O. Hirschfelder, C.F. Curtiss, and R.B. Bird. *Molecular Theory of Gases and Liquids.* John Wiley and Sons, New York, 1954.

[40] G.E. Ewing. Infrared Spectroscopy. *Ann. Rev. Phys. Chem.*, 23:141, 1972.

[41] G.E. Ewing. The Spectroscopy of van der Waals Molecules. *Can. J. Phys.*, 34:487, 1976.

[42] T.R. Dyke. Microwave and Radiofrequency Spectra of Hydrogen-bonded Complexes in the Vapor-phase. *Topics in Curr. Chem.*, 120:85, 1984.

[43] R.J. Saykally and G.A. Blake. Molecular-interactions and Hydrogen-bond Tunneling Dynamics— Some New Perspectives. *Science*, 259:1570, 1993.

[44] S.E. Novick. Bibliography of Rotational Spectra of Weakly Bound Complexes. This bibliography is updated several times a year and available from the author electronically at snovick@boltzmann.wesleyan.edu.

[45] C.H. Townes and A.L. Schawlow. *Microwave Spectroscopy.* Dover Publications, New York, 1975.

[46] R.C. Cohen, K.L. Busarow, K.B. Laughlin, G.A. Blake, M. Havenith, Y.T. Lee, and R.J. Saykally. Tunable Far Infrared-Laser Spectroscopy of van der Waals Bonds—Vibration-Rotation-Tunneling Spectra of Ar–H_2O. *J. Chem. Phys.*, 89:4494, 1988.

[47] R.C. Cohen, K.L. Bursarow, Y.T. Lee, and R.J. Saykally. Tunable Far Infrared-Laser Spectroscopy of van der Waals Bonds—the Intermolecular Stretching Vibration and Effective Radial Potentials for Ar–H_2O. *J. Chem. Phys.*, 92:169, 1990.

[48] Ronald Carl Cohen. *Determination of Multidimensional Intermolecular Potential Energy Surfaces.* PhD thesis, University of California, Berkeley, 1992.

[49] G.T. Fraser, F.J. Lovas, R.D. Suenram, and K. Matsumura. Microwave Spectrum of Ar–H_2O: Dipole Moment, Isotopic Studies, and ^{17}O Quadrupole Coupling Constants. *J. Mol. Spec.*, 144:97, 1990.

[50] S. Suzuki, R.E. Bumgarner, P.A. Stockman, P.G. Green, and G.A. Blake. Tunable Far-infrared Laser Spectroscopy of Deuterated Isotopomers of Ar–H_2O. *J. Chem. Phys.*, 94:824, 1991.

[51] E. Zwart and W.L. Meerts. The Submillimeter Rotation-Tunneling Spectrum of Ar–D_2O and Ar–NH_3. *Chem. Phys.*, 151:407, 1991.

[52] R. Lascola and D.J. Nesbitt. Slit-jet Near-infrared Spectroscopy and Internal Rotor Dynamics of the ArH_2O Complex—an Angular Potential-Energy Surface for Internal H_2O Rotation. *J. Chem. Phys.*, 95:7917, 1991.

[53] This 55% is above the zero point energy of the complex. When this uncertainty energy is taken into account, the spectral data probe up to 86% of the bound state region.

[54] R.C. Cohen and R.J. Saykally. Extending the Collocation Method to Multi-dimensional Molecular Dynamics: Direct Determination of the Intermolecular Potential of Ar–H_2O from Tunable Far-infrared Laser Spectroscopy. *J. Phys. Chem.*, 94:7991, 1990.

[55] R.C. Cohen and R.J. Saykally. Determination of an Improved Global Potential Energy Surface for Ar–H_2O from Vibration-Rotation-Tunneling Spectroscopy. *J. Chem. Phys.*, 98:6007, 1993.

[56] W.T. Yang and A.C. Peet. The Collocation Method for Bound Solutions of the Schrodinger- Equation. *Chem. Phys. Lett.*, 153:98, 1988.

[57] D. Ray, R. Robinson, D.-H. Gwo, and R.J. Saykally. Intracavity Far-Infrared Laser-Absorption Sepctroscopy of van der Waals Complexes in Supersonic Free Jets. *J. Opt. Soc. Am. B*, 3:100, 1986.

[58] R. Robinson, D.-H. Gwo, and R.J. Saykally. An Extended Study of the Lowest Pi-Bending Vibration-Rotation Spectrum of Ar-HCl by Intracavity Far Infrared-Laser Microwave Double-Resonance. *J. Chem. Phys.*, 87:5149, 1987.

[59] R. Robinson, D.-H. Gwo, and R.J. Saykally. Far Infrared-Laser Stark Spectroscopy of the Sigma-Bending Vibration of Ar-HCl—Strong Evidence for a Double Minimum Potential Surface. *Mol. Phys.*, 63:1021, 1988.

[60] J.M. Hutson and B.J. Howard. Anisotropic Intermolecular Forces 1. Rare Gas-Hydrogen Chloride Systems. *Mol. Phys.*, 45:769, 1982.

[61] J.M. Hutson. The Intermolecular Potential of Ar-HCl—Determination from High-Resolution Spectroscopy. *J. Chem. Phys.*, 89:4550, 1988.

[62] J.M. Hutson. Vibrational Dependence of the Anisotropic Intermolecular Potential of Ar-HCl. *J. Phys. Chem.*, 96:4237, 1992.

[63] D.R. Haynes, N.J. Tro, and S.M. George. Condensation and Evaportaion of H_2O on Ice Surfaces. *J. Phys. Chem.*, 96:8502, 1992.

Chapter 2 Experimental Equipment and Methods

2.1 Introduction

The purpose of this work is to obtain and analyze high-resolution VRT spectra of water-containing, hydrogen-bonded clusters as a basis for determining their IPSs and also to learn about more qualitative aspects of hydrogen-bonding interactions. Due to the nature of vdW bonds, the most informative spectral regions for these clusters are the microwave (MW) and FIR frequencies, where information about equilibium geometry and IPS shape, as well as intracluster dynamics, can be obtained. The method employed here is direct absorption spectroscopy using both MW and FIR sources. The instruments used in Professor Blake's laboratory have been developed over several years, and the reader will be refered to the original work for many of the details. What will be explained in this chapter are the peculiarities of the instruments as they are used (and repaired) in the Blake lab and also the methods employed to collect the spectra. My work in the Blake lab has been concurrent with that of Dr. Sakae Suzuki, and we have divided important topics about the spectrometers between us to be discussed in our theses. While some material does overlap from the necessity of continuity, the two should be read together for a complete discription, and I will refer to Sakae's thesis (SS) where appropriate [12]. In the following section, an overview of the spectrometers is given, and the commonalites of the MW and FIR instruments is explained using an analogy to Beer's Law. Each spectrometer is then discussed in more detail, as well as the common components—molecular beam, frequency modulation (FM) and lock-in detection, and scanning software. Finally, a description of a Fourier transform (FT) MW spectrometer at the National Institute of Standards and Technology (NIST) in Gaithersburg, MD, from which some of the

methanol-water data used in Chapter 5 were obtained, is included.

2.2 Overview of MW and FIR spectrometers

The general method employed to measure the VRT spectra of vdW complexes in the Blake lab is direct absorption spectroscopy. An analogy to the Beer-Lambert law of absorption is useful to explain the different components of the experimental apparatus. This law relates the incident intensity of light upon a sample, I_i, with the final transmitted intensity, I_t, given by

$$I_t = I_i \, \mathrm{e}^{-\varepsilon c l}. \tag{2.1}$$

Here, ε is the molar absorption coefficient, c is the concentration of the absorbing species, and l is the pathlength along which light and absorbing species are coincident. The MW and FIR spectrometers differ in their production of I_i and their detection of I_t; c and l remain constant between the two experiments; while ε is VRT eigenstate specific, and depends upon the sample temperature and VRT selection rules and partition functions of the complex. Figure 2.1 diagrams how the various components of the apparatus are connected. Simply by changing the light source and detector, the experiment interchanges from a MW spectrometer to a FIR spectrometer [2]. The other components remain physically in place and consist of: the molecular beam source, which determines ε, c, and l and has three subcomponents—gas supply, planar jet, and vacuum pumps; FM of I_i and lock-in detection of I_t; and a computer with an IEEE-488 interface to control the flow of gases, the scanning rate of I_i, and the acquisition of I_t signal.

2.3 Blake lab MW source and detection

The MW spectrometer used in the Blake lab is a direct absorption apparatus constructed from components used for the FIR spectrometer. It is not the most sensitive

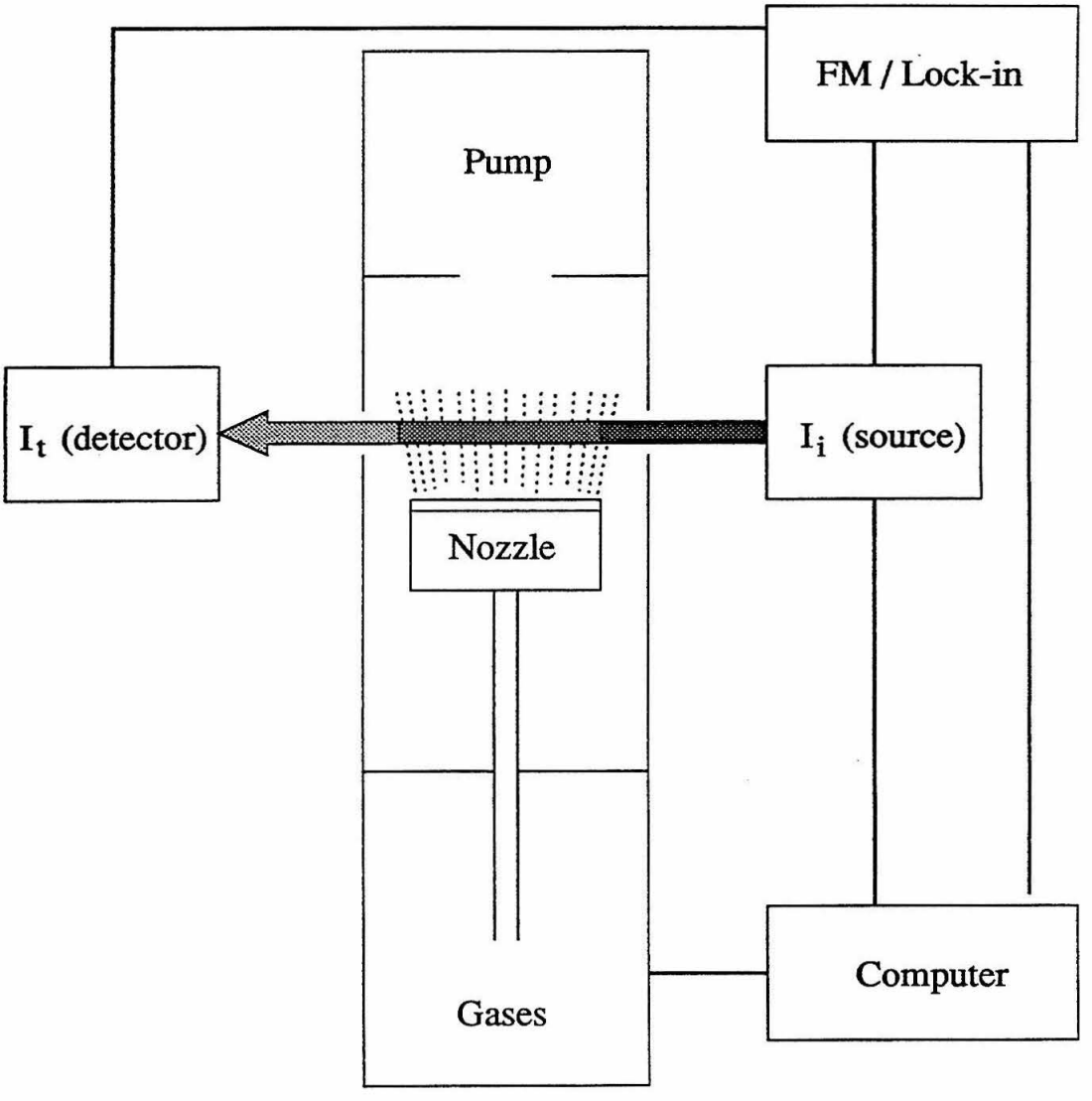

Figure 2.1: Block diagram of the MW/FIR spectrometers.

instrument for measuring the MW spectra of vdW complexes, nor is it even completely optimized (in order to make the conversion between MW and FIR instruments more facile); however, due to its ease of use, automated (and relatively fast) scanning, and higher-than-usual frequency range, the instrument has proven to be quite complimentary to other, more sensitive MW instruments, and also to the VRT studies with the FIR spectrometer. It has been an important asset in my work, providing me the means to measure rotational ground states of vdW clusters and optimize cluster production before begining more difficult FIR experiments. Indeed, MW spectroscopy was responsible for the initial measurements of high-resolution spectra for vdW complexes [3], allowing structures to be determined, and still represents the largest source of new information about vdW complexes, owing to ease of operation and relatively low cost. An FTMW spectrometer was used to collect some of the data used in Chapter 5, and a brief description of this state-of-the art instrument is given in Section 2.8.

The design of the Blake lab MW spectrometer is little different in principle from the earliest of MW spectrometers developed in the late 1940's. In these instruments, MW absorption was measured for species contained within a conducting waveguide. However, in order to detect vdW clusters, they must be cooled well below their dissociative limit. This is accomplished by use of a planar supersonic expansion, discussed below. Instead of being contained within a waveguide, the clusters are now produced inside a free-space cavity formed by sections of waveguide on either side of the jet. These pieces of waveguide are flaired to WR132 dimensions and focused by teflon lenses on either side of the planar jet chamber, forming a Gaussian telescope, in order to match the profile of the expansion.

The MW source (I_i) in the lab is a Wiltron 6747A-20 frequency synthesizer, which puts out approximately +18 dBm (63 mW) between 10 MHz and 20 GHz. The synthesizer relies on a number of narrow band YIG oscillators to cover this range, and each set of oscillators has its own history of performance, which can definitely decline over eight years of hard use. In particular, the band from 9 to 9.5 GHz has minimal power output, and this seems to also affect the harmonic from 19 to 20

GHz to a lesser extent. Another trouble spot is from 10.6 to 10.8 GHz; here, the power is often erratic, and the best performance is achieved with slower scanning rates. From the 0–20 GHz fundamental, harmonics are generated up to 90 GHz (highest detected cluster frequency was for Ar···HF at 79 GHz [4]) using a number of frequency doublers and triplers in conjunction with MW amplifiers. The lowest usable frequency is limited by the waveguide broadcasters and receivers in the lab to approximately 17 GHz. The detection of I_t is accomplished with whisker-contacted Schottky diodes. At frequencies above 60 GHz, the InSb hot electron bolometer, described below, operated at zero field in the Rollin mode can provide improved sensitivity with careful alignment. A more detailed description of the individual components can be found in Bumgarner and Blake [5]. SS also provides a two-page operation procedure for the MW spectrometer.

Detached from the gas lasers of the FIR instrument, the MW spectrometer is completely automated and can scan several GHz a day. Such hands off data accumulation means that ground state rotational spectra for strongly absorbing vdW clusters can be obtained quickly. Also, this spectral region is free of strong water absorptions which can hamper FIR scanning at higher frequencies. A number of material changes could be made to improve the performance of the instrument: primarily the purchase of MW components to improve the power and frequency range. However, these are increasingly unjustified, as the FTWM spectrometers elsewhere have recently improved scanning speed and frequency ranges, and the operators at NIST are friendly in providing members of our group with access and data. The Blake lab MW spectrometer should nevertheless remain useful for the reasons outlined above.

2.4 Blake lab FIR source and detection

The FIR source used in the Blake lab is a CO_2-pumped FIR gas laser. The lasing media are usually small organic molecules which are either gas phase or high vapor pressure liquids at room temperature. Both the CO_2 laser and the FIR laser are discretely line tunable, and continuously tunable FIR output is made by mixing the

laser with the microwave source, described in the previous section, on a Schottky diode. Usable sidebands are separated from the FIR fundamental by a polarizing Martin-Puplett diplexer, and detected with an InSb hot electron bolometer operating in either the Rollin or Putley mode. Each of these important components will be discussed in more detail in the following subsections, and can be seen as a whole in Figure 2.2. The Blake lab FIR spectrometer is an offspring of the parent Berkeley apparatus [6]. This in turn was a modification of the design by Pickett and coworkers at JPL, who also provide a brief review of other previous tunable FIR sources [7]. The present account will include primarily components peculiar to the Blake lab instrument as well as general operating and repair methods. Again, some material will be referenced to SS.

2.4.1 Apollo 150 (75) CO_2 laser

The Apollo 150 CO_2 laser provides radiation between 9 and 11 μm to pump the FIR laser. The CO_2 lasing medium is a mixture of He, N_2, and CO_2, and the reader is refered to [8] for an excellent review of its operation. The radiation is focused and passed onto the FIR laser cavity by three gold coated silicon mirrors as seen in Figure 2.2: the first and third mirrors are flat and the second one has a 1 m focal length. This particular laser is fraught with design flaws covered by SS, and has been a major cause of down time in the lab. The nominal output of the laser exceeded 150 W initially; however current performance is about half of that. There have been numerous failures within the cavity, degredation of the ruled grating and ZnSe output coupler, and diminished pumping speed, which seem to have all contributed to the decrease in performance. While outputs on all FIR lines measured in the Blake lab have not suffered, it may well be that lack of CO_2 pump power prevents us from lasing on transitions with high-gain thresholds. The Coherent power meter and display were recently recalibrated and showed only slight deviation after seven years of use.

Careful monitoring of the CO_2 laser performance is the key to avoiding, or at least anticipating, catastrophic failures. These include maintaining the oil level in the

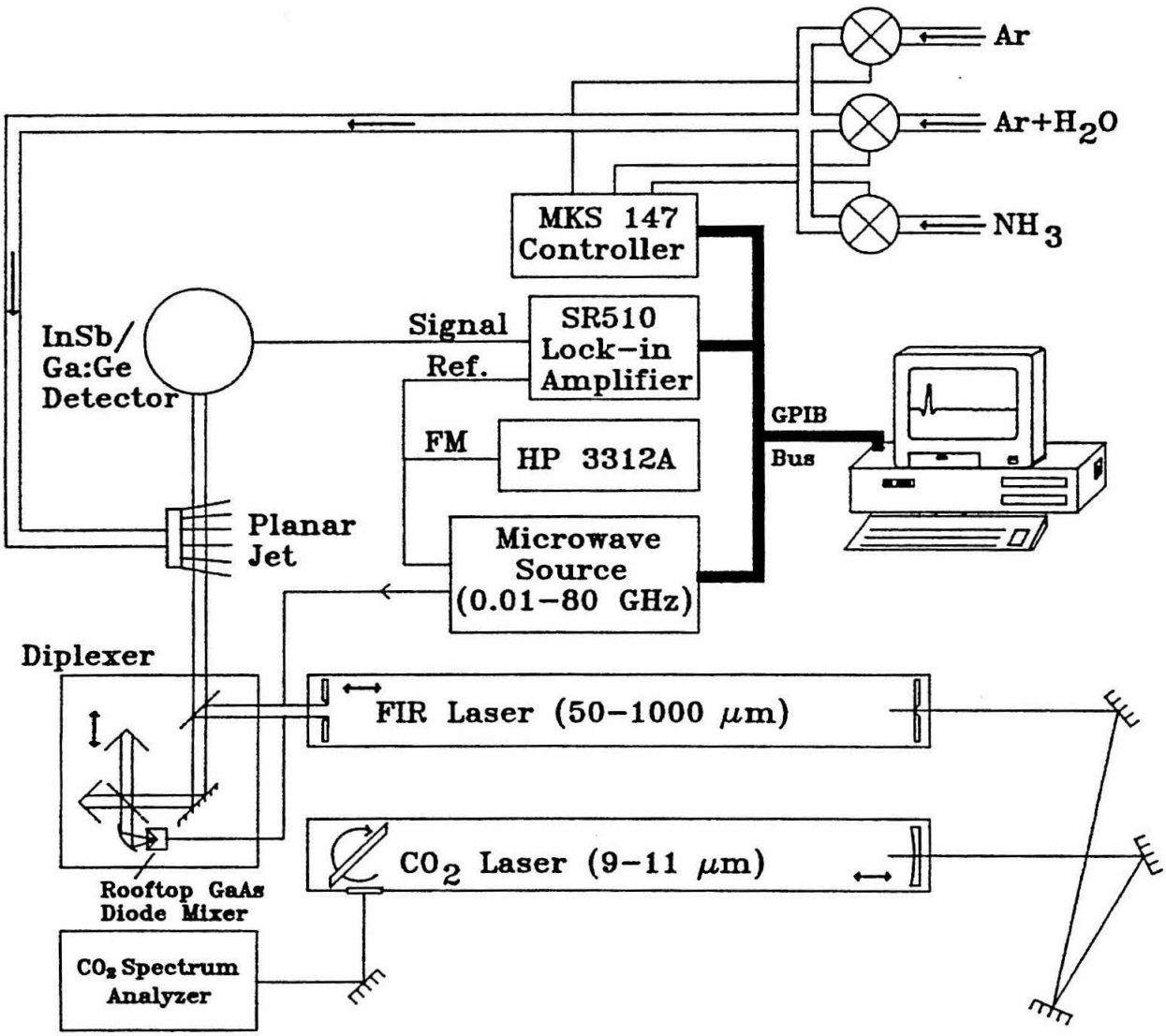

Figure 2.2: Detailed diagram of the FIR laser sideband spectrometer.

cathode housings, especially on the output end of the laser, and also remembering to refill them when the laser is being reassembled. There is a lifetime supply of the cathode oil in a five gallon yellow can marked Shell Dialax AX. Also, one cannot trust the interlock mechanisms to work at all times. The user should ensure an adequate supply of laser gases, as well as check the operation of the Bay Voltex water circulator. The portions of the laser exposed to the circulated water are subject to corrosion and the resulting oxides accumulate in the laser tube. These should be removed when the laser is taken apart for other repairs. The oxides are filtered out of circulation at the Bay Voltex, and the filter cartridges, which are available from Ametek, should be changed as necessary. Finally, the oil in the laser pump should be changed every few months.

Unfortunately, routine maintenance has not been enough to prevent more invasive overhauls of the laser, and the cavity has been taken apart, reassembled, and realigned a number of times. SS gives good advice about the realignment procedure. With experience, one can be prepared for the eventual overhauls. The manual provides quite detailed directions for taking the laser apart and putting it back together. We have accumulated almost all of the o-ring seals used in the cavity. It is a good practice to replace any questionable seals, especially the ones associated with the anode and cathode housings since these are exposed to heat and water, and restock before the next episode. The quartz tubes are precision bored and available from Wilmad Glass of Buena, NJ. For a while, we had replaced the precision bored tubes with pyrex ones without any diminishing effects. However, the original tubes are an odd size (0.570 in. o.d. and 0.050 in. thick), and trusting the less than perfect seal of the pyrex tube led to needlessly crossed fingers. Just keep some of the precision bore tubes on hand. The tubes can be difficult to remove after they have been in service. Apart from careful removal techniques, not much can be done to avoid breaking a tube that is stuck. However, the insertion is made quite easy by having the glass blower bevel any new tubes and using a small amount of cathode oil as a lubricant. All of the plastic tubing parts of the gas circulation are actually plumbing supplies used for swimming pools. The grating and the output coupler have both been replaced

once with parts from the II-VI company. Whenever the cavity is disassembled, one should flush the accumulated oxides from all of the various cooling lines. See also the electrical problems covered by SS.

Lastly, some advice. This laser is an enormous power hog, pulling 20 A of current from the wall and converting it into nearly 100 W of continuous wave (cw) invisible IR photons, which is then focused down to a few square millimeters of beam diameter. Be careful of the current drawn by the laser, and unplug it whenever possible when working on it, making sure to discharge the large capacitors inside the electronics cabinet if the laser has been on recently. If you must work on the laser while it is on, make sure to use the "one hand in the pocket rule." Remember too that the high voltage for the piezo electric drivers is on whenever the initial power is turned on, and not just when the laser high voltage discharge is lit. The cw IR radiation can also be dangerous when misdirected, as the burn marks in the plexiglass output box attest. Whenever there has been any realignment, or even the chance of bumbling hands coming in contact with the folding mirrors, make sure that the full plexiglass box is in place, including the top.

2.4.2 FIR laser cavity

As stated earlier, the Blake lab FIR laser is based on earlier designs [7, 6], and this section will contain primarily those features peculiar to the Blake lab instrument. Briefly, the FIR laser is home-built and constists of a 2.5 m jacketed, water cooled (0 C) pyrex tube with a 1.25 in. o.d. The laser tube projects into sealed aluminum boxes on either end which contain cavity end mirrors and remote controlled motor mikes to control the angular orientation of the gimbel-mounted optics. The laser resonators are cooled with a separate water supply maintained at a few degrees above ambient to avoid condensing vapor onto the optics. The input end mirror is a 2.0 in. o.d. flat copper mirror with a 5.0 mm beveled hole to couple in the CO_2 laser pump beam. As recorded by SS, this mirror has had a few different coatings, all of which seem to work equally well. It is presently sporting a gold top coat.

The design of the output coupler has recently been changed from that used in previous references [9], and the new design is discussed in detail below. The original output coupler consisted of another 2.0 in. gold-coated copper mirror with a 10.0 mm hole blocked by a z-cut quartz optic coated such that it reflects the CO_2 pump radiation and lets about 20% of the FIR radiation pass. The coating had been deteriorating for the last few years, and this spring the z-cut quartz optic eventually cracked. We had tried to replace this optic several years earlier, but the replacement from the same company, Laser Power Optics of San Diego, did not perform well at all. I subsequently learned that their FIR coating has changed in formulation over the years, and they had lost track of what the original coating was. As a replacement, a high purity silicon output coupler was manufactured according to the description of Pugliano [10]. The high purity silicon substrate, which passes FIR light, was obtained as Cold War surplus from Jim Huffmann at the Rockwell International Science Center in Anaheim, CA; a commercial supplier, Lattice Materials of Bozeman, MT, exists for future runs. The output coupler is constructed by masking most of the surface with gold, reflective to both IR and FIR, leaving a small, uncoated hole in the center to pass the FIR laser out of the cavity. The gain of the cavity is then determined by the sizes of the input and output holes relative to the entire cavity. Four different size output couplers were made at the Lawrence Berkeley Laboratory vacuum coating lab by laying down a 5 nm chromium bonding layer and a 650 nm gold coat on top; the copper cavity mirrors were recoated at the same time. The uncoated holes, sizes $\frac{3}{16}$, $\frac{1}{4}$, $\frac{5}{16}$, and $\frac{3}{8}$ in., were masked by disks of ungalvanized sheet metal punched out of a die and held in place with magnets behind the silicon optics. A small amount of CO_2 radiation does leak through the bare silicon, and a piece of z-cut quartz behind the optic prevents the IR leakage from melting a hole in the polyethylene window (again). The initial performance equals or slightly exceeds that of the coated z-cut quartz optic, and is cataloged for three different size output couplers for a series of difluoromethane laser lines in Table 2.1. As seen, the larger output couplers benefit the stronger, lower threshold, laser lines.

The FIR laser cavity is fairly simple and robust, and rarely is the sight of in-

Table 2.1: Schottky diode rectification (mV) for masked output couplers on different difluoromethane lasers.

Laser frequency (GHz)	$\frac{1}{4}''$ hole	$\frac{5}{16}''$ hole	$\frac{3}{8}''$ hole
1042		1100	
1397	600	950	750
1547	100	300	240
1626	450	600	500

strument failure, although realignments are a quick attempt when trouble shooting an ill-defined problem. SS gives a good instruction list for operating and realigning the FIR laser. Here are some additional suggestions. One needs to be careful with the gimbel mounts, as they are no longer supported by the manufacturer. This is especially true for the teflon locking rings, whose fine threads are easy to strip. We are on our last good pair, and gentle care when using the spanning key will save hours of tedious labor in the machine shop making new ones. Also, the motor and encoder mikes are susceptible to corrosion. It would be a good idea to pump and flush the FIR tube after using formic acid lasers and before opening the cavity to atmosphere. These mikes can sometimes be resuscitated with WD-40. The controller for the Oriel mikes also periodically plays dead. Usually after a night's rest, the box has been miraculously healed. Corrosion of the FIR laser mechanical pump can be avoided by using a $N_{2(\ell)}$ trap in front of the pump for formic acid lasers. The cooling lines to the input and output gimbels were originally Tygon tubing, but after a couple years they degraded and one of them burst and flooded the FIR cavity, causing major corrosion damage to the mikes and gimbels. Replacing the tubing inside the cavity with high pressure tubing has worked well for the last four years. When changing laser gases to and from those with labile H and D, it is necessary to wait several hours to several days to fully exchange the hydrogen absorbed on the walls of the cavity. Finally, prior to opening the cavity to atmosphere, warm the pyrex jacket to 50 C in order to prevent adsorption of water onto the cavity surfaces, and when reassembling, allow the cavity to pump down for about an hour at 50 C before cooling back to 0 C.

2.4.3 Sideband generation and separation

In order to do useful spectroscopy with the FIR source described above, the FIR radiation must be made tunable. This is accomplished by mixing the fixed frequency FIR source with the tunable MW source on a Schottky barrier diode; the FIR $\pm$ MW sidebands are then discriminated from the FIR fundamental by a Martin-Puplett polarizing diplexer. The FIR and MW radiation are coupled onto the diode surface by a thin antenna (whisker): the FIR light couples optically with the short arm of the whisker and the MW power is fed onto the whisker via a coaxial connection. Again, the specifics of this mixing and separation have been discussed before [7, 6]. A particularly useful and enlightening resource has been a paper by Zmuidzinas *et al.*, which derives the frequency dependence for the optimum geometry of the whole mixing device [11], and SS gives a good account of the practical implementaion of this theory in our lab. In this section, I will address the etching of the whisker, provide some hints about contacting the whisker with the diode, and give the present focusing scheme for the FIR sidebands.

The whisker and diode are housed in a corner cube reflector designed by Professor Blake and built by Custom Microwave. The reflector serves to focus the FIR radiation onto the whisker. The 1I7 diode obtained from Professor Tom Crowe of the University of Virginia is actually an array of Schottky barrier diode devices with 1.0 μm diameter Pt-Au contacts spaced approximately 1.5 μm apart. Röser provides a good sketch of the epitaxial structure of the diode and the whisker point contact [12]. The Ni-Au whisker is 25 μm in diameter, and therefore must be tapered in order to make a good electrical contact with the diode. This is accomplished by electrochemically etching the whisker in a w/w aqueous solution of 10% KCN and 5% $Fe(CN)_6$.

1. Using double-sided tape, stick a disposable plastic cuvette onto the corner of an adjustble height lab jack.

2. Hook a piece of Pt wire into the cuvette to serve as the anode.

3. Fill the cuvette full of etching solution, leaving a well-formed meniscus.

4. Using a mirror, focus a microscope at 10x to 20x power on the *meniscus* of the etching solution.

5. Position the whisker in the whisker holder close above and normal to the meniscus, and focus the the microscope on the end of the whisker.

6. Attach the positive lead of a power supply set for 12–15 V to the coax connection of the whisker and the negative lead to the Pt wire.

7. Insert the whisker into the solution by adjusting the jack height, and then withdraw until the surface tension of the solution just barely wets the whisker.

8. Turn on the power supply. The etched whisker should spring out of the solution after a few seconds.

The etching process works because the suface tension decreases as the diameter of the whisker is electrochemically reduced. The length of the whisker should be adjusted for the frequency of the laser [11] by etching away the unneeded length. Researchers at UC Berkeley have commented that a 3% solution of HCl and a 7 V potential work as an etching medium as well [10]. A few attempts were made with this simpler, less toxic solution, but the results were not as successful as with the cyanide solution.

Etching the whisker is a somewhat rare event, but contacting the whisker to the diode can be a much more frequent occurrence. Evidence of a good contact is that the bias voltage is 700–750 mV at a few μA current and 900–950 mV at 250 μA; anything outside of these ranges indicates either a bad contact or a weak bias battery. Contacting is most successful after an etching and if performed with the visual aid of the microscope. However, the etched point of the whisker is fairly robust and usually survives many contacting attempts, and it is much less of a hassle to contact the diode *in situ*. In the corner cube, the whisker is stationary and the diode moves along the axis of its post. Its best to mark with a pen the position of the last successful contact before withdrawing the diode for a new attempt. With the diode uncontacted, the bias measures > 1 V at the zero current setting. Patient movement

of the diode axially, as well as rotating, usually finds a good contact. Once the 700–750 mV reading appears, indicating contact, advancing the diode a little bit more can assure a stronger seat. While partial contacts and bad diodes can give supressed biases of < 1 V, experience dictates that anything outside of the 700–750 mV range is not worthwhile. Whenever the whisker in its holder is removed from the corner cube, its position relative to the diode should be realigned under the microscope, using shim stocks between the holder and the corner cube.

The optical path of the FIR sidebands leaving the diplexer are contrained by the fixed position of the FIR laser and the vacuum chamber which contains the planar jet. The location of the FIR laser table and the orientation of the chamber have been changed several times. Figure 2.3 shows the present optical configuration which focuses the sidebands onto the detector while also giving strong cluster signals from the jet. In order to eliminate the possibility of reflecting the sidebands off the face of the nozzle, two cardboard appertures ($\sim$ 1.0 in. diameter) have been placed on either side of the chamber. Throughout the FIR spectrum, atmospheric H_2O absorptions are a nuisance, sometimes attenuating spectral regions of 10 GHz or more. Our solution, though crude, has allowed us to scan within a 100 MHz or so of a strong H_2O line. The exposed optical pathway is encapsulated in plastic sheeting, most conveniently translucent garbage bags, and sealed to the laser table and elsewhere with magnetic strips and tape. This tent is then purged with house air that has been passed through a dry ice/acetone trap. The full purging effect is realized within 2-3 hours. Generally, there is a molecular transition either strong enough or sufficiently removed from the H_2O line, so that the optics can be tweaked before the tent is in place.

2.4.4 InSb hot electron bolometer

The dectector for all of the FIR experiments to date has been a commercial InSb hot electron bolometer from Cochise Instruments of Tucson. These detectors can be operated without (Rollin mode) or with (Putley mode) a permanent magnetic field applied to the detecting element. The greater the magnetic field, the higher in

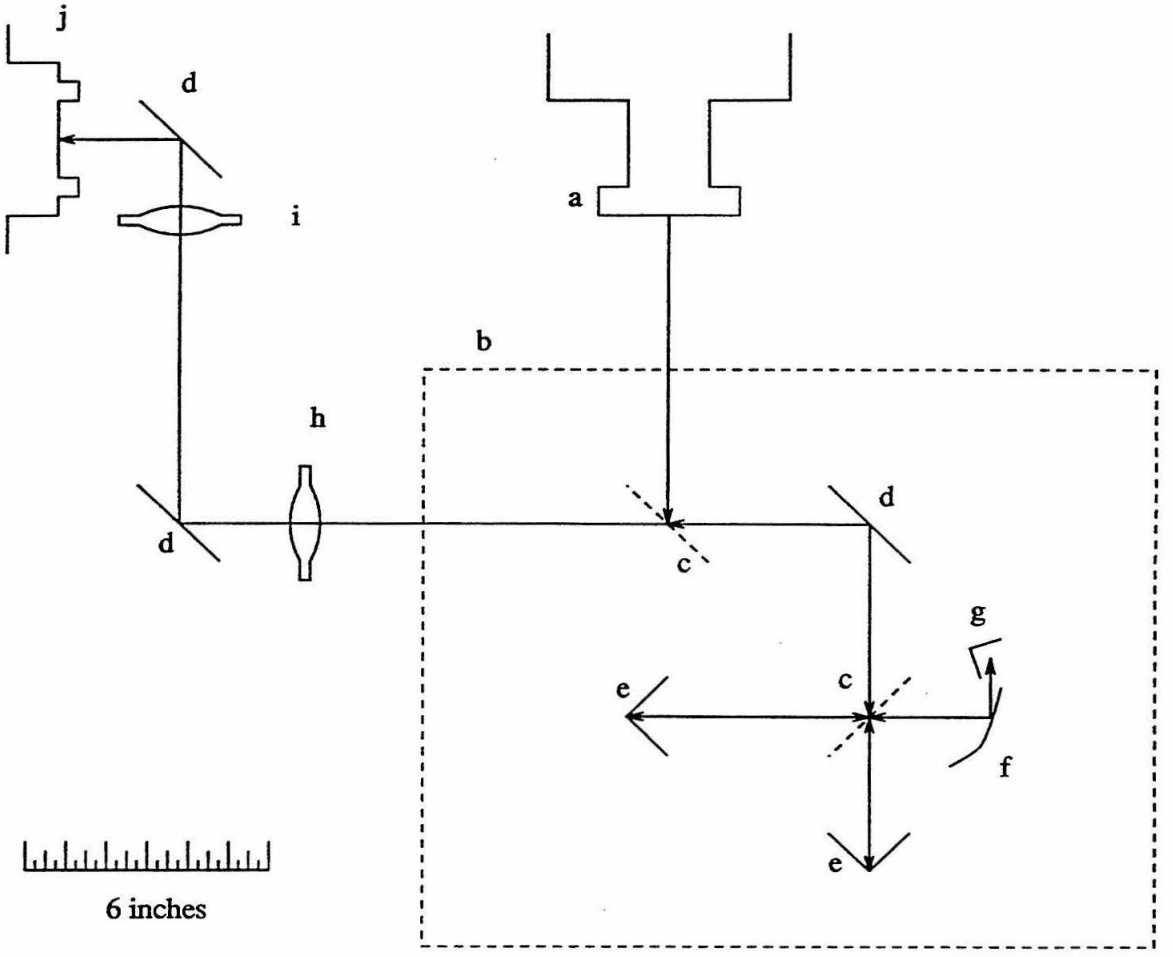

Figure 2.3: Geometry of FIR mixing/focusing optics: a) output from FIR laser cavity, b) raised optical bench for mixing optics, c) 2.0 in free-standing wire polarizers, d) 2.0 in plano mirrors, e) 90° corner reflectors, f) off-axis ellipse, g) corner cube mixer, h) polyethylene lens (r = 2.5 in), i) polyethylene lens (r = 4.5 in), and j) chamber housing planar jet expansion.

frequency the response of the detector. Our detector design employs 0.4 in. diameter $\times$ 0.2 in. long SmCo magnets that are placed 0.1 in. on either side of the InSb element. We measured the surface flux of these magnets and found them to be about 80% of the manufacturer's stated value after several years of use. However, our observed detector response does not correspond well with published values [13]. This may be due to different grades of detecting elements, and volume effects of the detector elements. Empirically, our results can be summarized as follows.

1. Stronger magnetic fields give higher frequency responsitivity.

2. With the 93% (three magnets on each side) of the maximum possible field with the CoSm magnets, detection at 50 cm^{-1} works well.

The work of Brown indicates that a small magnetic field may give stronger response even at low frequencies than operating in the Rollin mode, though we have not made any quanitative measurements [13]. Also, stronger magnets may become available in the near future. One must be careful of the comparisons made by magnet vendors. They quote a magnetic strength term, the maximum energy product, or BH_{max}, which is a measure of the B–H hysteresis curve upon charging the magnet. This does not provide a good comparison of B. The best way to test new magnets is to get one or two magnets and compare their field strength against the SmCo magets directly using a Gauss meter (available from the physics undergraduate lab). We did this with some highly-rated NdFeB magnets and were disappointed.

2.5 Molecular beam

2.5.1 Gas delivery

Gas flow into the supersonic expansion is controlled by four separate MKS 1259B mass flow controllers, allowing us to tailor the chemistry of the molecular beam. These controllers slave to an MKS 147B flow programmer, which is part of the automated spectrometer which enables background (gases off) subtraction. While the flow

controllers are supposed to have been fitted with Kalrez seals, they are *still* susceptible to corrosion. This is a problem when working with water, since even with check valves in place, water vapor inevitably leaks back to the other flow controllers. For using particularly corrosive gases like HF and HCl, stainless steel needle valves were used in place of the flow controllers. The supply gases are typically run at 10–20 psig. Two low-carbon stainless steel lines were installed to fume hood to allow dangerous gases to be used with some modicum of safety. Vapors of chemicals which are liquids at room temperature are introduced by bubbling Ar carrier gas through a trap filled with the liquid. During the last few years, we have used spargers in the water lines in order to increase the amount of vapor entrained.

The flow controllers are a source of downtime due to corrosion—usually the solenoid valve gets stuck open or closed. One should try to prevent any reflux of liquid into the gas lines. Repair is straightforward, with two different possible problems to address. Either the solenoid valve is stuck, or less likely, the mass flow sensor is dirty, in which case the flow will oscillate. The solution to both problems is to take apart the dirty part, clean and replace all of the o-ring seals, and reassemble as per the manual. Fine gauge copper wire and freon (or whatever CFHC equivalent is now available) works well to clean the mass flow tube.

2.5.2 Planar jet

The Ar carrier gas and the clustering gases expand supersonically through a planar jet measuring 2.5 in. long and 0.001 in. wide. The area through which the gases expand is comparable to a pin hole of 1.43 mm diameter. However, there are three distinct advantages for using a planar nozzle *vs.* a pin hole nozzle for direct absorption cluster spectroscopy. First, because the gases expand in only two dimensions for the planar jet, the nonadiabatic cooling process is slower and more gentle, allowing more clustering than a three-dimensional cooling pin hole expansion provides. Second, the planar expansion increases the volume interrogated by the MW or FIR light source, which is in the plane of the expansion and skims the face of the nozzle. Third, in

the region where the clusters are formed, there is very little beam velocity parallel to the light source, and hence no Doppler broadening of the typical 0.75–1.5 MHz linewidths. Busarow [14] and SS analyze the characteristics of the expansion.

There are a number of possible modifications for the planar jet to increase the sensitivity of the experiment. Pulsing the slit valve has the advantage of increasing the backing pressure of the expansion while maintaining the same throughput as the cw expansion, and box-car detection can improve the sensitivity. A number of groups now employ pulsed slits, and use multiple valves and drivers for long slit lengths [15, 16]. The molecular beam is now limited to sources which are either gases or volatile liquids. As one of the focuses of the group has become biologically significant clusters, it would be useful to put larger biological molecules into the gas phase. There are a few different types of sources currently in use, which use heated resevoirs within the nozzle [16] and capillary injection of solutions at the throat of the nozzle [18]. Finally, the signal can be increased by a factor of 2–4 by using some type of multipassing cell [19, 20]. We tried in the past to install such a cell, but the tight dimensions of the present chamber made that impractical.

2.5.3 Pumps

The pumping system for the molecular beam consists of an Edwards EH4200 Roots blower backed by two Edwards E2M275 direct drive mechanical pumps. These are housed on the roof of North Mudd, and the effective pumping speed downstairs in the lab is 1800–2000 cfm. The mechanical pumps have been overhauled twice, and SS gives good instructions. While we have put quite a bit of corrosive material through the pumps, water is their worst enemy. Highly corrosive molecules, like HF and Cl_2, react quickly with the pump oil, protecting the pump itself. Water, however, remains separate from the oil and can dissolve other corrosive materials which can then come in direct contact with the pump. The mechanical pumps seem to have shielded the Roots blower from any harm thus far.

2.6 FM and lock-in detection

The primary detection scheme employed for these experiments, both MW and FIR, is FM of the MW source, usually at 50 kHz, and lock-in detection at twice the FM frequency. The FM driver is an HP 3312A function generator as an outside source for the Wiltron synthesizer, and the lock-in detector is a Stanford Research Systems SR510 instrument. This instrument is controlled via GPIB by an AT clone PC. The lab recently purchased an SR830 with the capability for higher order harmonic detection, but this failed to increase the sensitivity of the instrument.

Several other modulation schemes have been employed. Amplitude modulation of the MW is useful for aligning the flaired microwave horns in the MW spectrometer and for optimizing the production and optical path of the sidebands in the FIR spectrometer. Also, SS built an FM Stark effect driver and Stark plates for use with benzene-water experiments. The achievable field strength near our stainless steel nozzle limits its use to molecules with first-order Stark effects, such as symmetric tops and internal rotors. Both modulation schemes use the HP function generator as a primary source.

2.7 Scanning software and data collection

The Wiltron MW frequency generator, Stanford lock-in, and MKS flow controller are all controlled via GBIP (IEEE-488) connections to the PC clone and by QuickBasic software written Dr. Roger Bumgarner. The core program is called `gtest.bas` and typing `scan` anywhere within DOS will automatically load the bus software and begin the scanning program. From this program, one can define the scanning rate, time constants, sensitivity, direction of the scan (up or down in frequency), signal averaging, and whether background subtraction should be performed with the gases off. Numerous modifications of the code have been made, usually for turning separate gas flows on and off in order to scan for different clusters at the same time or discriminate the chemistry of certain clusters.

The following parameters are typical of how the data used in this thesis were collected. The scanning rate for careful scanning (finding all lines, weak and strong) was 40 MHz for a two minute acquisition window; the pre- and post-time constants were 1.0 s; and lock-in sensitivity was 2 or 5 μV for the MW detectors and 50 or 100 μV for the FIR InSb detector. The FM rate was 50 kHz and detected at the maximum allowed 100 kHz on the lock-in. The FM width was variable, depending empirically upon what maximized the cluster signal for a particular chemistry mixture; a width of 10 kHz FM per MHz of scanning was sure to detect any transition, while higher widths often produced stronger signals.

Because the mixing of the FIR and MW produces both upper (FIR + MW) and lower (FIR - MW) sidebands, the frequency of observed transitions needed to be determined. This was accomplished by pulling the FIR laser cavity to slightly longer or shorter cavity lengths (± 5 μm) with the Oriel encoder mike. In turn, the FIR frequency red shifts or blue shifts, respectively, and the sign and magnitude of the MW compensation gives the sideband designation.

2.8 NIST FTMW spectrometer

Part of the data set for the methanol-water complexes was obtained by researchers at NIST Gaithersburg using their FTMW spectrometer. The instrument is a MW cavity of the Balle-Flyagare type [21], and has been documented extensively in the literature [22]. Since this citation, the instrument has been modified so that the pulsed nozzle expansion is along the FT cavity axis. This orientation allows maximum pathlength interrogation and sub-Doppler linewidths. The instrument was complementary in studying the methanol-water spectra as it provided high resolution (2 kHz) access to the 3–20 GHz frequency range where the lowest-J rotational transitions of the complex lie.

Bibliography

[1] Sakae Suzuki. *Towards a More Quantitative Understanding of Intermolecular Interactions: Biologically Significant Intermolecular Clusters.* PhD thesis, California Institute of Technology, 1996.

[2] This is a truly simple operation. The microwave horns used to broadcast I_i and receive I_t can be placed in the FIR spectrometer set-up with the removal of a single mirror. The only other work is to switch a few SMA and BNC cables.

[3] T.R. Dyke, B.J. Howard, and W. Klemperer. Radiofrequency and Microwave Spectrum of the Hydrogen Fluoride Dimer; a Nonrigid Molecule. *J. Chem. Phys.*, 56:2442, 1972.

[4] P.A. Stockman and G.A. Blake. Improved Ground State Rotational Constants for the Argon- Hydrogen Fluoride Dimer. *J. Chem. Phys.*, 98:4307, 1993.

[5] R.E. Bumgarner and G.A. Blake. Microwave Direct Absorption Sectroscopy of Weakly-Bound Clusters in Planar Supersonic Jet: Spectra of Ar–HCN and $(HCN)_2$ from 17.4 to 76.7 GHz. *Chem. Phys. Lett.*, 161:308, 1989.

[6] G.A. Blake, K.B. Laughlin, R.C. Cohen, K.L. Busarow, D.-H. Gwo, C.A. Schmuttenmaer, D.W. Steyert, and R.J. Saykally. The Berkeley Tunable Far Infrared Laser Spectrometers. *Rev. Sci. Instrum.*, 62:1701, 1991.

[7] J. Farhoomand, G.A. Blake, M.A. Ferking, and H.M. Pickett. Generation of Tunable Laser Sidebands in the Far-Infrared Region. *J. Appl. Phys.*, 57:1763, 1985.

[8] J. Hecht. *The Laser Guidebook.* TAB Books, Blue Ridge Summit, PA, 2nd edition, 1992.

[9] P.A. Stockman, R.E. Bumgarner, S. Suzuki, and G.A. Blake. Microwave and Tunable Far-infrared Laser Spectroscopy of the Ammonia-Water Dimer. *J. Chem. Phys.*, 96:2496, 1992.

[10] Nick Pugliano. *Vibration-Rotation-Tunneling Dynamics in Small Water Clusters.* PhD thesis, University of California, Berkeley, 1992.

[11] J. Zmuidinas, A.L. Betz, and R.T. Borenko. A Corner-Reflector Mixer Mount for Far-Infrared Wavelengths. *Infrared Phys.*, 29:119, 1989.

[12] H.-P. Röser. Heterodyne Spectroscopy for Submillimeter and Far-Infrared Wavelengths from 100 μm to 500 μm. *Infrared Phys.*, 32:385, 1991.

[13] Elliot R. Brown. *Investigation of Bulk Indium Antimonide as a Heterodyne Detector for the Submillimeter Wavelength Region.* PhD thesis, California Institute of Technology, 1985.

[14] Kerry Lynn Busarow. *Tunable Far Infrared Laser Spcetroscopy of Van der Waals Molecules in Planar Supersonic Jet Expansion.* PhD thesis, University of California, Berkeley, 1990.

[15] C.M. Lovejoy and D.J. Nesbitt. Slit Pulsed Valve for Gerneation of Long-Path-Length Supersonic Expansions. *Rev. Sci. Instrum.*, 58:807, 1987.

[16] T.A. Hu, E.L. Chappell, and S.W. Sharpe. Infrared, Diode-Laser Spectroscopy of the Ar-N_2O Complex— Observation of the Intermolecular Bending Mode in Combination with the Highest Frequency Intramolecular Stretching Mode. *Rev. Sci. Instrum.*, 64:3380, 1993.

[17] F.J. Lovas, R.D. Suenram, G.T. Fraser, C.W. Gillies, and J. Zozom. The Microwave Spectrum of Formamide-Water and Formamide-Methanol Complexes. *J. Chem. Phys.*, 88:722, 1988.

[18] J.A. Phillips, M. Cangaratna, H. Goodfriend, and K.R. Leopold. Microwave Detection of a Key Intermediate in the Formation of Atmospheric Sulphuric Acid—The Structure of H_2O-SO_3. *J. Phys. Chem.*, 99:501, 1995.

[19] D. Kaur, A.M. de Souza, S.A. Hammad, L. Mercorelli, and D.S. Perry. Multipass Cell for Molecular Beam Absorption Spectroscopy. *App. Optics*, 29:119, 1990.

[20] Andrew Lloyd Cooksy. *Infrared Laser Spectroscopy of Atomic Carbon and Carbon Clusters.* PhD thesis, University of California, Berkeley, 1990.

[21] T.J. Balle, E.J. Campbell, M.R. Keenan, and W.H. Flygare. A New Method for Observing the Rotational Spectra of Weak Molecular Complexes: Kr-HCl. *J. Chem. Phys.*, 71:2723, 1979.

[22] F.J. Lovas and R.D. Suenram. Pulsed Beam Fourier Transform Microwave Measurements on OCS and Rare Gas Complexes of OCS with Ne, Ar, and Kr. *J. Chem. Phys.*, 87:2010, 1987.

Chapter 3 Vibration-Rotation-Tunneling Spectroscopy and Results for Nitrogen-Water and Carbon Monoxide-Water Dimers

3.1 Introduction

3.1.1 Motivation

The hydrogen-bonding interactions of $OC\cdots H_2O$ and $N_2\cdots H_2O$ provide increased complexity on many levels to the prototypical $Ar\cdots H_2O$ system, and are the next logical step in the progression to larger, more chemically relevant water-containing dimers. In fact, moving from the atom-molecule framework of $Ar\cdots H_2O$ to that of the diatom-molecule dimers is the single largest jump to be made in this study of water-containing dimers. Studies of $OC\cdots H_2O$ and $N_2\cdots H_2O$ are grouped together in this one chapter because of their similiarities in structure, dynamics, and level of understanding. The six corollaries discussed in Section 1.6 indicate the nature of the increased complexity, and primary among these are the existence of "real" intermolecular vibrations akin to covalent vibrations, as seen in Figure 1.2, and the concurrent generation of quantum mechanical tunneling between identical nuclei. These two issues are addressed below.

The substitution of diatomic molecules for argon as hydrogen bond acceptors also increases the level of chemical interaction. While still not the makings of larger, biologically significant interactions, the IPSs of these two vdW complexes do contain information about a number of important chemical interactions. The dynamics of solvation, for example, change dramatically when there are vibrational degrees of freedom available to the solute [1]; and diatom-water complexes are the building blocks for understanding such vibrational motion within an aqueous cage. The

nitrogen-water interaction also is significant in the absorption by atmospheric water lines, causing discrete rovibrational lines of water to pressure broaden into what is termed the water continuum, which occludes much of the IR and FIR transmission through the lower atmosphere. In the complex of carbon monoxide with water there is the addition of a large degree of anisotropy because CO is a heteroatomic molecule with distinct sites of chemical interaction. As shown in Figure 1.3c, the preferred equilibrium structure is a hydrogen bond from water to the carbon end of CO. This interaction is particularly important because of the "water gas shift reaction" which converts gas phase CO and H_2O into CO_2 and H_2. Moreover, the structure of Figure 1.3c, borne out by the research presented in this chapter, indicates that clusters of larger molecules must be studied in order to obtain IPSs relevant to biological problems. Specifically in this case, the $OC\cdots H_2O$ dimer is a poor model for water-carbonyl interactions, since water does not even show a preference for binding with the oxygen end of carbon monoxide. A more chemically intuitive interaction is seen in the complex between water and formaldehyde, which adopts the $H_2CO\cdots H_2O$ structure [2, 3].

The greater stability of the $N_2\cdots H_2O$ and $OC\cdots H_2O$ bonds, compared to those of $Ar\cdots H_2O$, can be predicted from the added dipole-dipole and dipole-quadrupole electrostatic interactions present. Such forces also align the dimer's heavy atoms in a nearly linear array. Since these complexes do have permanent electrostactic moments, and the multipole moments of the constituent monomer units are known, it is possible to *a priori* estimate the relative magnitude of the attractive forces of the dimer pairs [4, 5, 6]. Figure 3.1 illustrates the most favorable dipole-dipole and dipole-quadrupole interaction geometries and calculates the relative electrostatic forces present in the $N_2\cdots H_2O$, $OC\cdots H_2O$, and $H_2O\cdots HOH$ complexes. Note that the negative value of the quadrupole moments for N_2 and CO cause them to align their diatomic axes with the H—O bond axis [7]. Also notable is the comparable size of the dipole-quadrupole forces of $N_2\cdots H_2O$ and $OC\cdots H_2O$ with the dipole-dipole force associated with the $H_2O\cdots HOH$, 35% and 60% respectively, and that the $OC\cdots H_2O$ dipole-quadrupole interaction is nearly ten times that of the dipole-dipole interaction.

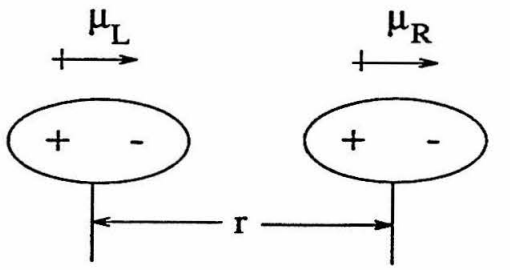

$$-\frac{2\mu_L\mu_R}{r^3}$$ dipole-dipole

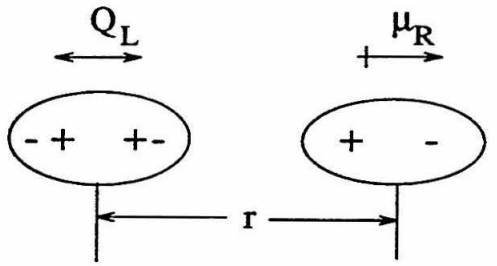

$$\frac{3Q_L\mu_R}{r^4}$$ dipole-quadrupole

	μ /Cm	Q/Cm^2
N_2		-5.07×10^{-40}
CO	0.37×10^{-30}	-8.34×10^{-40}
H_2O	6.14×10^{-30}	

$r \approx 3.5$ Å $= 3.5 \times 10^{-10}$ m

	$N_2 \cdots H_2O$	$OC \cdots H_2O$	$(H_2O)_2$
dipole-dipole *		1.06	17.6
dipole-quadrupole *	6.22	10.2	

* units = 10^{-31} C^2/m

Figure 3.1: Multipole moments and interaction geometries for nitrogen-water, carbon monoxide-water, and water-water complexes.

Table 3.1: Colligative properties of Ar, N_2, and CO.

Species	Melting point (°C)	Boiling point (°C)
N_2	-210	-196
CO	-199	-192
Ar	-189	-186

The difference in strength between the Ar-water and diatomic-water complexes is not predicted, however, by their colligative properties. Table 3.1 shows the melting and boiling points for Ar, CO, and N_2. They are all very similar, within 5 % of each other. In fact, Ar is the least volatile of the three. The many-body effects in the dispersion forces of $Ar_{(\ell)}$ are evident, and show the need to study trimers and larger order clusters as discussed in Chapter 6.

3.1.2 Vibration-rotation frameworks

The stronger vdW bonding interactions in $N_2 \cdots H_2O$ and $OC \cdots H_2O$ make the hindered rotor framework used for $Ar \cdots H_2O$ inappropriate for describing the intermolecular vibrations and rotations of these more strongly bound complexes. Instead, the intermolecular motions of the subunits with respect to each other are modeled as vibrations, with separate rotational manifolds to describe the overall rotation of the bound complex. Figure 3.2 shows the differences in these frameworks for the rotation about the b-axis of water in a bound complex. Quantum mechanically, these differences are manifested in the ability or inability of the wavefunction to sample all angular coordinates freely. As noted in Section 1.4, and made clear by Figure 3.2, however, intermolecular vibrations can have wide amplitude wavefunction distributions, even in the lowest vibrational levels.

In order to provide an accurate basis for normal mode analyses of these clusters, their intermolecular geometry must be determined. Because of the great disparity of energy between intra- and intermolecular vibrations, it is correct to decouple them, and so the most appropriate set of structural parameters is the relative orientation of one subunit towards the other. Such a scheme is illustrated in Figure 3.3a and

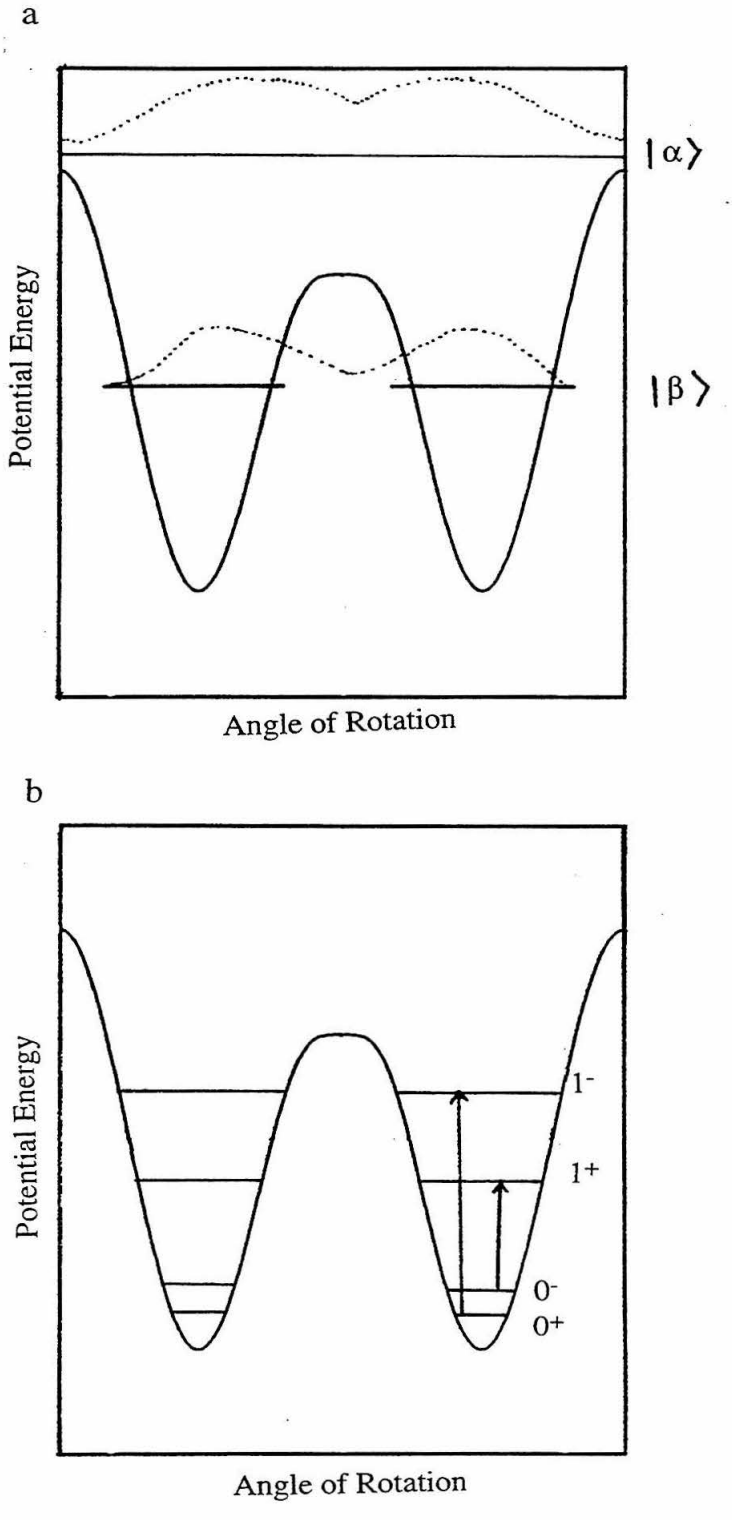

Figure 3.2: Energy levels and wavefunctions for different water rotors: a) hindered $|\alpha\rangle$, bound $|\beta\rangle$, and b) tunneling water rotors.

b. Here, R is the intermolecular separation of the centers-of-mass between the two subunits, and $\theta_{\alpha,\beta}$ and $\phi_{\alpha,\beta}$ are the in-plane and out-of-plane rotations of the subunits with respect to R for each subunit A and B. $\theta = 0°$ is defined for water as the bidentate configuration with the water b-axis parallel to R, and for N_2 and CO as the configuration with the diatomic axis parallel to R; $\phi = 0°$ is defined as the coplanar configuration for both subunits.

An additional consequence of the quenching of free monomer rotations is the creation of equivalent bound states of the complex when there are chemically identical nuclei, such as the hydrogens in H_2O as well as the nitrogens in N_2. Because of the non-classical nature of the vibrational wavefunctions, vibrational amplitude extends past the inside potential wall and into the barrier. When the overlap between two wells is substantial, tunneling between the equivalent conformations can occur, and the vibrational eigenstates are split into tunneling sublevels in order to satisfy the Pauli exclusion principle. This is shown in Figure 3.2b. Vibrational states above the tunneling barrier no longer support tunneling *per se*, and hence have no tunneling splittings; however, the energy spacings and wavefunction amplitudes continue to be affected by the structure of the potential. Therefore, one potential can, theoretically, support internal rotation, vibration, and tunneling, depending upon the reduced masses and barrier heights involved. This is a particularly important consideration for the study of $N_2 \cdots H_2O$ and $OC \cdots H_2O$, as the intermolecular bending modes couple tunneling modes from several degrees of freedom.

3.1.3 Tunneling frameworks

PI theory, via the formulation of molecular symmetry groups, is used to describe the large amplitude motions which interconvert equivalent frameworks in vdW complexes. In addition to molecular point groups, which account for the exchange of identical nuclei by rigid body rotations, molecular symmetry groups also include all possible permutations of identical nuclei, regardless of whether or not the exchange pathway includes inversion. The difference between the two theories can be seen in their

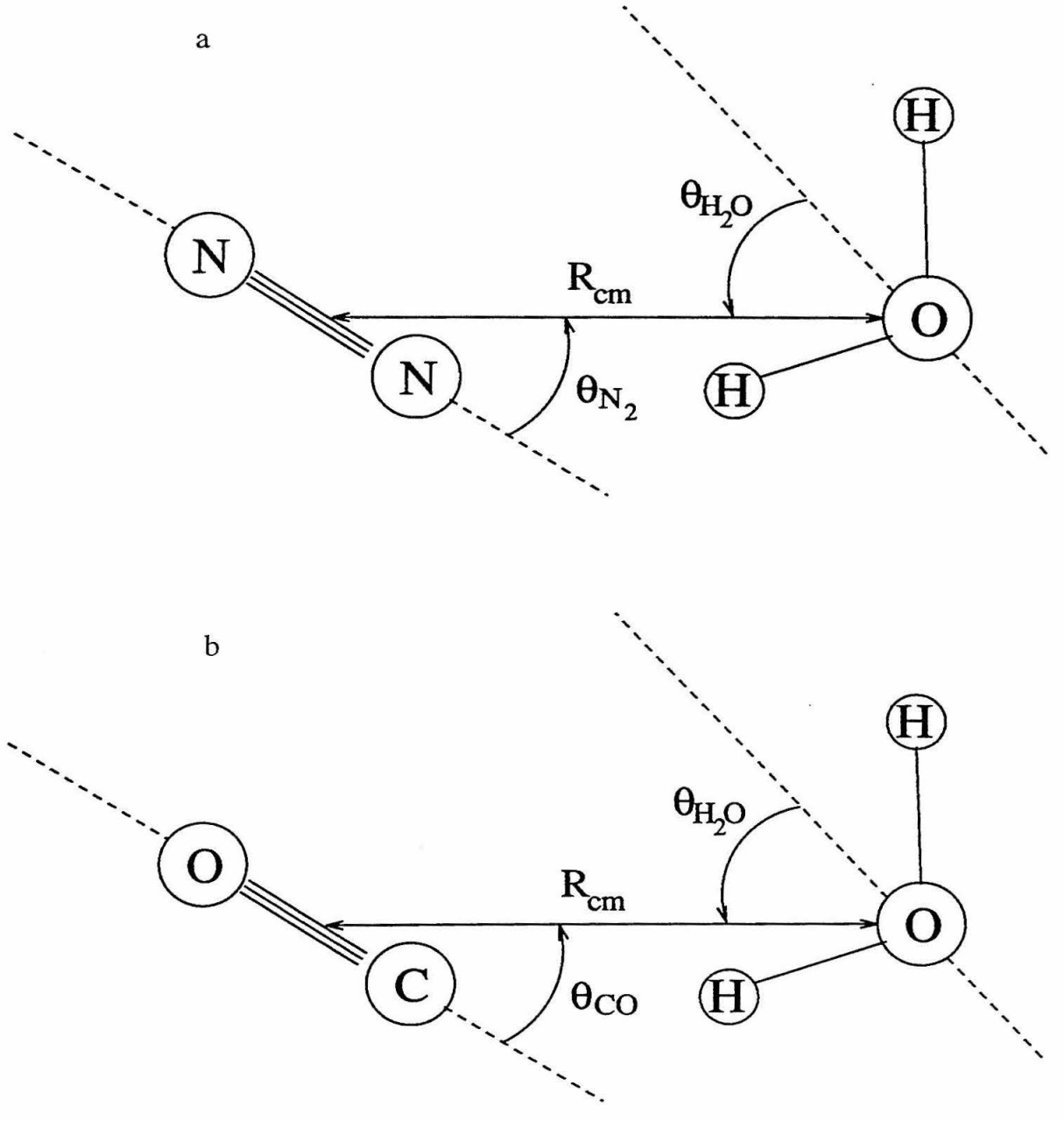

Figure 3.3: Structural parameters for a) $N_2 \cdots H_2O$, and b) $OC \cdots H_2O$ complexes.

treatment of the ammonia monomer. Rigid ammonia has the same C_{3v} molecular point group as methyl fluoride, but the C_{3v} group does not account for the doubling of the ground state and $\nu_2 = 1$ modes by inversion tunneling. The molecular symmetry group for ammonia, D_{3h}, includes inversion, and applying PI theory to ammonia correctly gives the symmetry allowed inversion transitions and spin weightings. An excellent resource for the general application of PI theory is *Molecular Symmetry and Spectroscopy* by P.R. Bunker [10].

To count the number of possible tunneling splittings of a vdW complex, one must first identify all equivalent frameworks of the complex and then determine which interchange pathways are feasible, that is, which barriers are low and narrow enough to allow significant wavefunction overlap. Figure 3.4 diagrams the equivalent frameworks for the various isotopomers of the carbon monoxide-water and nitrogen-water dimers. Note that this assignment breaks the isotopomers into three different sets: $N_2\cdots H_2O$ and $N_2\cdots D_2O$, with two pairs of equivalent nuclei, have four equivalent tunneling frameworks; $N_2\cdots DOH$, $OC\cdots H_2O$, and $OC\cdots D_2O$, with one pair of equivalent nuclei, have two equivalent tunneling frameworks; and $OC\cdots DOH$ has no equivalent nuclei, and therefore does not undergo tunneling.

The next step is to determine by what pathways the equivalent frameworks can feasibly interconvert. For vdW complexes at low temperatures, *feasible* means that vdW bonds may be broken, but covalent ones cannot. Looking to Figure 3.4, we see that there are three distinct pathways available for this set of complexes. In $N_2\cdots DOH$, the nitrogen nuclei can interchange by an acceptor tunneling pathway, and in $OC\cdots H_2O$ and $OC\cdots D_2O$, the hydrogens can interchange by a donor pathway. With pairs of equivalent nuclei in both the acceptor and the donor subunits, $N_2\cdots H_2O$ and $N_2\cdots D_2O$ can interchange frameworks by both acceptor and donor pathways, as well as a geared pathway which swaps both pair of nuclei simultaneously. This geared pathway is not unique, however, since it is equivalent to successive acceptor and donor tunneling motions. Each unique tunneling pathway between sets of two identical nuclei results in two non-degenerate tunneling levels, so the isotopomers with either acceptor or donor tunneling pathways have two tunneling states, and those

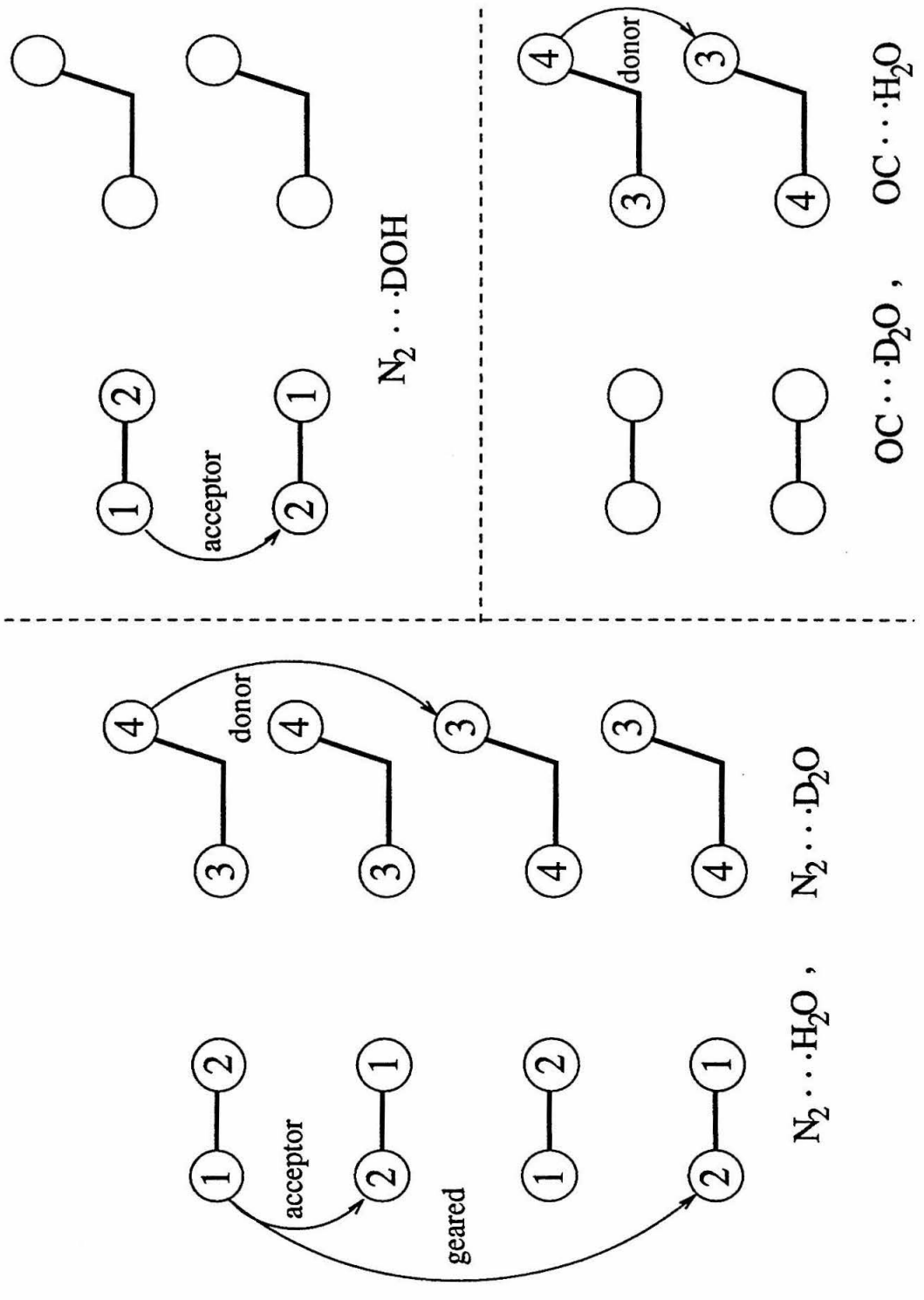

Figure 3.4: Tunneling frameworks for isotopomers of nitrogen-water and carbon monoxide-water complexes.

Table 3.2: PI theory correlations between nitrogen-water and carbon monoxide-water dimers and the mixed water dimers.

Dimer	Corresponding water dimer	Nuclear spin weights	Selection rules
$N_2\cdots H_2O$	$D_2O\cdots H_2O$	$A_1^{\pm}(2)$ $A_2^{\pm}(1)$ $B_1^{\pm}(6)$ $B_2^{\pm}(3)$	$A_1^{+}\leftrightarrow A_1^{-}$ $A_2^{+}\leftrightarrow A_2^{-}$ $B_1^{+}\leftrightarrow B_1^{-}$ $B_2^{+}\leftrightarrow B_2^{-}$
$N_2\cdots DOH$	$D_2O\cdots DOH$	$A_1^{\pm}(2)$ $A_2^{\pm}(1)$	$A_1^{+}\leftrightarrow A_1^{-}$ $A_2^{+}\leftrightarrow A_2^{-}$
$N_2\cdots D_2O$	$D_2O\cdots D_2O$	$A_1^{\pm}(4)$ $A_2^{\pm}(2)$ $B_1^{\pm}(2)$ $B_2^{\pm}(1)$	$A_1^{+}\leftrightarrow A_1^{-}$ $A_2^{+}\leftrightarrow A_2^{-}$ $B_1^{+}\leftrightarrow B_1^{-}$ $B_2^{+}\leftrightarrow B_2^{-}$
$OC\cdots H_2O$	$DOH\cdots H_2O$	$A^{\pm}(1)$ $B^{\pm}(3)$	$A^{+}\leftrightarrow A^{-}$ $B^{+}\leftrightarrow B^{-}$
$OC\cdots D_2O$	$DOH\cdots D_2O$	$A^{\pm}(2)$ $B^{\pm}(1)$	$A^{+}\leftrightarrow A^{-}$ $B^{+}\leftrightarrow B^{-}$

with both pathways operative have four tunneling states. Therefore, each rotational or rovibrational transition for these complexes should have either four or two or one set(s) of tunneling components, depending on the number of pairs of identical nuclei.

After determining the number of tunneling states for each isotopomer, we next must assign to them symmetry labels and statistical weights. This is accomplished by determining the molecular symmetry group associated with the number and type of unique, feasible operations, and then obtaining the nuclear spin statistics for each symmetry element. Finally, one needs to derive the selection rules which connect states of different symmetries. This work has already been accomplished for the complete set of water dimer isotopomers [9, 10], and fortuitously all of the PI theory for the nitrogen-water and carbon monoxide-water dimers is completely analogous to that for the water dimers. By substituting D_2O for N_2, both of which have pairs of spin I = 1 particles, and DOH for CO, one can find the correct analog. For example, the analog for $N_2\cdots H_2O$ is $DOD\cdots H_2O$ and for $OC\cdots D_2O$ it is $HOD\cdots D_2O$. Table 3.2 lists all of the appropriate analogies, and includes the nuclear spin weights and selection rules.

3.2 Previous microwave experiments

Two seminal MW investigations preceded the FIR spectral measurements discussed in this chapter. These works were particularly useful in the initial phase of the FIR experiments because the more accurate relative intensity measurements in the MW data enabled unambiguous symmetry labels to be assigned to individual sets of rotational transitions. In turn, the FIR data could be assigned to symmetry states by the method of combination differences tied to the MW data. In this section, I will present a brief, annotated summary of the results of these two studies.

Leung and coworkers measured the MW spectra of several different isotopomers of the nitrogen-water complex using the NIST FTMW spectrometer [11]. They recorded a-type rotational transitions ($J = 0 \rightarrow 1$ to $J = 3 \rightarrow 4$) for the following isotopomers: $N_2 \cdots H_2O$, $^{15}N_2 \cdots H_2O$, $N_2 \cdots H_2{}^{17}O$, $N_2 \cdots D_2O$, $N_2 \cdots DOH$, ^{14}N—$^{15}N \cdots H_2O$, and ^{15}N—$^{14}N \cdots H_2O$. Careful intensity measurements of the tunneling splittings of the $J = 0 \rightarrow 1$ transition of $^{15}N_2 \cdots H_2O$, which lacks the much larger nuclear hyperfine interactions of the ^{14}N nuclei, provided the 1:3:3:9 intensity ratio associated with the tunneling of two pairs of $I = \frac{1}{2}$ fermions, and allowed the assignment of the appropriate symmetry labels. Using this isotopomer as a reference, the tunneling splittings of the remaining six isotopomers were assigned. A dipole moment of 0.833 D was measured along the a-axis of the complex as well as the nuclear quadrupole coupling constants for the ^{14}N, ^{17}O, and D nuclei along the a-axis. Note that only the D-bound conformer of $N_2 \cdots DOH$ was observed, but that both ^{14}N—$^{15}N \cdots H_2O$ and ^{15}N—$^{14}N \cdots H_2O$ were detected. This indicates that the internal rotation of nitrogen and water are quenched by the complex formation, *i.e.*, distinct conformers were observed instead of averaged structures. The large D/H isotope effect present in complex formation yields only the D-bound conformer; the $^{15}N/^{14}N$ isotope effect is not nearly as large, and allows both conformers to form in large amounts. Leung *et al.* also noted that monomer related molecular parameters, such as tunneling splittings and nuclear quadrupole coupling constants, were dependent upon the tunneling state of the other subunit in the complex. This suggests that water tunneling and nitrogen tunneling may

be correlated in some ways. Finally, they made some attempt at determining the equilibrium structure. A planar geometry was assumed for the complex, because the a-type MW rotational data offered no information of the orientation of the subunits about R. From the $\bar{B} = (B+C)/2$ rotational constants measured, an $R_{N\cdots H}$ distance of 2.45± 0.10 Å was calculated. The values of the nuclear quadrupole coupling constants along the a-axis were used to determine the values of $\langle\theta_{N_2}\rangle$ and $\langle\theta_{H_2O}\rangle$. $\langle\theta_{H_2O}\rangle$ was found to be 59°, however, because of the coupling of $eQq_a(^{14}N)$ to the water tunneling states, the derived value of $\langle\theta_{N_2}\rangle = 21°$ was considered questionable.

Subsequently, Yaron and coworkers studied five different isotopomers of the carbon monoxide-water complex—OC···H_2O, ^{13}OC···H_2O, OC···DOH, ^{13}CO···DOH, and OC···D_2O—again using the NIST FTMW spectrometer as well as a molecular beam electric resonance (MBER) spectrometer [12, 13]. Rotational a-type transitions ($J = 0 \rightarrow 1$ to $J = 2 \rightarrow 3$) yielded similar information about this complex as did the previous $N_2\cdots H_2O$ experiments. This time, spin-spin hyperfine interactions between the two protons on the water subunit led to the assignment of the correct symmetery labels. The dipole moment along the a-axis was measured as 1.04 D, and eQq_a was measured for the deuterium labeled compounds. Again, only D-bound conformers of complexes with DOH were observed. The structure was determined from $\bar{B}$ rotational constants and deuterium quadrupole coupling constants, and as with nitrogen-water, the complex was assumed to be planar and θ_{CO} set to 0°. $R_{C\cdots H}$ was calculated to be 2.41 Å, and θ_{H_2O} had a best fit value of 64°, slightly more tilted than the hydrogen bond of $N_2\cdots H_2O$. Using a one-dimensional potential dependent upon the small differences in the dipole moments for the A and B symmetry states for both OC···H_2O and OC···D_2O, Yaron *et al.* modeled the water tunneling potential. Results from this potential predicted that the tunneling splitting for OC···H_2O is 17(1) GHz and for OC···D_2O is 1.1(1) GHz.

3.3 FIR observation of rotation-tunneling modes

3.3.1 Observed data and experimental conditions

The full structures intimated by the MW results of the last section for $N_2\cdots H_2O$ and $OC\cdots H_2O$ suggest a nearly linear arrangement of all of the atoms except for the non-bonding hydrogen atom. This structure is reminiscent of that of hydrazoic acid, HN_3, and like this molecule, the two vdW complexes have b-type rotational spectra in the FIR. Data were collected for complexes with three different types of water isotopomers—H_2O, DOH, and D_2O— as well as naturally abundant (1.1 %) ^{13}C. The "bone dry" N_2 from campus sources and CO, from Matheson Gases, were obtained with little regard for purity except dryness; D_2O (99.5 %) was obtained from Cambridge Isotope Laboratories, while DOH was made by mixing equal portions of H_2O and D_2O. The water vapor was placed into the gas stream before the planar nozzle by bubbling Ar through a resevoir of water. The mixing ratio of gases initially used in these experiments was 3.25 standard liters per minute (slm) Ar/6.6 slm Ar + H_2O/0.235 slm N_2 for $N_2\cdots H_2O$ and 5.2 slm Ar/1.289 slm Ar + H_2O/0.219 slm CO for $OC\cdots H_2O$. Since these data were recorded, higher Ar backing pressures and gas spargers have been used, changing the optimal cluster-forming conditions to 1.0 slm Ar/9.0 slm Ar + H_2O/0.720 slm N_2 for $N_2\cdots H_2O$ and 3.5 slm Ar/6.0 slm Ar + H_2O/0.500 slm CO for $OC\cdots H_2O$. These expansion conditions were first optimized on MW transitions, and the a-type rotational data measurements for the $N_2\cdots H_2O$ and $OC\cdots H_2O$ isotopomers were then extended to $J = 9 \rightarrow 10$ for $N_2\cdots H_2O$ and $J = 12 \rightarrow 13$ for $OC\cdots H_2O$. The initial structures from the MW papers predicted the location of the $K_P = 1 \leftarrow 0$ transitions fairly well, and the rotation-tunneling bands were located with little trouble. All of the PI predicted tunneling bands were observed and Figure 3.5 summarizes the observed b-type spectra for the various isotopomers of the nitrogen-water and carbon monoxide-water complexes. Two FIR laser lines—584388.2 MHz (HCOOH) and 420404.0 MHz (DCOOH)—were used. $N_2\cdots D_2O$ and $OC\cdots D_2O$ transitions below 360 GHz were observed using the second lower MW sideband off of the 420 GHz line. All of the assigned and fit

data are recorded sequentially in Tables 3.3–3.10: $N_2\cdots H_2O$, $N_2\cdots DOH$, $N_2\cdots D_2O$, $OC\cdots H_2O$, $^{13}OC\cdots H_2O$, $OC\cdots DOH$, and $OC\cdots D_2O$. Nuclear hyperfine structure from the $^{14}N_2$ nuclei were apparent but not fully resolved for low J nitrogen-water transitions, and listed frequencies represent estimated line centers.

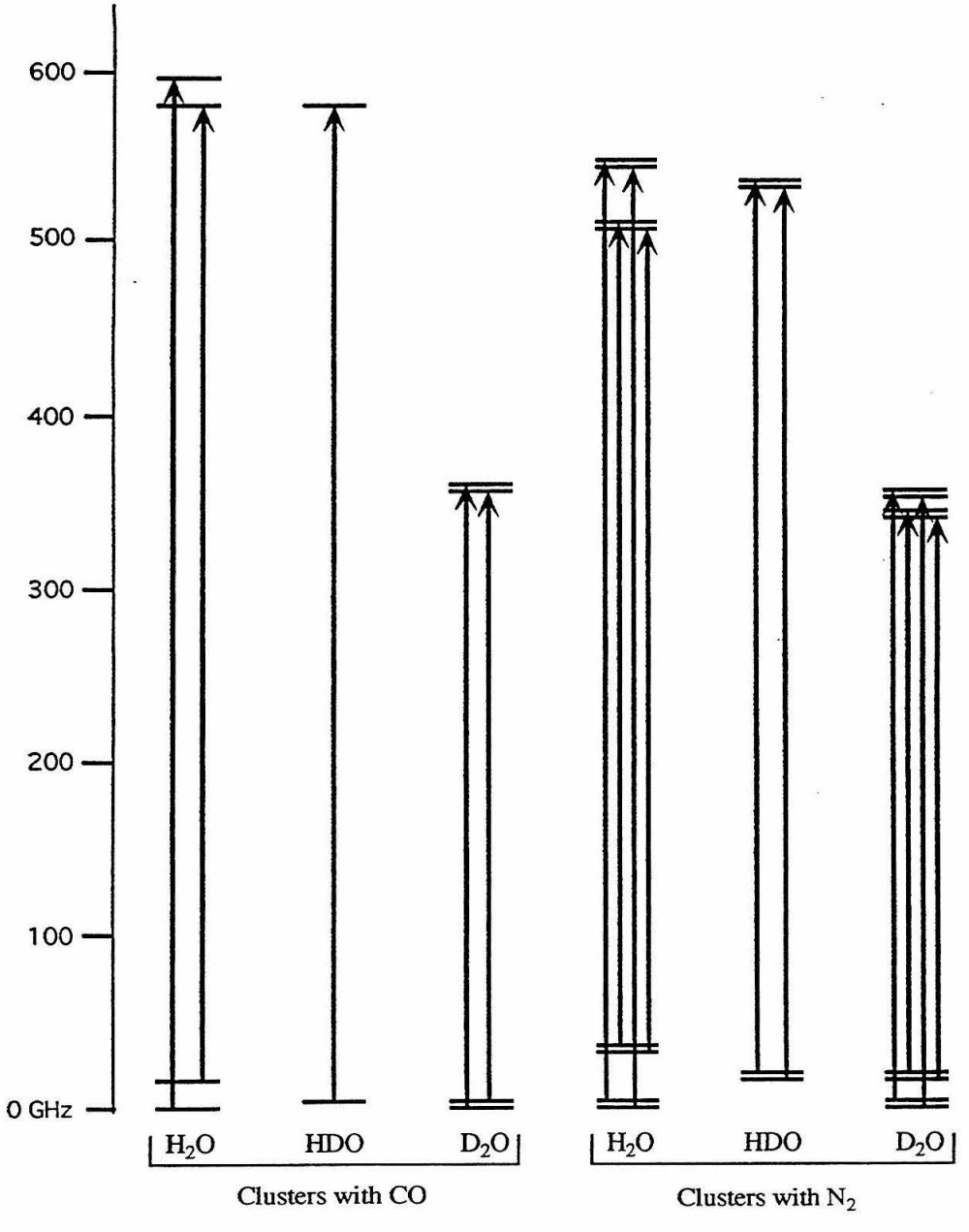

Figure 3.5: Summary of observed b-type spectra for isotopomers of nitrogen-water and carbon monoxide-water complexes. Note, spectra were also observed for $^{13}OC\cdots H_2O$ which nearly overlap with those for the normal isotopomer.

Table 3.3: MW and FIR rotational-tunneling transitions of $N_2 \cdots H_2O$. "O–C" are the observed frequencies minus the frequencies calculated with the fit parameters. All units are in MHz. Transitions are labeled with the notation ${}^{\Delta K}\Delta J_{K''}(J'')$, and frequencies marked with an asterisk are from Leung *et al.*

	A_1		A_2		B_1		B_2	
	Observed	O–C	Observed	O–C	Observed	O–C	Observed	O–C
${}^{Q}R_0(0)$	5813.677*	0.00	5812.556*	0.00	5828.121*	0.00	5828.332*	0.00
${}^{Q}R_0(1)$	11626.309*	0.00	11624.110*	0.00	11655.219*	0.00	11655.632*	0.00
${}^{Q}R_0(2)$	17436.855*	0.00	17433.656*	0.00				
${}^{Q}R_0(3)$	23244.37	0.09	23240.25	0.05	23302.28	0.01	23303.16	0.12
${}^{Q}R_0(4)$	29047.68	0.11	29042.86	0.12	29120.24	0.04	29121.28	0.17
${}^{Q}R_0(5)$	34845.84	0.14	34840.42	0.12	34933.14	0.08	34934.17	0.09
${}^{Q}R_0(6)$	40637.83	0.13	40631.94	0.05	40739.94	0.07	40741.08	0.12
${}^{Q}R_0(7)$	46422.75	0.16	46416.94	0.39	46539.61	-0.03	46540.85	0.08
${}^{Q}R_0(8)$	52199.49	0.05	52193.25	-0.06	52331.47	0.06	52332.72	0.16
${}^{Q}R_0(9)$	57967.23	-0.10	57961.15	-0.08	58114.20	-0.05	58115.31	-0.07
${}^{R}P_0(8)$					432586.19	0.04	432737.93	0.12
${}^{R}P_0(7)$					437668.45	-0.03	437840.46	0.11
${}^{R}P_0(6)$					442853.28	-0.08	443044.39	0.01
${}^{R}P_0(5)$					448142.91	0.00	448351.09	-0.16
${}^{R}P_0(4)$					453538.86	0.02	453761.79	-0.16
${}^{R}P_0(3)$					459042.28	-0.09	459277.19	0.06
${}^{R}P_0(2)$	528471.44	-1.24	527132.51	0.39	464653.68	-0.47	464897.24	0.22
${}^{R}Q_0(1)$	540158.48	0.18	538803.71	0.20	476337.92	-0.26	476582.94	0.18
${}^{R}Q_0(2)$	540559.52	0.22	539233.70	0.24	476608.80	-0.08	476848.16	0.11
${}^{R}Q_0(3)$	541159.64	0.34	539876.12	0.31	477012.93	-0.01	477244.37	0.14
${}^{R}Q_0(4)$	541956.89	0.40	540727.58	0.11	477548.04	0.02	477769.34	0.15
${}^{R}Q_0(5)$	542948.81	0.37	541784.27	-0.06	478211.05	0.02	478420.11	-0.04
${}^{R}Q_0(6)$	544132.19	0.06	543040.73	-0.50	478998.21	0.00	479193.68	-0.03
${}^{R}Q_0(7)$	545503.66	-0.28	544492.26	0.26	479905.05	-0.05	480085.81	-0.04
${}^{R}Q_0(8)$	547059.20	-0.43			480926.82	0.11	481091.91	-0.04
${}^{R}Q_0(9)$	548794.16	-0.20			482057.46	-0.04	482206.89	-0.03
${}^{R}Q_0(10)$	550703.00	0.33			483291.49	0.01	483425.14	-0.04
${}^{R}Q_0(11)$					484622.25	-0.09	484740.77	0.07
${}^{R}Q_0(12)$					486043.62	0.10	486147.20	0.02
${}^{R}Q_0(13)$					487548.23	-0.04	487637.96	-0.02
${}^{R}R_0(0)$	545913.06	0.39	544568.36	-0.43	482137.96	0.47	482380.80	-0.18
${}^{R}R_0(1)$	552007.76	-0.44	550714.78	-0.90	488178.10	0.24	488413.35	-0.29
${}^{R}R_0(2)$					494321.67	0.27	494545.70	-0.17
${}^{R}R_0(3)$	564615.60	0.31	563494.56	0.47	500565.45	0.06	500775.33	-0.07
${}^{R}R_0(4)$	571124.16	0.07	570116.04	-0.02	506906.60	-0.03	507099.62	0.05
${}^{R}R_0(5)$	577767.68	-0.09	576884.97	-0.08	513341.32	-0.10	513515.53	0.14
${}^{R}R_0(6)$					519865.59	-0.07	520019.63	0.09
${}^{R}R_0(7)$					526474.98	0.07	526608.26	-0.19

Table 3.4: FIR rotational-tunneling transitions of $N_2 \cdots DOH$. "O–C" are the observed frequencies minus the frequencies calculated with the fit parameters. All units are in MHz. Transitions are labeled with the notation ${}^{\Delta K}\Delta J_{K''}(J'')$.

Assignment	A_1 Observed	O–C	A_2 Observed	O–C
${}^{R}P_0(12)$	457378.01	0.14	457380.12	0.16
${}^{R}P_0(11)$	462201.95	0.10	462204.98	0.05
${}^{R}P_0(10)$	467106.56	-0.36	467110.82	-0.37
${}^{R}P_0(9)$	472094.00	-0.85	472099.58	-0.82
${}^{R}P_0(8)$	477168.17	1.02	477174.98	1.00
${}^{R}P_0(7)$	482325.12	0.06	482333.08	0.00
${}^{R}P_0(6)$	487569.72	0.20	487578.80	0.20
${}^{R}P_0(5)$	492901.44	0.20	492911.52	0.30
${}^{R}P_0(4)$	498320.66	0.01	498331.70	0.37
${}^{R}P_0(3)$	503827.28	-0.62	503838.80	-0.30
${}^{R}P_0(2)$	509422.60	-0.30	509433.28	-1.15
${}^{R}Q_0(1)$	520995.72	0.09	521007.00	-0.23
${}^{R}Q_0(2)$	521237.52	0.00	521248.72	-0.21
${}^{R}Q_0(3)$	521599.44	-0.03	521610.40	-0.21
${}^{R}Q_0(4)$	522080.68	0.24	522091.48	0.26
${}^{R}Q_0(5)$	522679.18	0.15	522689.58	0.22
${}^{R}Q_0(6)$	523393.56	0.08	523403.48	0.18
${}^{R}Q_0(7)$	524221.70	0.02	524230.98	0.04
${}^{R}Q_0(8)$	525160.92	-0.28	525169.52	-0.32
${}^{R}R_0(0)$	529971.00	0.04	529977.00	0.04
${}^{R}R_0(1)$	532669.72	0.02	532681.52	0.59
${}^{R}R_0(2)$	538693.36	0.13	538704.68	0.65
${}^{R}R_0(3)$	544798.75	0.05	544809.01	0.09
${}^{R}R_0(4)$	550984.32	0.04	550993.60	-0.17
${}^{R}R_0(6)$	563587.20	-0.15	563594.18	-0.57
${}^{R}R_0(7)$	569999.99	-0.04	570005.78	-0.19
${}^{R}R_0(8)$	576483.20	-0.03	576487.70	0.38
${}^{R}R_0(9)$	583034.06	0.07		

Table 3.5: FIR rotational-tunneling transitions of $N_2 \cdots D_2O$. "O–C" are the observed frequencies minus the frequencies calculated with the fit parameters. All units are in MHz. Transitions are labeled with the notation ${}^{\Delta K}\Delta J_{K''}(J'')$.

	A_1		A_2		B_1		B_2	
Assignment	Observed	O–C	Observed	O–C	Observed	O–C	Observed	O–C
${}^{R}P_0(3)$	325231.4	0.4	325220.9	0.1				
${}^{R}P_0(2)$	330762.9	-0.8	330752.8	-0.4				
${}^{R}Q_0(1)$	341905.7	0.0	341895.1	0.2				
${}^{R}Q_0(2)$	342001.3	0.3	341990.8	0.5				
${}^{R}Q_0(3)$	342144.0	0.4	342133.7	0.5	332302.6	-0.1	332304.8	0.0
${}^{R}Q_0(4)$	342333.1	0.1	342322.8	0.0				
${}^{R}Q_0(5)$	342568.7	0.3	342558.8	0.2	332709.2	0.2	332710.9	0.0
${}^{R}Q_0(6)$	342849.3	0.1	342839.9	0.0	332977.6	0.0	332979.3	0.1
${}^{R}Q_0(7)$	343174.2	-0.2	343165.6	0.1	333288.4	0.0	333290.1	0.0
${}^{R}Q_0(8)$	343542.8	0.0	343534.5	0.0	333640.6	-0.1	333642.1	-0.1
${}^{R}Q_0(9)$	343953.1	-0.1	343945.4	-0.1	334033.0	-0.1	334034.5	0.0
${}^{R}Q_0(10)$	344403.8	-0.2	344396.8	-0.2	334464.1	0.1	334465.5	0.0
${}^{R}Q_0(11)$	344893.6	-0.1	344887.2	-0.2				
${}^{R}Q_0(12)$	345420.9	0.2	345415.3	0.3				
${}^{R}R_0(0)$	347418.5	-0.1	347406.9	-0.6				
${}^{R}R_0(1)$	352987.0	-0.2	352975.7	-0.4				
${}^{R}R_0(2)$	358562.6	-0.2	358551.9	-0.1				
${}^{R}R_0(3)$	364144.4	0.0	364134.3	0.2	354365.5	0.1	354367.4	0.1
${}^{R}R_0(4)$	369730.9	0.2	369721.3	0.3	359979.7	-0.1	359981.5	-0.1
${}^{R}R_0(5)$	375320.6	0.1	375311.8	0.0	365604.0	0.0	365605.7	0.0
${}^{R}R_0(6)$	380912.2	-0.2	380904.3	-0.3	371236.6	0.1	371238.4	0.1
${}^{R}R_0(7)$	386505.1	0.1	386497.9	0.1	376876.3	0.1	376878.1	0.1
${}^{R}R_0(8)$					382521.6	-0.1	382523.4	-0.1
${}^{R}R_0(9)$					388171.7	0.0	388173.4	0.0

Table 3.6: MW and FIR rotational-tunneling transitions of $OC\cdots H_2O$. "O–C" are the observed frequencies minus the frequencies calculated with the fit parameters. All units are in MHz. Transitions are labeled with the notation ${}^{\Delta K}\Delta J_{K''}(J'')$, and frequencies marked with an asterisk are from Yaron *et al.*

	A		B	
Assignment	Observed	O–C	Observed	O–C
${}^{Q}R_0(0)$	5498.17*	0.00	5500.93*	0.00
${}^{Q}R_0(1)$	10995.86*	-0.00	11001.38*	0.00
${}^{Q}R_0(2)$	16492.55*	-0.01	16500.84*	0.00
${}^{Q}R_0(3)$	21987.77	0.19	21999.00	0.17
${}^{Q}R_0(4)$	27481.03	0.18	27495.02	0.16
${}^{Q}R_0(5)$	32971.82	0.13	32988.54	0.11
${}^{Q}R_0(6)$	38459.65	0.07	38479.12	0.06
${}^{Q}R_0(7)$	43944.04	0.06	43966.35	0.08
${}^{Q}R_0(8)$	49424.50	0.07	49449.83	-0.02
${}^{Q}R_0(9)$	54900.52	0.06	54928.37	-0.04
${}^{Q}R_0(10)$	60371.63	0.00	60402.18	-0.19
${}^{Q}R_0(11)$	65837.31	0.06	65870.81	-0.12
${}^{Q}R_0(12)$	71297.10	0.09	71333.53	-0.08
${}^{Q}R_0(13)$			76789.69	-0.23
${}^{R}P_0(13)$	523382.07	0.03		
${}^{R}P_0(11)$	533491.02	-0.02	499757.36	-0.81
${}^{R}P_0(10)$	538602.58	0.12	504931.82	-0.47
${}^{R}P_0(9)$	543752.66	0.14	510139.88	0.64
${}^{R}P_0(8)$	548941.53	0.17	515379.32	0.10
${}^{R}P_0(7)$	554169.33	-0.33	520652.48	0.16
${}^{R}P_0(6)$	559436.17	-0.17	525958.64	0.09
${}^{R}P_0(5)$	564742.03	0.07	531297.92	0.08
${}^{R}P_0(4)$	570086.85	0.05	536670.14	0.09
${}^{R}P_0(3)$	575470.46	-0.06	542074.91	-0.04
${}^{R}P_0(2)$			547512.08	-0.16
${}^{R}Q_0(1)$	591914.58	-0.28	558532.78	0.23
${}^{R}Q_0(2)$	592041.32	-0.22	558632.58	0.06
${}^{R}Q_0(3)$	592231.16	-0.16	558781.98	-0.21
${}^{R}Q_0(4)$	592483.78	-0.08	558980.98	-0.21
${}^{R}Q_0(5)$	592798.75	0.05	559229.48	0.42
${}^{R}Q_0(6)$	593175.54	0.06	559525.44	0.22
${}^{R}Q_0(7)$	593613.50	0.10	559869.00	0.01
${}^{R}Q_0(8)$	594111.87	0.03	560259.52	-0.06
${}^{R}Q_0(9)$	594669.80	0.00	560695.94	-0.18
${}^{R}Q_0(10)$	595286.33	-0.03	561177.46	-0.18
${}^{R}Q_0(11)$	595960.37	-0.07	561703.14	0.04
${}^{R}Q_0(12)$	596690.75	0.05	562271.40	0.01

Table 3.7: FIR rotational-tunneling transitions of $OC\cdots H_2O$, continued

Assignment	A Observed	O–C	B Observed	O–C
$^RQ_0(13)$			562881.44	0.11
$^RQ_0(14)$			563531.78	0.07
$^RQ_0(15)$			564221.20	-0.08
$^RR_0(0)$	597386.64	-0.04	564014.54	-0.01
$^RR_0(1)$	602958.87	0.13	569576.90	-0.26
$^RR_0(2)$	608567.18	0.82	575169.71	-0.01
$^RR_0(3)$	614210.83	0.17	580791.56	0.04
$^RR_0(4)$	619889.01	-0.01	586441.85	0.18
$^RR_0(5)$	625600.00	-0.80	592119.63	-0.18
$^RR_0(6)$	631345.80	0.58	597824.20	-0.35
$^RR_0(7)$	637121.20	-0.01	603554.43	-0.62
$^RR_0(8)$	642927.50	-0.10	609311.10	0.86
$^RR_0(9)$	648763.17	-0.17	615089.38	0.44
$^RR_0(10)$	654626.60	-0.10	620889.98	0.11
$^RR_0(11)$	660516.56	0.08		

3.3.2 Hamiltonian and data fitting

The nearly linear arrangement of the heavy atoms in the $N_2\cdots H_2O$ and $OC\cdots H_2O$ complexes gives them a near-prolate character. For example, the asymmetry parameter

$$\kappa = \frac{2B - A - C}{A - C} \tag{3.1}$$

is -0.99992 for $OC\cdots H_2O$ (κ = -1 signifies a completely prolate top). Even at the relatively high resolution of 1 part in 10^6 for the FIR spectrometer, the splitting of the $K_P = 1$ symmetric top states will be unresolved, so it is appropriate to label the observed spectra with prolate top quanta and assume K_P is a good quantum number. Even so, because of the wide amplitude motions and anisotropic IPS expected for these complexes, one needs to use an asymmetric top Hamiltonian in order to properly account for the rotational distortion. The form of the Hamiltonian used is the A-reduced Watson Hamiltonian in the I_r basis set [6], which has the basic form

$$\hat{H} = \frac{1}{2}(B + C)J(J + 1) + [A_{eff} - \frac{1}{2}(B + C)]K^2$$

Table 3.8: FIR rotational-tunneling transitions of $^{13}OC\cdots H_2O$. "O–C" are the observed frequencies minus the frequencies calculated with the fit parameters. All units are in MHz. Transitions are labeled with the notation ${}^{\Delta K}\Delta J_{K''}(J'')$, and frequencies marked with an asterisk are from Yaron *et al.*

	A		B	
Assignment	Observed	O–C	Observed	O–C
${}^{Q}R_0(0)$	5471.31*	0.01	5474.07*	0.01
${}^{Q}R_0(1)$	10942.12*	0.00	10947.62*	0.00
${}^{Q}R_0(2)$			16420.21*	0.00
${}^{R}P_0(7)$	547728.32	0.04		0.00
${}^{R}P_0(5)$			525783.98	0.01
${}^{R}P_0(4)$			531126.62	0.00
${}^{R}P_0(3)$	568913.30	-0.31	536502.58	-0.02
${}^{R}P_0(2)$	574308.84	1.00	541912.01	0.36
${}^{R}Q_0(1)$	585275.98	-0.17	552878.52	-0.02
${}^{R}Q_0(2)$	585403.96	-0.20	552980.56	-0.01
${}^{R}Q_0(3)$	585596.02	0.10	553133.32	-0.01
${}^{R}Q_0(4)$	585851.38	0.22	553336.53	0.03
${}^{R}Q_0(5)$	586169.66	0.18	553589.59	-0.04
${}^{R}Q_0(6)$	586550.48	0.09	553892.18	0.03
${}^{R}Q_0(7)$	586993.08	-0.24	554243.40	-0.01
${}^{R}R_0(0)$	590721.00	-0.27		
${}^{R}R_0(1)$	596268.04	0.32	563870.28	-0.16
${}^{R}R_0(2)$	601849.84	-0.94	569437.92	-0.24
${}^{R}R_0(3)$	607469.76	0.09	575035.68	-0.12
${}^{R}R_0(4)$	613123.28	-0.25		
${}^{R}R_0(5)$	618811.72	0.33	586318.06	0.39
${}^{R}R_0(6)$			591999.96	-0.19

Table 3.9: FIR rotational-tunneling transitions of OC···DOH. "O–C" are the observed frequencies minus the frequencies calculated with the fit parameters. All units are in MHz. Transitions are labeled with the notation ${}^{\Delta K}\Delta J_{K''}(J'')$, and frequencies marked with an asterisk are from Yaron *et al.*

Assignment	Observed	O–C
${}^{Q}R_0(0)$	5454.68*	-0.02
${}^{Q}R_0(1)$	10908.95*	-0.01
${}^{Q}R_0(2)$	16362.35*	0.02
${}^{R}P_0(16)$	484803.80	0.57
${}^{R}P_0(15)$	489835.46	-0.29
${}^{R}P_0(14)$	494895.20	-0.60
${}^{R}P_0(13)$	499983.20	-0.53
${}^{R}P_0(12)$	505100.00	0.18
${}^{R}P_0(11)$	510244.58	0.26
${}^{R}P_0(10)$	515417.70	0.32
${}^{R}P_0(9)$	520619.36	0.26
${}^{R}P_0(8)$	525849.95	0.42
${}^{R}P_0(7)$	531109.25	0.60
${}^{R}P_0(5)$	541713.26	0.69
${}^{R}P_0(4)$	547057.82	0.76
${}^{R}Q_0(1)$	568759.22	-0.63
${}^{R}Q_0(2)$	568855.38	0.45
${}^{R}Q_0(3)$	568996.65	-0.71
${}^{R}Q_0(4)$	569187.29	0.37
${}^{R}Q_0(5)$	569423.35	0.02
${}^{R}Q_0(6)$	569706.68	0.47
${}^{R}Q_0(7)$	570035.33	0.21
${}^{R}Q_0(8)$	570409.64	0.09
${}^{R}Q_0(9)$	570828.82	-0.10
${}^{R}Q_0(10)$	571292.43	-0.12
${}^{R}Q_0(11)$	571799.64	-0.08
${}^{R}Q_0(12)$	572349.50	-0.11
${}^{R}Q_0(13)$	572941.18	-0.17
${}^{R}Q_0(14)$	573573.98	0.00
${}^{R}Q_0(15)$	574246.63	0.17
${}^{R}R_0(0)$	574193.10	-0.44
${}^{R}R_0(1)$	579700.47	-0.42
${}^{R}R_0(2)$	585233.62	-0.15
${}^{R}R_0(3)$	590791.08	-0.53
${}^{R}R_0(4)$	596373.84	0.05
${}^{R}R_0(5)$	601979.38	-0.26
${}^{R}R_0(6)$	607608.02	-0.43
${}^{R}R_0(7)$	613259.02	-0.47
${}^{R}R_0(8)$	618931.32	-0.65
${}^{R}R_0(9)$	624625.88	0.81
${}^{R}R_0(10)$	630337.92	-0.02

Table 3.10: FIR rotational-tunneling transitions of $OC\cdots D_2O$. "O–C" are the observed frequencies minus the frequencies calculated with the fit parameters. All units are in MHz. Transitions are labeled with the notation ${}^{\Delta K}\Delta J_{K''}(J'')$, and frequencies marked with an asterisk are from Yaron *et al.*

	A		B	
Assignment	Observed	O–C	Observed	O–C
${}^{Q}R_0(0)$	5238.38*	0.00	5237.81*	0.04
${}^{Q}R_0(1)$	10476.32*	0.00	10475.18*	-0.03
${}^{Q}R_0(2)$	15713.57*	0.00	15711.95*	0.01
${}^{R}Q_0(1)$	350668.96	0.47	348643.24	0.06
${}^{R}Q_0(2)$	350707.64	0.49	348682.40	0.10
${}^{R}Q_0(3)$	350765.48	0.41	348741.04	0.12
${}^{R}Q_0(4)$	350842.60	0.42	348819.00	0.05
${}^{R}Q_0(5)$	350935.68	0.31	348916.32	0.03
${}^{R}Q_0(6)$	351053.88	0.35	349032.76	-0.05
${}^{R}Q_0(7)$	351187.68	0.20	349168.48	0.11
${}^{R}Q_0(8)$	351340.04	-0.03	349322.64	-0.13
${}^{R}Q_0(9)$	351511.20	0.12	349495.68	-0.13
${}^{R}Q_0(10)$	351700.28	-0.01	349687.36	0.11
${}^{R}Q_0(11)$	351907.00	-0.44		
${}^{R}Q_0(12)$	352131.92	-0.35		
${}^{R}Q_0(13)$	352374.28	-0.18		
${}^{R}Q_0(14)$	352633.80	0.10		
${}^{R}Q_0(15)$	352909.88	0.26		
${}^{R}R_0(0)$	355880.88	-0.17	353855.80	-0.09
${}^{R}R_0(1)$	361104.84	-0.91	359082.24	-0.05
${}^{R}R_0(2)$	366321.04	-1.33	364302.24	-0.18
${}^{R}R_0(3)$	371528.72	-1.37	369515.84	-0.02
${}^{R}R_0(4)$	376727.92	-0.39	374722.16	-0.03
${}^{R}R_0(5)$	381918.02	1.22	379920.84	-0.12
${}^{R}R_0(6)$	387098.40	2.53	385112.00	0.27
${}^{R}R_0(7)$	392267.10	0.50	390294.00	-0.04
${}^{R}R_0(8)$	397427.06	-3.87	395467.44	0.00
${}^{R}R_0(9)$	402593.52	1.63	400631.46	-0.03

Table 3.11: Fitted spectroscopic parameters for $N_2 \cdots H_2O$.

	A_1	A_2	B_1	B_2
A_{eff}(MHz)	542864.42(10)	541494.39(10)	479116.584(37)	479364.006(32)
B(MHz)	2936.621(17)	2929.998(16)	2928.5732(29)	2929.3295(25)
C(MHz)	2877.230(17)	2882.726(16)	2899.7177(28)	2899.1733(24)
Δ_J(kHz)	43.371(26)	41.708(25)	42.563(34)	42.889(30)
Δ_{JK}(MHz)	-85.605(11)	-96.012(13)	-60.7250(26)	-59.0216(23)
δ_J(kHz)	10.53(23)	-1.07(22)	4.567(23)	5.917(20)
H_J(Hz)	4.88(37)	2.25(33)	2.93(28)	3.47(25)
H_{JK}(kHz)	-14.78(24)	-44.06(27)	-28.741(41)	-23.761(35)
L_{JJK}(HZ)	(0)	(0)	13.81(15)	9.32(13)

$$- \Delta_J J^2(J+1)^2 - \Delta_{JK} J(J+1)K^2 - \Delta_K K^4$$
$$+ \text{off diagonal terms}$$
$$+ \text{higher order terms.} \qquad (3.2)$$

Tunneling splittings are not explicitly treated with this Hamiltonian, and are incorportated in the fit into the A_{eff} rotational constant; Δ_K is also included in A_{eff} since there is high degree of correlation between these two terms for a data set with only two values of K. The program `AFITSPEC` developed by Dr. Roger Bumgarner was used to fit the data, and the results are given in Tables 3.11–3.17. The MW data of Leung al. and Yaron *et al.*, as well as those reported here, were incorportated into the fits. Note that the different distortional constants vary between complexes, from isotopomer to isotopomer, and from symmetry state to symmetry state. The number and kind of distortion parameters were chosen to bring the fits within experimental error, ± 0.5 MHz, and were added sequentially and rationally, starting with lower order parameters.

3.3.3 Structural analysis

The above spectral analysis provides a full set of rotational constants for a number of isotopomers to which the ground state structures of the nitrogen-water and carbon monoxide-water complexes can be fit. A caveat is in order, however. As noted in the

Table 3.12: Fitted spectroscopic parameters for $N_2 \cdots$ DOH.

	A_1	A_2
A_{eff}(MHz)	523759.193(81)	523770.88(10)
B(MHz)	2902.268(15)	2902.291(12)
C(MHz)	2867.085(13)	2867.052(15)
Δ_J(kHz)	35.41(20)	34.835(90)
Δ_{JK}(MHz)	-51.7926(34)	-51.7314(44)
δ_J(kHz)	2.163(21)	2.072(28)
H_J(Hz)	4.14(89)	
H_{JK}(kHz)	-12.489(27)	-12.512(35)

Table 3.13: Fitted spectroscopic parameters for $N_2 \cdots D_2O$.

	A_1	A_2	B_1	B_2
A_{eff}(MHz)	344633.96(16)	344622.94(16)	334803.79(27)	334806.08(22)
B(MHz)	2795.473(45)	2795.348(46)	2789.41(40)	2789.47(32)
C(MHz)	2756.501(51)	2756.373(27)	2758.98(11)	2758.965(92)
Δ_J(kHz)	26.7(22)	23.00(69)	30.3(38)	28.7(31)
Δ_{JK}(MHz)	-14.139(16)	-14.177(13)	-15.233(71)	-15.199(57)
H_J(Hz)	22.(14)		32.0(76)	26.7(61)
H_{JK}(kHz)	-6.830(41)	-6.798(41)	-6.513(52)	-6.432(41)

Table 3.14: Fitted spectroscopic parameters for $OC \cdots H_2O$.

	A	B
A_{eff}(MHz)	594600.280(89)	561233.01(11)
B(MHz)	2762.1849(39)	2759.9769(73)
C(MHz)	2736.0710(39)	2741.0376(73)
Δ_J(kHz)	20.474(12)	20.416(15)
Δ_{JK}(MHz)	-25.1925(31)	-20.2986(43)
δ_J(kHz)	0.520(15)	1.154(54)
H_{JK}(kHz)	-3.980(20)	-3.838(32)
h_J(Hz)		1.26(21)

Table 3.15: Fitted spectroscopic parameters for $O^{13}C\cdots H_2O$.

	A	B
A_{eff}(MHz)	587947.79(25)	555564.53(12)
B(MHz)	2748.785(11)	2746.704(12)
C(MHz)	2722.597(11)	2727.433(12)
Δ_J(kHz)	20.04(30)	20.37(12)
Δ_{JK}(MHz)	-25.487(27)	-20.727(11)
δ_J(kHz)		0.85(13)
H_{JK}(kHz)	-4.07(52)	-3.81(19)

Table 3.16: Fitted spectroscopic parameters for OC$\cdots$DOH.

A_{eff}(MHz)	571439.66(18)
B(MHz)	2737.8942(80)
C(MHz)	2716.8813(63)
Δ_J(kHz)	18.48(11)
Δ_{JK}(MHz)	-18.5404(53)
H_J(Hz)	1.89(57)
H_{JK}(kHz)	-2.526(34)
h_{JK}(kHz)	-0.551(29)

Table 3.17: Fitted spectroscopic parameters for OC$\cdots D_2O$.

	A	B
A_{eff}(MHz)	353268.37(58)	351242.53(19)
B(MHz)	2632.111(79)	2631.4543(80)
C(MHz)	2606.343(84)	2606.380(11)
Δ_J(kHz)	19.9(11)	14.46(32)
Δ_{JK}(MHz)	-3.231(46)	-3.519(10)
H_J(Hz)	238(39)	5.0(24)
H_{JK}(kHz)	-6.9(12)	-1.12(11)
h_{JK}(kHz)	5.8(12)	

first chapter, while these complexes can be expected to have a much more defined structure than Ar$\cdots$H$_2$O, and while the quenching of the water tunneling is evidence of this, these are still weak and anharmonic bonds, as depicted in Figure 1.2, and any structure derived will still represent a statistical average over the portion of the IPS accessible at ground state energies. Nevertheless, an averaged but accurate molecular structure can give us a more tangible feeling for the chemical interactions in the complex in the absence of a multidimensional IPS, and can serve as a benchmark for non-empirical computational efforts.

In this analysis, it will be assumed that the monomer units—N_2, CO, and H_2O—all retain their $\langle R_0 \rangle$ monomer geometries within the complexes [23]. In order to arrive at the correct structure from the rotational constants, efforts must be made to ensure that they represent the structural inverses of the complexes' moments of inertia. In particular for these complexes, this means removing the effects of tunneling from the rotational constants. Since the structural and tunneling analyses here are interdependent and concurrent processes, the pertinent tunneling results will be stated in this section and justified below. The tunneling-free rotational contants are the averaged constants across all symmetry states for a given isotopomer. The A rotational constants for the nitrogen-water complexes were excluded because the tunneling effects could not be sufficiently decoupled. The program `STRFTQ` written by D. Schwendeman and modified by F. Lovas was used to fit the structures to the rotational constants [22], and the coordinates used in specifying the internal molecular coordinates are those developed by H. Thompson [21]. This program allows the simultaneous fitting of multiply substituted isotopomers by a weighted non-linear least squares routine, and is much more flexible and robust than using Kraitchman's equations in a repetitive, sequential algorithm.

The structure of OC$\cdots$H$_2$O was determined using the rotational constants from all four isotopomers studied in this work. The initial starting configuration was planar and any attempt at non-planar variations, *i.e.*, non-zero values of the ϕ coordinates, worsened the fit, and so the final fit included only the three planar variables R_{cm}, θ_{CO}, and θ_{H_2O}. The results are tabulated in Table 3.18. The monomer separation distance

Table 3.18: Optimized structural parameters for nitrogen-water and carbon monoxide-water dimers.

Parameter	$N_2\cdots H_2O$	$OC\cdots H_2O$
$R_{N\cdots H}/R_{C\cdots H}$	2.43 Å	2.41 Å
θ_{H_2O}	55.7°	57.4°
θ_{N_2}/θ_{CO}	21.9°	8.1°
$\phi_{H_2O} \equiv 0,\ \phi_{N_2} \equiv 0,\ \phi_{CO} \equiv 0$		

of $R_{C\cdots H} = 2.41 \pm 0.01$ Å is quite similar to the result of Yaron *et al.*, but the determined angular coordinates are somewhat different. Here, much of the non-linearity of the O—C$\cdots$H—O set of atoms stems from the tilt in the θ_{CO}= 8.1° parameter, while the water tilt angle of θ_{H_2O}= 57.4°makes the H—O bond parallel within error to the a-axis of the complex. Recall that in the MW experiment, no independent constraints could be placed upon θ_{CO}, and θ_{CO} and θ_{H_2O} were fit separately. The present structure confirms intuitive electrostatic sense, aligning both dipole-dipole and dipole-quadrupole interactions favorably. The structure of $OC\cdots H_2O$, as test for the $N_2\cdots H_2O$ structure, was fit without the A rotational constants, with no significant effect on the outcome. These results also agree well with the *ab initio* IPS discussed below.

The structure of $N_2\cdots H_2O$ was determined using only the B and C rotational constants of the three isotopomers studied in this work, and it also showed a strong preference for a planar structure. The results are tabulated in Table 3.18. Again, as with $OC\cdots H_2O$, the radial coordinate $R_{N\cdots H} = 2.43 \pm 0.02$ Å agrees well with the MW structure, as does θ_{N_2}= 21.9 $\pm$ 3.5 °, but the nearly linear θ_{H_2O} coordinate differs significantly from the 12° tilt of Leung *et al.* As before, the advantage of the present structural analysis over previous attempts is the ability to fit all parameters at the same time, from the same data. Also, the reliance on the nuclear quadrupole coupling constants in complexes with wide amplitude motions to provide accurate structural information is disputable, and is discussed further in the next chapter. The primary difference between the structures fit for $OC\cdots H_2O$ and $N_2\cdots H_2O$ is the much larger tilt of N_2 subunit compared to that for the CO subunit, which can be

ascribed to two factors: N_2 tunneling wavefunctions, discussed below, and the lack of a permanent dipole-dipole interaction. Although we saw above that the dipole-quadrupole term was much larger for $OC\cdots H_2O$ than the dipole-dipole term, and thus the lack of this latter term should make little difference for $N_2\cdots H_2O$, there is a much stronger directionality associated with dipole alignment than with the quadrupolar distribution of charges.

3.3.4 Water tunneling in $OC\cdots H_2O$

As stated in Section 3.3.2, the tunneling of water in the $OC\cdots H_2O$ complex was not treated explicitly in the Hamiltonian and spectral analysis, and the tunneling splitting of the rotational levels is accomodated by fitting each symmetry state for each isotopomer separately. The results of this treatment can be seen in the differences in rotational constants between symmetry states, as the A, B, and C rotational constants are all affected by the water tunneling. However, the A rotational constant stores by far the greatest amount of tunneling information: for the $OC\cdots H_2O$ isotopomer, the difference between the A and B symmetry states for A_{eff} is 3.0% but only 0.1% for B and C. The disparity is even greater for $OC\cdots D_2O$. In this treatment of the water tunneling potential, therefore, the assumption is made that total tunneling splitting of the rovibrational ground state is well approximated by the difference in A rotational constants. Δ_K is also included within A_{eff}, but for complexes like $H_3N\cdots H_2O$ studied in the next chapter, when Δ_K is decoupled, its value is less than 1% of the present tunneling splitting.

There are two possible monomer-fixed axes about which the water subunit can exchange its hydrogens—its b- and c-axes—and it is important to determine by which of these pathways the exchange occurs for two different reasons. First, in modeling the tunneling motion, it is necessary to know the reduced mass of the tunneling motion, and because water is a very asymmetric molecule, its moments of inertia are quite dissimilar. In addition, the selection rules between the two tunneling states in $K = 0$ and $K = 1$ can either be "top-to-top, bottom- to-bottom" or "top-to-bottom,

bottom-to-top," and knowing which selection rules apply will tell whether ΔA_{eff} is either the difference or the sum of the $K = 0$ and $K = 1$ splittings respectively (see Figure 3.6). However, because the symmetry labels have already been unambiguously applied to the ground rotational states by Yaron *et al.*, we know that the higher frequency transition originates from the totally symmetric A ground state, and therefore the selection rules must be "top-to-bottom, bottom-to-top," and the tunneling levels are shown in Figure 3.6 for $OC\cdots H_2O$ and $OC\cdots D_2O$. How then to determine the tunneling pathway? Recall from $Ar\cdots H_2O$ and Equation (1.4) that the exchange wavefunction was dependent upon the overall rotation of the complex. In $OC\cdots H_2O$, tunneling about the c-axis of H_2O has a barrier which aligns the b-symmetry axis of H_2O with the a-axis of the complex, and the symmetry of rotation about the a-axis of a prolate top is symmetric for K even and antisymmetric for K odd. Again, we have ortho and para nuclear spin states associated with the H_2O subunit, and in order to maintain $\psi_{exchange}$ overall as antisymmetric, ortho and para wavefunctions must alternate pairing with K. The tunneling about the H_2O b-axis has no such symmetry dependence, and so the tunneling must occur about the c-axis of water, as the symmetry labels in Figure 3.6 indicate. If we assume that the tunneling splitting in the $K = 0$ and $K = 1$ rotational levels are similar, which is reasonable since the energy difference in these two levels (~ 20 cm^{-1}) is small compared to the potential well depth, then the tunneling splitting ν_t is 16.684 GHz for $OC\cdots H_2O$ and 1.012 GHz for $OC\cdots D_2O$. These values are in excellent agreement with the calculations of Yaron *et al.*

A Fourier expansion in $\cos(\theta_{H_2O})$ is used to model the one-dimensional potential,

$$V(\theta_w) = \sum_n (\frac{1}{2} V_n)[1 - \cos(n\theta_{H_2O})], \tag{3.3}$$

and the energy levels are calculated using an internal rotor Hamiltonian

$$\hat{H} = -\frac{\hbar^2}{2I_{tunnel}} \left(\frac{d^2}{d\theta^2_{H_2O}} \right) + V(\theta_{H_2O}) \tag{3.4}$$

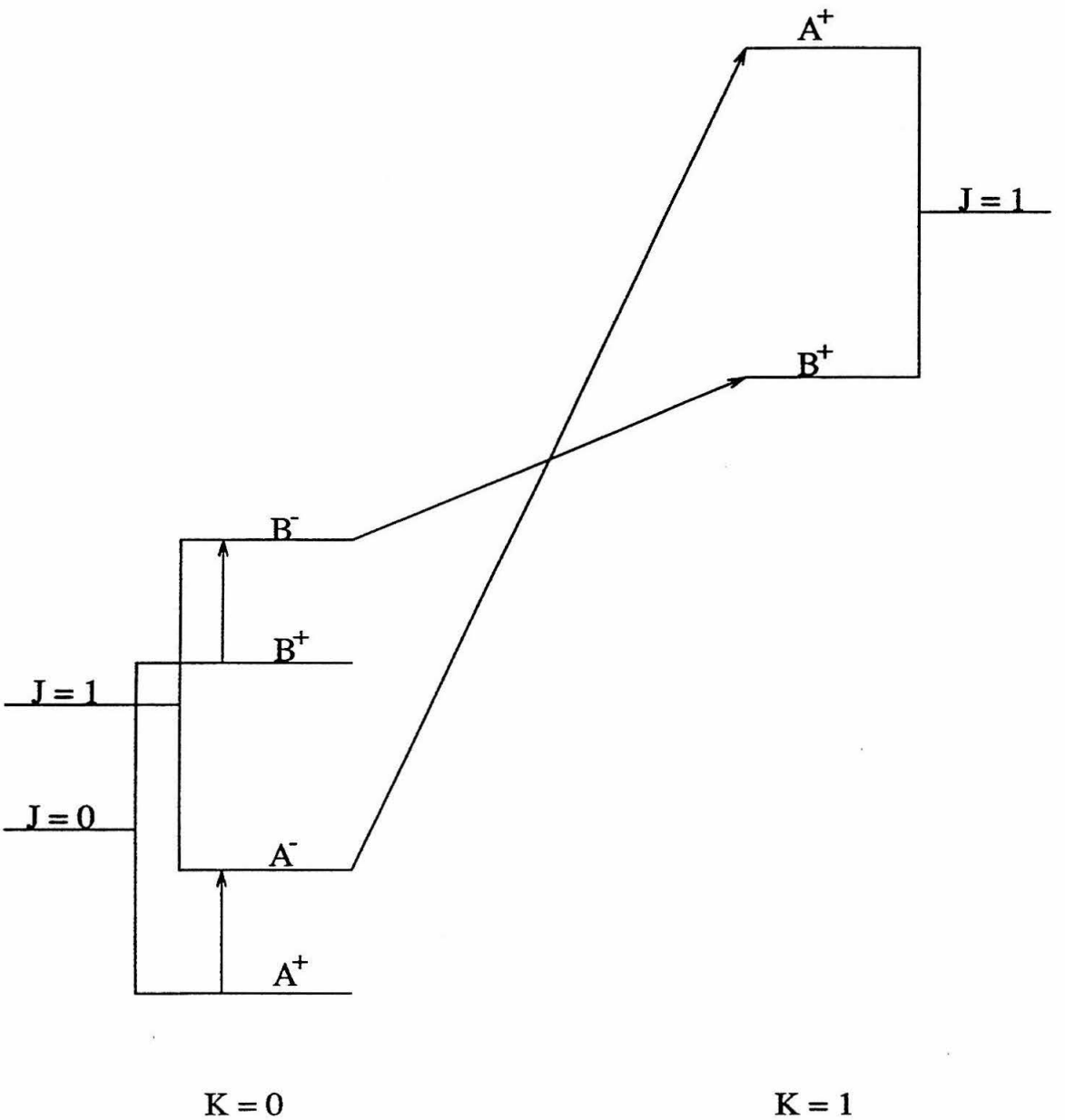

Figure 3.6: Selection rules for OC$\cdots$H$_2$O spectra.

with free rotor basis funtions

$$\psi = \frac{1}{\sqrt{2\pi}} e^{im\theta_{H_2O}}. \tag{3.5}$$

The c-inertial moments of H_2O and D_2O are used for I_{tunnel}. A two term $V_1 + V_2$ potential was used to fit the OC$\cdots$$H_2O$ and OC$\cdots$$D_2O$ splittings. Note that in this potential, θ_{eq} is not independent and is determined by

$$-\frac{V_1}{4V_2} = \theta_{eq}. \tag{3.6}$$

The parameters found which reproduce the tunneling splittings of 16.7 GHz and 1.01 GHz are V_1=745.00 cm^{-1} and V_2=-493.21 cm^{-1}, which in turn determine θ_{eq}= 67.8°. This potential, shown with the first two tunneling levels in Figure 3.7, has a barrier height of 191 cm^{-1} and a 58 cm^{-1} worth of zero point energy, and the tunneling wavefunction has an amplitude under the barrier that is approximately 7% of the maximum amplitude. The value of θ_{eq} is 10° larger than that found in the structural analysis, and this may well be due to limited number of parameters in the potential. In order to explore the response of the potential to more degrees of freedom, a third potential term, V_3, was added to the Hamiltonian, and the height of the potential at θ_{H_2O}= 180° was varied along with θ_{eq}. Ranges of 400 to 1100 cm^{-1} and 58° to 67° reproduced the earlier barrier height within 12%. Thus, the inner walls of the potential seem to have been accurately determined by the Fourier expansion, which makes sense since this is the portion of the potential which is well-sampled by the tunneling of the water subunit.

3.3.5 Water and nitrogen tunneling in $N_2\cdots H_2O$

No attempts thus far to place the tunneling motions of H_2O and N_2 in the same context as above have been successful, and this difficulty arises from two factors. First, the lower binding energy of $N_2\cdots H_2O$ relative to OC$\cdots$$H_2O$, only 60%, and the homo- *vs.* heteronuclear acceptor mean that the nitrogen-water IPS is significantly more isotropic than that for OC$\cdots$$H_2O$. With a presumably lower tunneling barrier,

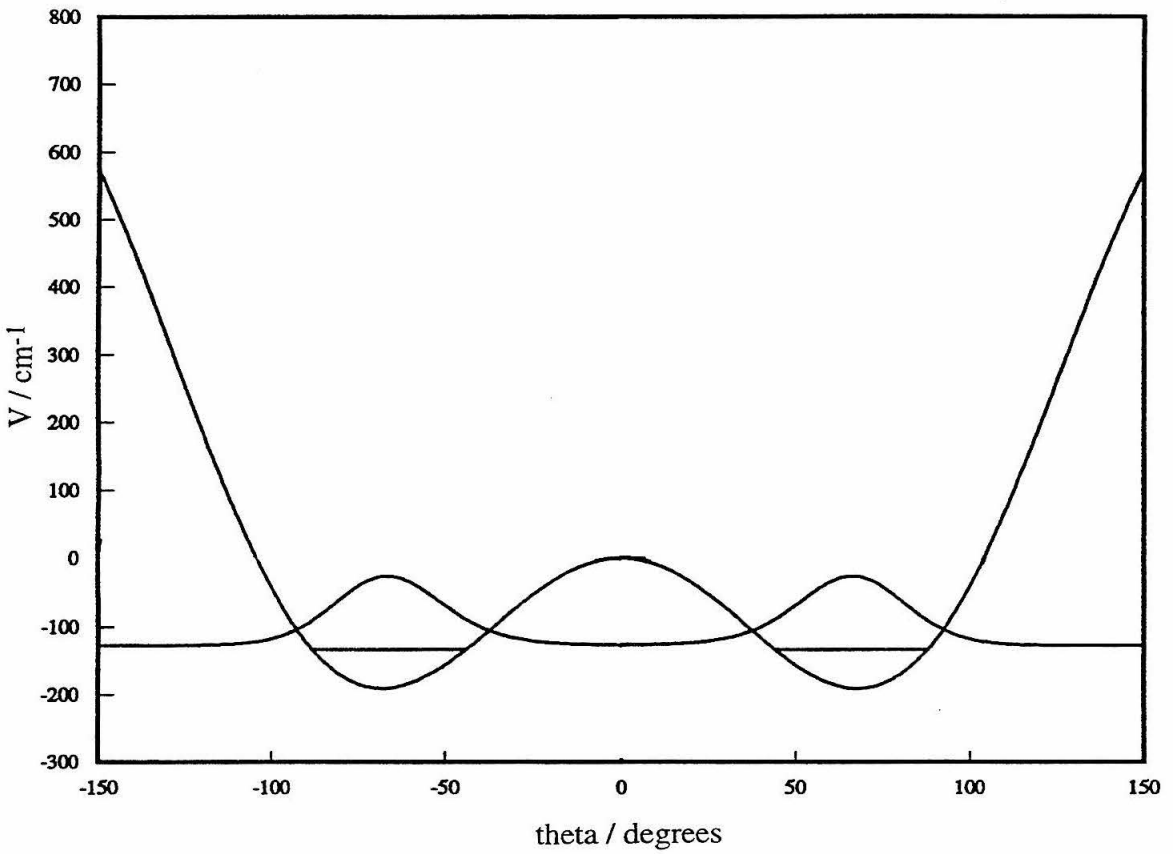

Figure 3.7: Tunneling potential and ground state energy and wavefunction for $OC\cdots H_2O$.

the tunneling splittings in $N_2\cdots H_2O$ might be affected by the rotational energy of the complex, and the assumptions used above may not apply here. Second, and more demonstrable, the tunneling motions of H_2O and N_2 are coupled to some degree. This effect was first seen in the MW data collected by Leung and coworkers. For example, the nitrogen tunneling splitting in the $J = 0 \rightarrow 1$ transition of $^{15}N_2\cdots H_2O$ is dependent upon the water tunneling state: it is 700 kHz for the singlet ($I_H = 0$) water tunneling state but less than 200 kHz for the triplet tunneling state. Also, the nuclear quadrupole coupling constant $eQq_a(^{14}N)$ is seen to vary by as much as 5% between water tunneling states.

As disscused in Section 3.1.3, there are three feasible pathways by which the hydrogen and nitrogen nuclei may tunnel, but only two of these together can form a unique set of operations. Since these two operations must effectively include the geared tunneling mechanism, both tunneling motions must be treated at the same time. The first step, as with $OC\cdots H_2O$, is to determine the specific pathways along which the hydrogen and nitrogen nuclei tunnel. Because the out-of-plane potential is much steeper than the in-plane potential, as revealed by the structural analysis, and by analogy to the similar $OC\cdots H_2O$ complex, it is reasonable to assume that both tunneling pathways are in the plane of the ground state structure. The barriers for both tunneling pathways must lie along the a-axis of the complex because of symmetry constraints, and so the pairing of the nuclear spin wavefunctions again alternates with the value K. Figure 3.8 shows the resulting double "top-to-bottom, bottom-to-top" selection rules for b-type $K = 0 \rightarrow 1$ transitions. Notice that H_2O, which has a pair of fermions, and N_2, bosons, pair oppositely with tunneling and rotation wavefunctions to make $\psi^{H_2O}_{exchange}$ antisymmetric and $\psi^{N_2}_{exchange}$ symmetric.

Also labeled in Figure 3.8 are the six different tunneling splittings associated with this rotation-tunneling manifold. In $OC\cdots H_2O$, there were only two which were assumed to be nearly equal; however, the FIR data for the nitrogen-water isotopomers show evidence for tunneling splittings of different values for both H_2O and N_2 tunneling. The A_{eff} rotational constants, which again accomodate most of the tunneling effects in the spectral analysis, have a marked interdependence between water and

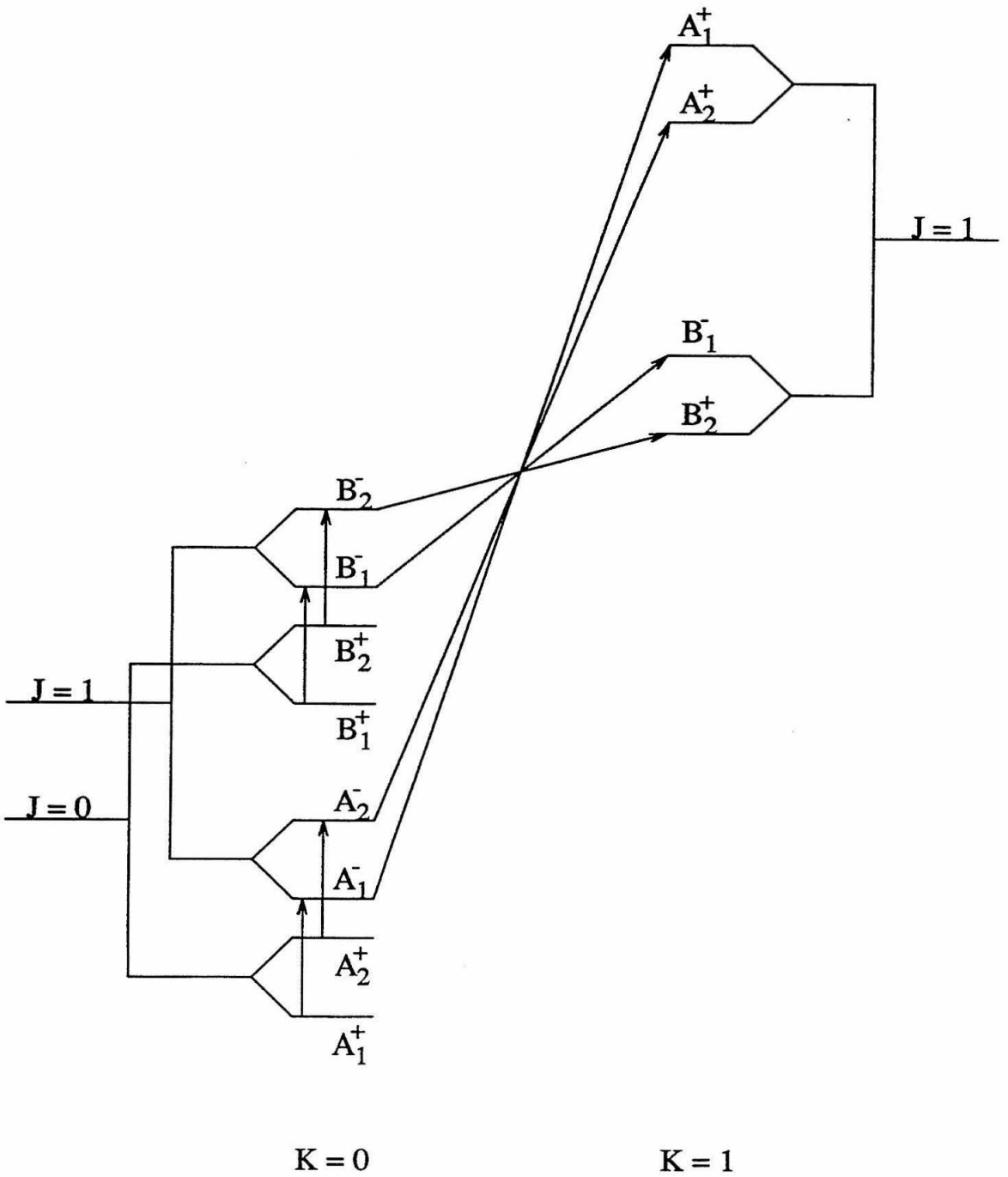

Figure 3.8: Selection rules for $N_2 \cdots H_2O$ spectra.

nitrogen tunneling. The nitrogen tunneling splitting in $N_2\cdots H_2O$ from the water tunneling ground state, $A(A_1)$-$A(A_2)$ = 1370 MHz, is 5.5 times the value for the equivalent splitting in the excited water tunneling state, $A(B_1)$-$A(B_2)$ = 284 MHz. The water tunneling splitting is also dependent upon the nitrogen tunneling state. One example of this is the comparison of the averaged values of A_{eff} across all symmetry states, $\bar{A}_{eff}$ for $N_2\cdots H_2O$ and $N_2\cdots$DOH. Here, $\bar{A}_{eff}$ for $N_2\cdots$DOH is *larger* by 13 GHz than that for $N_2\cdots H_2O$. Thus, it appears that there exist no near degeneracies in the six tunneling splittings for the $N_2\cdots H_2O$ rotation-tunneling manifold. With at most four values of A_{eff} per isotopomer, it is impossible to fit all six different, independent tunneling splittings: more rotational data with access to higher values of K are necessary in order to obtain a fit to all the tunneling splittings.

3.4 *Ab initio* and Diffusion Monte Carlo adjusted IPSs

3.4.1 *Ab initio* calculations and IPSs for planar complexes

The calculations described below were performed by Dr. Roger Bumgarner as an outgrowth of the efforts to extract parts of the IPSs for $N_2\cdots H_2O$ and $OC\cdots H_2O$ in the regions sampled by their FIR rotation-tunneling spectra. The Gaussian 88 suite of programs was used [17], employing a 6-31G** basis set, and second and fourth order Møller-Plesset corrections. The monomer geometeries were optimized separately and then frozen in the intermolecular calculations, where a grid of points across $\theta_{H_2O}\otimes\theta_{N_2}$ or $\theta_{H_2O}\otimes\theta_{CO}$ was scanned while optimizing R_{cm}. These represent initial efforts at characterizing the general features of the IPSs with less attention to the absolute energy relative to infinite separation. The results can be seen in Figure 3.9a and b for $N_2\cdots H_2O$ and $OC\cdots H_2O$. Because the primary motivation for generating these IPSs was to aid in the investigation of rotation-tunneling phenomena within the plane, the energies are shown relative to the water donor tunneling barrier height.

Due to symmetry, the $N_2\cdots H_2O$ IPS shown in Figure 3.9a is complete, with in-

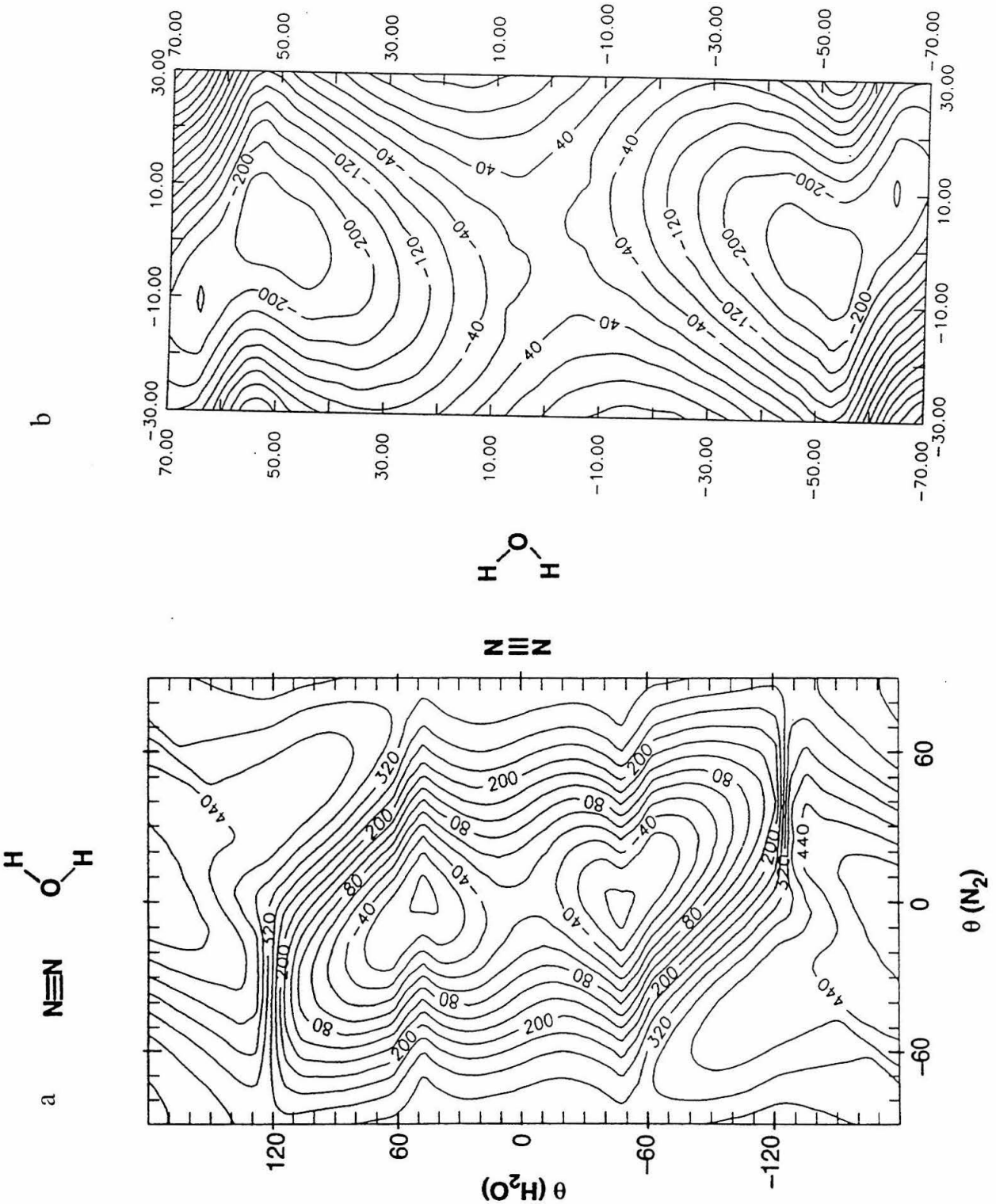

Figure 3.9: *Ab initio* IPSs calculated at the MP2 level of correction for a) $N_2 \cdots H_2O$, and b) $OC \cdots H_2O$. Energy units are in wavenumbers and are relative to the top of the water tunneling barrier.

teraction energies for all combinations of θ_{H_2O} and θ_{N_2}. There are two unique minima on the surface: the global minimum corresponding to the $N_2 \cdots H_2O$ bonding configuration at ($\pm 50°$,$\mp 5°$); and an O-bound minimum, which represents the interaction of the negative end of the H_2O dipole with the positive region of the N_2 quadrupole, found at the top right and bottom left corners of the surface ($\pm 180°$,$\mp 90°$). Also evident are the three accessible tunneling pathways: the donor tunneling, with a barrier of 120 cm^{-1}; acceptor tunneling, 440 cm^{-1}; and geared tunneling, 400 cm^{-1}. Notice that even the water donor tunneling mode involves a signicant $\pm 15°$ wag of the N_2 subunit, corroborating earlier evidence of the coupling of tunneling motions.

The IPS shown for $OC \cdots H_2O$ focuses more detail on the water tunneling region. The minima show a complex geometry similar to the one calculated in the structural analysis section, with a nearly linear extention of the O—H bond axis to the CO center of mass and a slight 5° tilt of the CO subunit. Again, donor tunneling involves some motion of the acceptor. Figure 3.10 is a comparison of the θ_{H_2O} potential surface fit to the tunneling splitting data in Section 3.3.4 to a cut along $\theta_{CO} = 0°$ from the present IPS. The barrier heights match well, although the postion of the minima differ by almost 10°. This may well stem from the exclusion of CO motion in the tunneling fit, and this problem is addressed in greater detail for the next complex studied, $H_3N \cdots H_2O$.

3.4.2 Diffusion Monte Carlo adjusted IPSs

Diffusion Monte Carlo (DMC) calculations, as implemented by Buch and Sandler for vdW clusters [18, 19], provide a flexible and robust intermediate between *ab initio* IPSs and experimental ground state data. The technique is based upon the correlation between the Schrödinger equation and the diffusion equation when substituting $t' = it$. An arbitrary ensemble of interaction geometries, or replicas, is chosen and allowed to propagate over a series of time intervals. Each replica is subject to multiplication or elimination, based upon its energy relative to the ensemble, and after a long enough time, the equilibium distribution of replicas approximates the ground

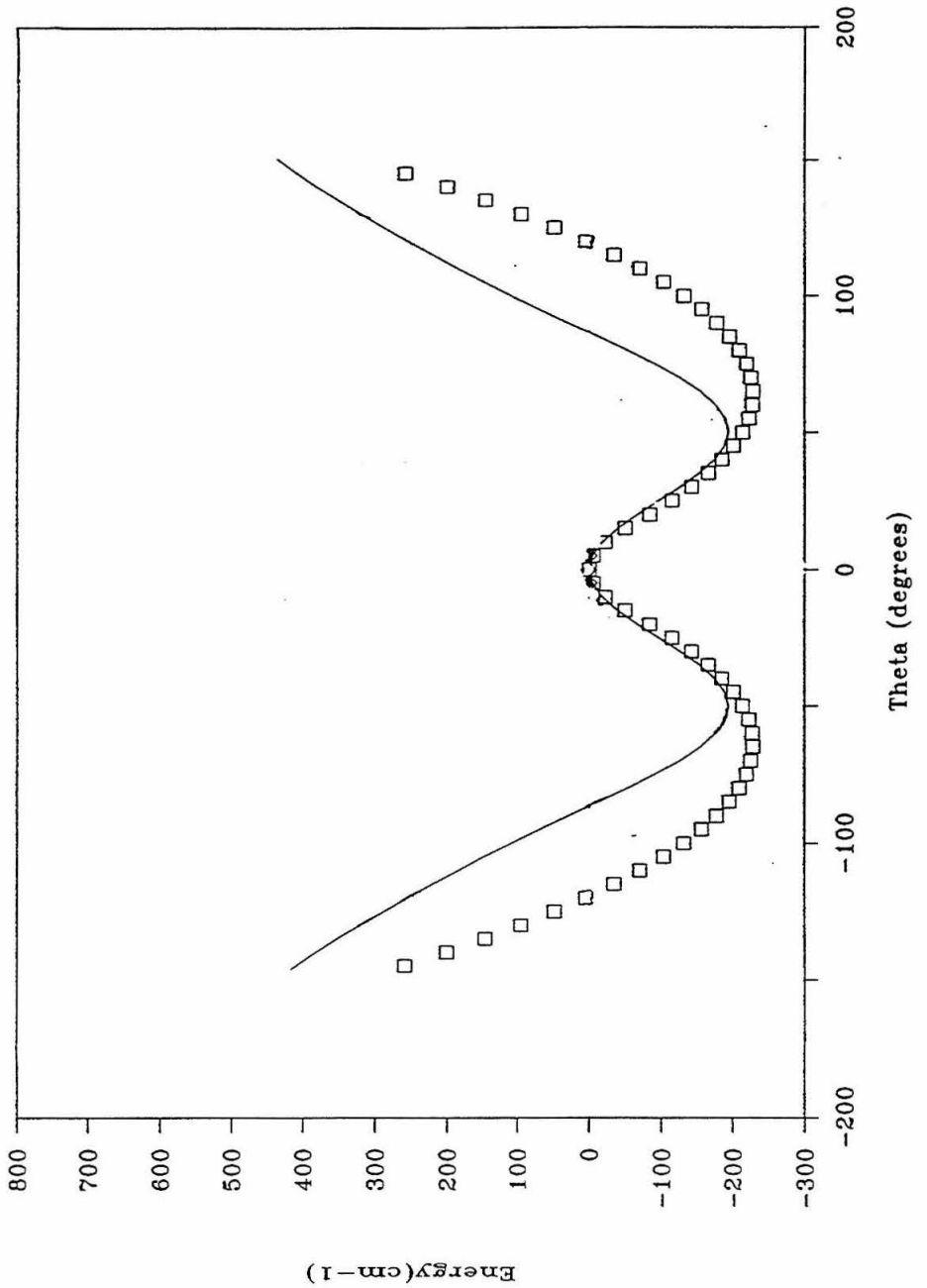

Figure 3.10: Comparison of Fourier $V_1 + V_2 + V_3$ and *ab initio* water tunneling IPS for $OC\cdots H_2O$. The line is a spline fit to the *ab initio* surface with θ_{CO} fixed to 0°, and the squares are along the Fourier potential.

state wavefunction. The basic method is as follows: 1), obtain an *ab initio* or other suitable surface; 2), parameterize the surface into a potential function; 3), use DMC to obtain the wavefunction and ground state eigenvalues; 4), test these against experimental results and adjust the potential parameters; and 5), repeat 3) and 4) until sufficient agreement is reached. While not as accurate as fitting a potential directly to the experimental observables, the authors claim an absolute accuracy of approximately 5%, with a much higher relative accuracy for different features on a particular surface. One major limitation of this method is that it is only easily applied to the ground state wavefunction and eigenvalues: excited states are much more difficult to reproduce using DMC.

Sandler and coworkers [19] and Sadlej and Buch [20] have applied this DMC methodology to the $N_2 \cdots H_2O$ and $OC \cdots H_2O$ complexes, and they have generated their own *ab initio* IPSs for the DMC calculations. These IPSs are presumably more accurate and reliable than the ones discussed above because these workers are experienced computationalists and they have performed energy partitioning and basis set expansion studies to optimize their work. The global minimum geometries found have a high degree of correlation with the results from the present structural analyses, and will not be discussed further. Interesting, however, are the absolute binding energies of the complexes calculated at different minima on the surfaces. For the $N_2 \cdots H_2O$ complex, the hydrogen-bonded global minimum was found to be bound by 430 cm^{-1}, while the oxygen-bound conformer had a binding energy of 275 cm^{-1}. Three different minima were found for the $OC \cdots H_2O$ complex: the hydrogen-bonded minimum at 651 cm^{-1}; a T-shaped oxygen-bonded geometry, with the water oxygen binding to the positive portion of the CO quadrupole, at 301 cm^{-1}; and an oxygen-bound configuration, with CO rotated by 180° from the global minimum structure, 256 cm^{-1}. Obviously, none of these non-global minima are populated in the planar supersonic expansion, which cools clusters to below 10 K. However, the geometry and energetics of the minima reinforce a view that the gross structure of vdW complexes is due to electrostatic interactions. Notice that the ratio of the hydrogen-bonded interaction energies for $N_2 \cdots H_2O$ and $OC \cdots H_2O$, 66%, agrees well with that calculated

above, 61%, from simple electrostatic arguments.

3.5 Intermolecular vibrations

3.5.1 Normal modes description and calculation

In order to quantify higher-energy portions of the IPSs, it is necessary to measure the intermolecular vibrations which have access to those regions. Like the vibrations of polyatomic molecules, intermolecular vibrations are poorly described by local modes, and instead involve the change in coordinates of many particles, the so-called normal mode analysis. Normal modes are those set of vibrational motions which are orthogonal to one another, that is, equilibrium excitation of one mode does not excite others. Of course the limitations of this description were shown with the discovery of time variance for vibrational Hamiltonians and the intramolecular vibrational energy redistribution effect; nonetheless, it is quite adequate for describing the time-averaged vibrational spectra of most molecules. In vdW molecules, the coupling of local modes to form normal ones can be quite extensive, owing to the the large anharmonicities in the vibrational potentials as well as the angular-radial coupling resulting from near cancellation of attractive and repulsive terms throughout much of the IPS. In fact, as seen in the AW1 and AW2 IPSs for Ar$\cdots$$H_2O$ in Section 1.6, angular-radial coupling can cause a breakdown of the normal mode analysis, where all intramolecular vibrations need to be treated simultaneously. In spite of this, it is helpful to begin with a normal mode approach for spectroscopic purposes.

As we calculated from Equation (1.3), the diatomic$\cdots$triatomic systems $N_2\cdots H_2O$ and $OC\cdots H_2O$ have five unique intermolecular modes. In a local mode analysis, an obvious representation of theses motions is the change in the one radial and four angular coordinates: R_{cm}, θ_{H_2O}, θ_{N_2}/θ_{CO}, ϕ_{H_2O}, and ϕ_{N_2}/ϕ_{CO}. However, experimental evidence from the rotation-tunneling spectra points to a coupling of the angular motions of H_2O and N_2 or CO. The structural analysis and *ab initio* studies show much weaker potentials for in-plane motions *vs.* out-of-plane motions, and this di-

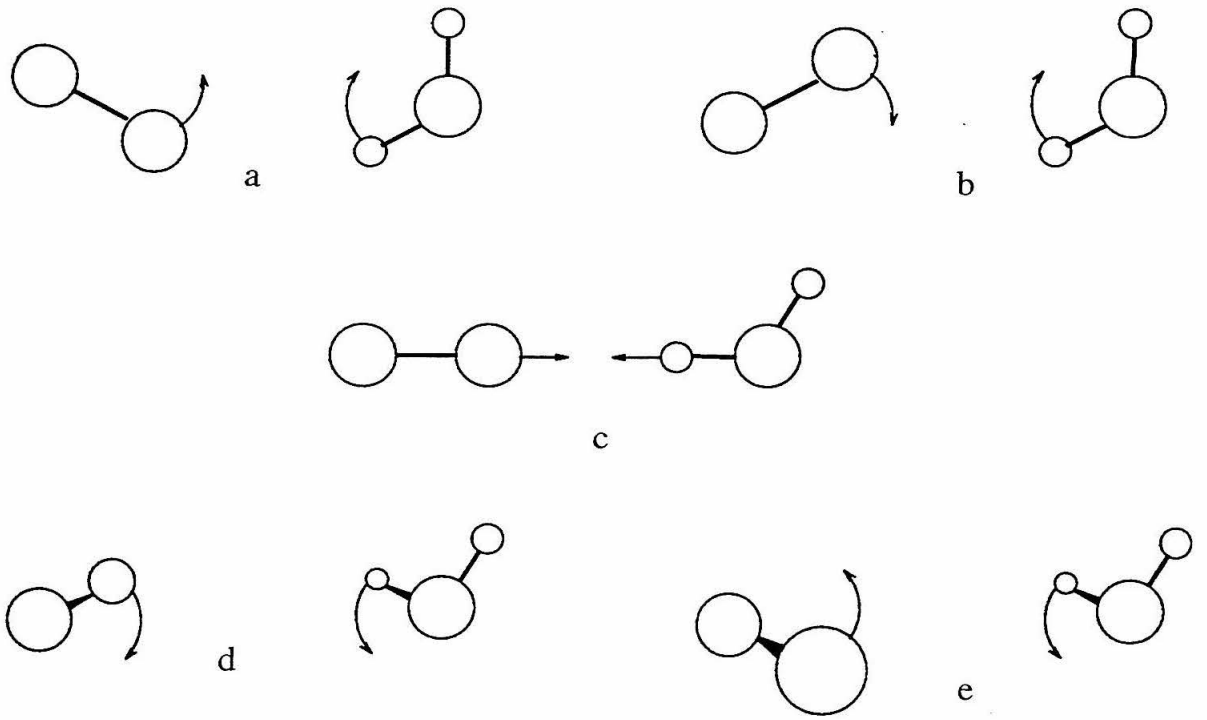

Figure 3.11: Proposed normal modes for planar diatomic···triatomic complexes: a) in-plane geared bend, b) in-plane anti-geared bend, c) vdW stretch, d) out-of-plane geared bend, and e) out-of-plane anti-geared bend.

vision of low frequency in-plane and high frequency out-of-plane motions provides a good starting point for a normal modes analysis. Coupling of the two in-plane and two out-of-plane angular local modes can be described by a geared and anti-geared rotation of the two monomer subunits with respect to each other, as shown in Figure 3.11. Tying them all together with angular-radial coupling is the vdW stretching mode.

Some of the authors from the two DMC studies went on to perform vibrational analysis on the *ab initio* surfaces which they generated for $N_2 \cdots H_2O$ and $OC \cdots H_2O$ [21]. These were performed in conjunction with low resolution IR spectra of N_2 and CO absorbed on ice surfaces. Unfortunately, these calculations were aimed at

Table 3.19: *Ab initio* intermolecular vibrational frequencies in cm^{-1} (and intensities in km/mol) for $N_2\cdots H_2O$ and $OC\cdots H_2O$ from Sadlej *et al.*

Mode	$N_2\cdots H_2O$	$OC\cdots H_2O$
ν_5 (in-plane, geared)	53 (10.6)	56 (10.4)
ν_6 (in-plane, anti-geared)	76 (18.7)	89 (12.1)
ν_7 (vdW stretch)	92 (0.1)	101 (1.34)
ν_8 (out-of-plane, geared)	192 (86.1)	219 (81.9)
ν_9 (out-of-plane, anti-geared)	266 (65.3)	312 (65.4)

providing only relative frequency shift information for comparing the complexes, and did not attempt to correct the frequencies for basis set superposition error (BSSE) or anharmonicity, and so the absolute values are questionably high. Regardless, the calculated frequencies provide a good assessment of the proposed normal mode analysis, and also give upper bounds to the experimental vibrational frequencies. Note also that tunneling is not included, and this could split or shift the the unperturbed vibrational frequencies by several wavenumbers. Their results, along with intensities, are given in Table 3.19. As predicted, the in-plane and out-of- plane modes are quite different in frequency. The vdW stretch, however, lies very close to the in-plane modes, and some Coriolis-type interactions among these three modes can be expected. Notice too that the intensity for the vdW stretch is quite weak, and any hope of seeing it with IR absorption spectroscopy lies in such a coupling which could borrow the needed dipole intensity.

3.5.2 FIR observation of intermolecular vibrations

As stated earlier, intermolecular vibrations for $N_2\cdots H_2O$ and $OC\cdots H_2O$ need to be measured in order to further characterize higher energy portions of their IPSs. Towards this end, a search was mounted to find such modes, and the following laser lines were used: 584 GHz (HCOOH), 692 GHz (HCOOH), 767 GHz (HCOOH), 1042 GHz (CH_2F_2), 1300 GHz (CH_3OD), 1397 GHz (CH_2F_2), 1546 GHz (CH_2F_2), and 1626 GHz (CH_2F_2). Absorption lines requiring both H_2O and N_2 or CO were eventually seen for $N_2\cdots H_2O$ between 1265 and 1335 GHz on the 1300 GHz laser line, and for

$OC\cdots H_2O$ between 1360 and 1560 GHz on the 1397 GHz and 1546 GHz laser lines. These are shown in Figure 3.12a and b. Due to their energy, these transitions could either be the sought-after intermolecular vibrational modes or $K = 1 \rightarrow 2$ rotationally "hot" bands. The first assignment is much more likely since these lines were seen under the same optimized expansion conditions used to observe the rotational transtions arising from the ground state. In the $H_3N\cdots H_2O$ complex studied in Chapter 4, a considerable reduction in the planar jet flow was necessary in order to warm the molecular beam so that the "hot" $K = 1$ levels at 20 cm^{-1} were populated. These groupings of lines correspond roughly to the predictions of Sadlej *et al.*, and are red-shifted from these by about 10%. In addition, because much of the lower frequency range was scanned without other transitions observed, these are most likely the lowest frequency ν_5 in-plane geared vibrations. The large spectral distribution of lines, particularly for $OC\cdots H_2O$, indicates that the tunneling splittings are much larger in this vibrationally excited state *vs.* the ground state, as expected.

Unfortunately, the spectra remain incomplete at present. Strong FIR laser lines are sparse in this region, and even the recognizable rotational progressions evident in Figure 12b are unassignable without more data. It is known that the high frequency $OC\cdots H_2O$ progression does terminate around 1565 GHz, but because the lower end has not been assigned, it cannot be even designated as a P- or R-branch at this time. Many laser lines have been attempted, especially between 1397 and 1546 GHz, but to no avail. However, the 1397 GHz and 1546 GHz CH_2F_2 laser lines are very strong, especially with the new output couplers, and these strong lines could be used to drive higher order sidebands from the Schottky diode mixer, allowing greater coverage of this region. Also, new optical photomixer FIR sources promise to make continuous coverage in the FIR available to spectroscopists in the not too distant future [22, 23].

3.6 Summary

The b-type $K = 0 \rightarrow 1$ rotational spectra for $N_2\cdots H_2O$ and $OC\cdots H_2O$, as well as isotopomers containing HOD, D_2O, and ^{13}CO, were recorded between 325 and 661

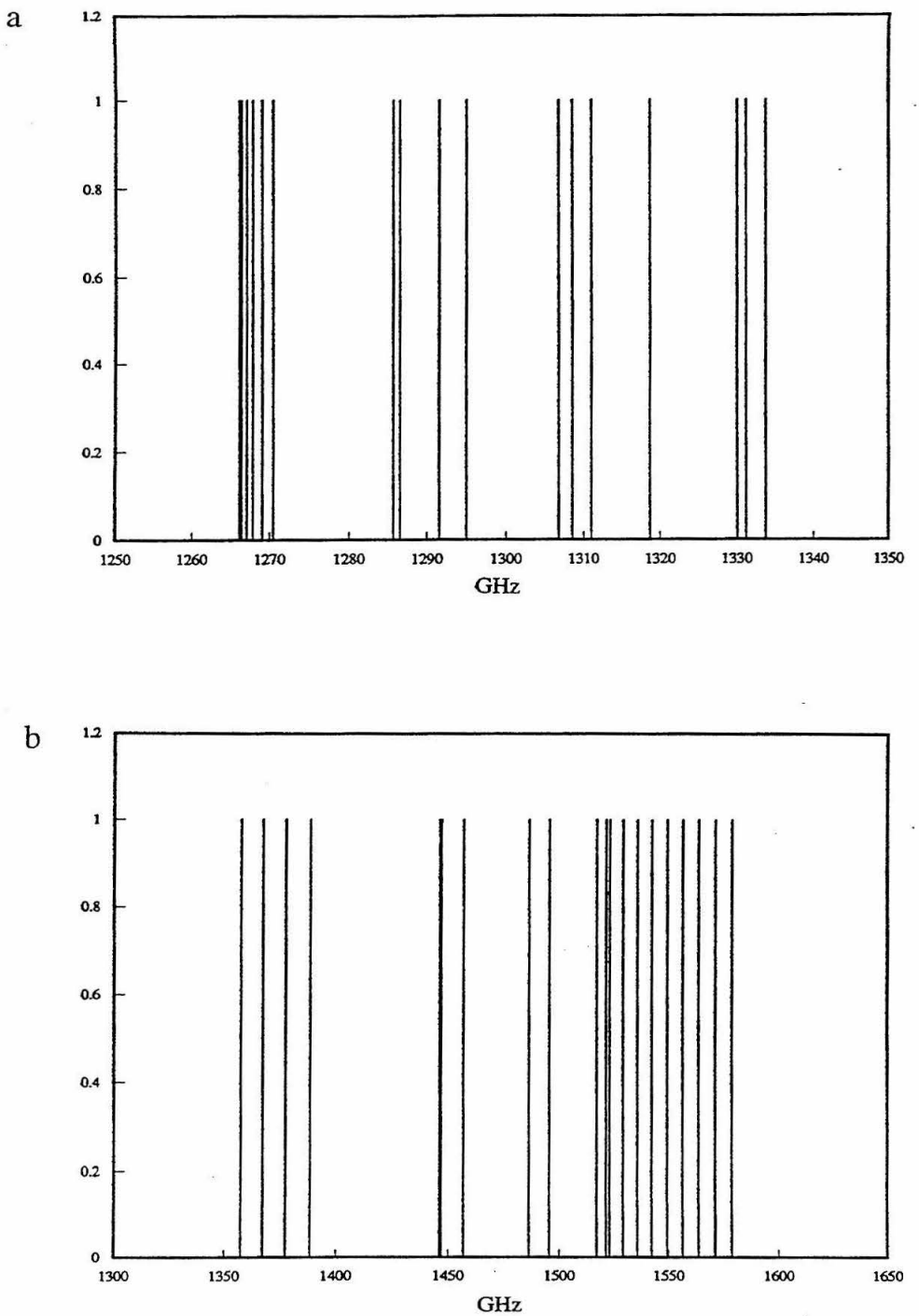

Figure 3.12: Observed FIR intermolecular VRT spectra for a) $N_2 \cdots H_2O$ and b) $OC \cdots H_2O$ complexes.

GHz using a FIR laser sideband spectrometer. Measurements were also extended for the a-type MW spectra of the $N_2\cdots H_2O$ and $OC\cdots H_2O$ isotopomers. Each rotational transition was split by the effects of large-amplitude tunneling of the hydrogen and nitrogen nuclei, and the number of tunneling components corresponded with that predicted from PI theory. After the effects of tunneling had been removed from the rotational constants, the structures of the two different complexes were fit to the rotational moments of inertia. These structures correspond to a nearly linear hydrogen bond and alignment of heavy atoms. The tunneling selection rules for $OC\cdots H_2O$ were confirmed to be "top-to-bottom, bottom-to-top", and the tunneling splittings were obtained from the difference in the A_{eff} rotational constants. Using two- and three-term Fourier expansions, the one-dimensional tunneling coordinate was fit to the tunneling splittings for $OC\cdots H_2O$ and $OC\cdots D_2O$. The $N_2\cdots H_2O$ rotational-tunneling analyses were complicated by the apparent coupling of nitrogen and hydrogen tunneling modes, as seen in the MW and FIR spectra. *Ab initio* surfaces were used both to visualize the tunneling modes and as a basis for normal mode analysis. A reasonable and justified normal mode separation was presented, with the five intermolecular degrees of freedom separated into geared and anti-geared in-plane and out-of-plane motions of the subunits as well as the intermolecular stretch. Finally, partial VRT spectra for both complexes recorded between 42 and 53 cm^{-1} were presented and preliminarily assigned to the in-plane geared motion.

Bibliography

[1] Y. Tanimura and S. Mukamel. Femtosecond Pump-Probe Spectroscopy of Intermolecular Vibrations in Molecular Dimers. *J. Chem. Phys.*, 103:1981, 1995.

[2] B. Nelander. A Matrix Isolation Study of the Water-Formaldehyde Complex. The Far-infrared Region. *Chemical Physics*, 159:281, 1992.

[3] T.A. Ramelot, C.-H. Hu, J.E. Fowler, B.J. Bradley, J. DeLeeuw, and Henry Schaefer, III. Carbonyl-Water Hydrogen Bonding: the H_2CO—H_2O Prototype. *J. Phys. Chem.*, 100:4347, 1994.

[4] P. Hobza and R. Zahradník. *Weak Intermolecular Interactions in Chemistry and Biology.* Elsevier, New York, 1980.

[5] P. Hobza and R. Zahradník. *Intermolecular Complexes.* Elsevier, New York, 1988.

[6] W. Gordy and R.L. Cook. *Microwave Molecular Spectra.* John Wiley and Sons, New York, 3rd edition, 1984.

[7] The sign of the molecular quadrupole moments for N_2 and CO seems counter-intuitive, at least for the author, at first consideration. The most prominent electronic feature of these diatomic molecules for chemists is the strong, multiple bond electrovalency in the center of the molecule, leaving a net charge deficit at either end of the molecule. However, on a local level, the dipole-quadrupole interaction energy falls off rapidly as r^{-4}, meaning that the quadrupole moment formed by the remaining non-bonding electrovalency and the nuclei has a strong force on the on-axis dipole. Interaction with the inner electrovalency takes the form of higher order multipole moments which fall off even faster with r.

[8] P.R. Bunker. *Molecular Symmetry and Spectroscopy.* Academic Press, New York, 1979.

[9] L.H. Coudert, F.J. Lovas, R.D. Suenram, and J.T. Hougen. New Measurements of Microwave Transitions in the Water Dimer. *J. Chem. Phys.*, 87:6290, 1987.

[10] Nick Pugliano. *Vibration-Rotation-Tunneling Dynamics in Small Water Clusters.* PhD thesis, University of California, Berkeley, 1992.

[11] H.O. Leung, M.D. Marshall, R.D. Suenram, and F.J. Lovas. Microwave Spectrum and Molecular Structure of the N_2–H_2O Complex. *J. Chem. Phys.*, 90:700, 1989.

[12] D. Yaron, K.I. Peterson, D. Zolandz, W. Klemperer, F.J. Lovas, and R.D. Suenram. Water Hydrogen Bonding: the Structure of the Water-Carbon Monoxide Complex. *J. Chem. Phys.*, 7095:92, 1990.

[13] T.R. Dyke, G.R. Tomasevich, W. Klemperer, and W.E. Falconer. Electric Resonance Spectroscopy of Hypersonic Molecular Beams. *J. Chem. Phys.*, 57:2277, 1972.

[14] M.D. Harmony, V.W. Laurie, R.L Kuczkowski, R.H. Schwendeman, D.A. Ramsay, F.J. Lovas, W.J. Lafferty, and A.G. Maki. Molecular Structure of Gas-Phase Polyatomic Molecules Determined by Spectroscopic Methods. *J. Phys. Chem. Ref. Data*, 8:619, 1979.

[15] R.H. Schwendeman. *Critical Evaluation of Chemical and Physical Structural Information.* National Academy of Sciences, Washington, D.C., 1972.

[16] H.B. Thompson. Calculation of Cartesian Coordinates and Their Derivatives from Internal Molecular Coordinates. *J. Chem. Phys.*, 47:3407, 1967.

[17] M.J. Frisch, M. Head-Gordon, H.B. Schlegel, K. Taghavachari, J.S. Binkley, C. Gonzalez, D.J. Defrees, D.J. Fox, R. A. Whiteside, R. Seeger, C.F. Melius, J. Baker, R.L. Martin, L.R. Kahn, J.J.P. Stewart, E.M. Fluder, S.Topiol, and J.A Pople. *Gaussian 88, Revision C*, 1988.

[18] V. Buch. Treatment of Rigid Bodies by Diffusion Monte-Carlo— Application to the Para-H_2...H_2O and Ortho-H_2...H_2O Clusters. *J. Chem. Phys.*, 97:726, 1992.

[19] P. Sandler, J. oh Jung, M.M. Szczęsniak, and V. Buch. The Complex of N_2 with H_2O, D_2O, and HDO: a Combined *Ab Initio* and Diffusion Monte Carlo Study. *J. Chem. Phys.*, 101:1378, 1994.

[20] J. Sadlej and V. Buch. *Ab Initio* Study of the Intermolecular Potential of Water-Carbon Monoxide Complex. *J. Chem. Phys.*, 100:4272, 1994.

[21] J. Sadlej, B. Rowland, J.P. Devlin, and V. Buch. Vibrational Spectra of Water Complexes with H_2, N_2, and CO. *J. Chem. Phys.*, 102:4804, 1995.

[22] G.A. Blake and P. Chen. A Solid State Optical Heterodyne Spectrometer in the Far-IR. In *Abstracts of the 50th International Symposium on Molecular Spectroscopy*, 1995.

[23] P. Chen and G.A. Blake. Submillimeter Applications of Optical Photomixing at Millimeter and Submillimeter Frequencies. In *Abstracts of the 50th International Symposium on Molecular Spectroscopy*, 1995.

Chapter 4 Vibration-Rotation-Tunneling Spectroscopy and Results for Ammonia-Water Dimer

4.1 Introduction

4.1.1 Motivation

The next step chosen in the study of water-containing hydrogen-bonded dimers is the ammonia-water dimer. This complex compliments the progression begun with $Ar\cdots H_2O$, $N_2\cdots H_2O$, and $OC\cdots H_2O$ in a number of ways. First, the strength of the interaction has now increased to within a factor of two of the strongest hydrogen-bonding interactions known. In comparison to the simple electrostatic calculations outlined in Figure 3.1 for $N_2\cdots H_2O$ and $OC\cdots H_2O$, $H_3N\cdots H_2O$ has a dipole-dipole interaction energy of 14.0 $\times 10^{-31}$ C^2m^{-1}, which is 40% stronger than $OC\cdots H_2O$. The stronger interaction energy has a large effect on the internal motions of the H_2O and NH_3 subunits. This polyatomic$\cdots$polyatomic complex also has the full six degrees of intermolecular freedom possible for any vdW dimer. Beyond dimers, things get much more complicated, as each additional polyatomic subunit adds another six degrees of freedom, so that $(H_2O)_3$ has 12 intermolecular modes and $(H_2O)_4$ has 18. Finally, this system represents an interaction of biologically, atmospherically, and chemically identifiable importance, each of which is examined in more detail below.

Hydrogen bonds and van der Waals interactions are ubiquitous in biologically important macromolecules, such as proteins and polynucleic acids, and determine much of their three-dimensional structure and folding dynamics. A large subset of these weak bonds are between nitrogen and oxygen containing moieties and nearby protons from similar species. Multiple possibilities for hydrogen bond donor and acceptor

roles exist, and preferences among these roles arise from the subtle effects of both chemical substitution and steric environment. The effects of substitution and local environment are important to consider when generalizing or extrapolating from one system to another. For example, the double helices of DNA contain repetitions of proton donation from amides and amines to carbonyls and other amides, and proton donation *from* amides and amines is a common theme in biology. Donations of hydrogen bonds from amides have been observed in gas-phase dimers of formamide with water and methanol by Lovas *et al.* [16]. For these, the nitrogen of formamide and the oxygen of either water or methanol act simultaneously as hydrogen bond acceptors, resulting in a cyclic structure with two hydrogen bonds. However, for gas phase ammonia, the "simplest amine," the preference for hydrogen bonding is, with the exception of the ammonia-benzene complex [2], for the acceptance of protons [3, 4]. This dispells the commonly held idea that ammonia is amphoteric in nature, both accepting and donating hydrogen bonds. Given this difference in acceptor/donor preference between gas phase ammonia and amine functional groups in solution, either the structures of sterically constrained amine hydrogen bonds do not reflect potential minima of the unconstrained functional groups or carbon bound amines interact significantly differently than unsubstituted ammonia.

Hydrogen bonds are also important cosmochemically. In a gas of solar composition, the most stable carbon, nitrogen, and oxygen containing species at the temperatures and pressures which characterize protostellar nebulae are methane, ammonia, and water. Ices, hydrates, and clathrates formed from these and other species, most notably CO, N_2, and the noble gases, may therefore play critical roles in the origin and evolution of outer solar system bodies [5]. For example, in the Saturnian system it has been estimated that the initial ice budgets of Titan as well as the smaller satellites may have contained up to as much as 15% ammonia-water hydrate [6]. The coexistence of a number of hydrate-clathrate systems determines, in part, the volatile inventories of comets, icy satellites, and other objects; and a detailed understanding of their formation kinetics, phase diagrams, and mechanical properties is essential over a wide range of temperatures and pressures. Accurate experimental measure-

ments sampling the entire parameter space provided by cosmochemical environments is exceedingly difficult. Theoretical models have therefore remained the prinicipal means of addressing the importance of ices in the early solar system [7].

Finally, the $H_3N\cdots H_2O$ complex represents the interaction of two fundamental chemical building blocks—the amino and the hydroxl groups—as well as two of the most important chemical feedstocks—ammonia and water. Even so, ammonia and water are by themselves completely unreactive at and below normal atmospheric temperature and pressure in the gas, liquid, and solid phases. Put in another way, this means that compound ammonium hydroxide, NH_4OH does not exist at normal temperature and pressure. Instead, ammonia and water form hydrates and clathrates, such as $2NH_3\cdot H_2O$, whose composition depends on the concentration of NH_3 and H_2O present [8]. However, when made more basic, for example with alkyl group substitution, amines willl react formally with water to form sustituted ammonium hydroxides like triethylammonium hydroxide. Ammonia and water do react sequentially with O_2 in the Otswald process, where, in the presence of heated platinum (750 to 900°C), ammonia reacts with oxygen to give NO, which then reacts with water to form HNO_3 [9]. Combined with the Haber process, this reaction converts N_2 into industrially useful precursors.

4.1.2 Vibration-rotation frameworks

In Figure 4.1, $H_3N\cdots H_2O$ is diagrammed in a principal axis coordinate system with the a-axis nearly colinear to the line connecting the centers of mass of the NH_3 and H_2O subunits. $R_{N\cdots O}$ again represents the separatation of the heavy atoms N and O. For this work, θ_{NH_3} and θ_{H_2O} are the angles between the NH_3 C_3 and H_2O C_2 symmetry axes and the a-axis of the complex. These are different from the angles defined against $R_{N\cdots O}$; however, because of the positions of the ammonia and water subunits at equilibrium, these two sets of angles are equivalent within the error of the structural analysis. Instead of using the ϕ coordinates to measure the out-of-plane tilt of the subunits, rotation about their symmetry axes, χ_{NH_3} and χ_{H_2O}, is used instead.

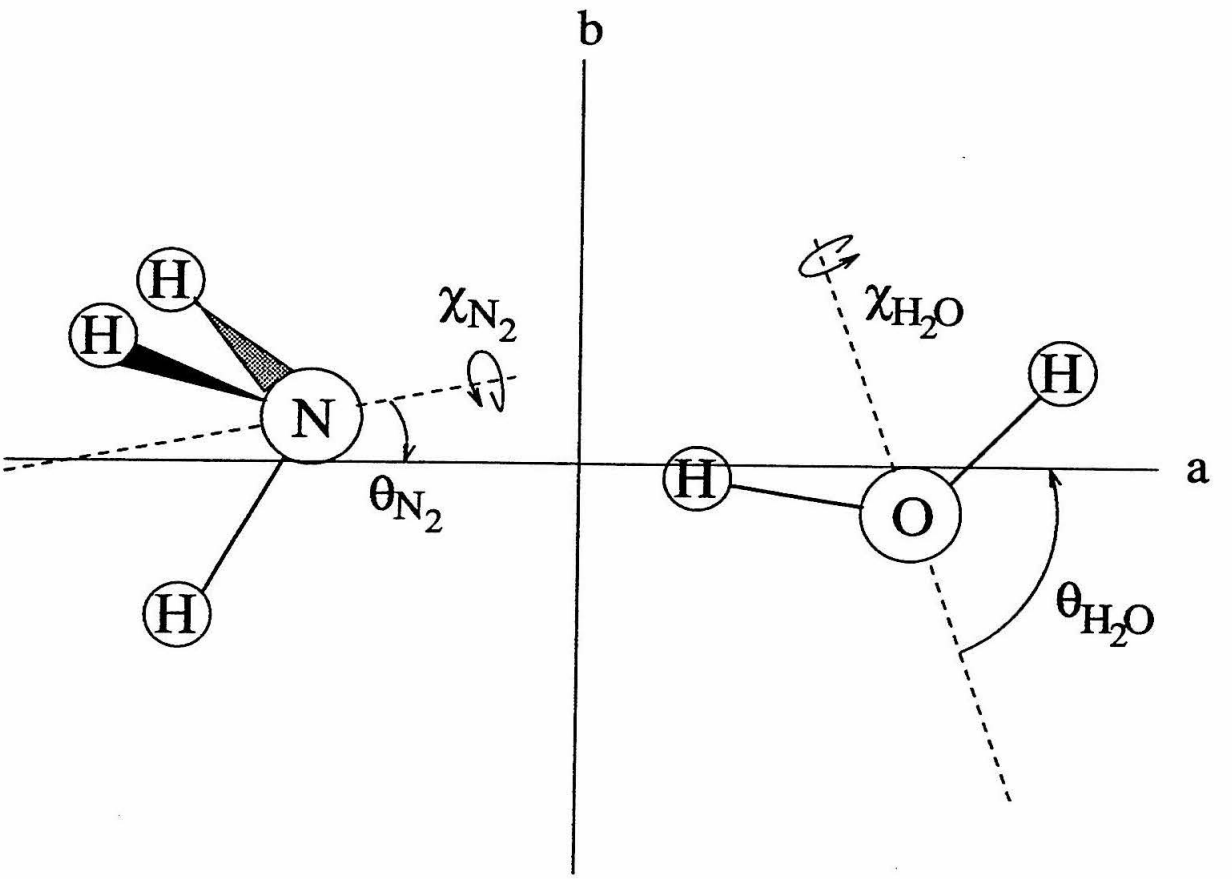

Figure 4.1: Structural parameters for $H_3N\cdots H_2O$.

Notice that there are only five of the six intermolecular degrees of freedom specified by Figure 4.1. The sixth coordinate is needed to specify the angular orientation of one subunit against the other, but will be unnecessary for the present discussion.

4.1.3 Tunneling and internal rotor frameworks

In the ammonia-water dimer, the ammonia monomer internally rotates about its C_3 axis and the water monomer tunnels between equivalent configurations in a double minimum potential. The three equivalent protons on ammonia and two equivalent protons on water give rise to six equivalent tunneling frameworks shown in Figure

4.2. Because the NH_3 subunit points its hydrogens away from the perturbing hydroxyl bond, rotation about its C_3 axis does not constitute tunneling in the true sense. However, as discussed earlier in Section 3.1.2, internal rotation potential barriers can cause perturbations to both eigenstates and eigenfunctions, and thus should be considered along with higher barriers. The "feasible" tunneling paths noted above lead to a G_{12} permutation-inversion group for the dimer. The character and correlation tables for this group as applied to nitromethane and methylamine may be found in Bunker [10] and Ohashi and Hougen [11]. The irreducible representations of this group are A_1', A_1'', A_2', A_2'', E′ and E″. The amount of NH_3 internal rotation is specified by the m quantum number. The internal rotation of the ammonia monomer about its symmetry axis splits the rotational levels of the dimer into two separate manifolds, analogous to those associated with the torsional motions of methyl and silyl groups of other molecules: an A symmetry manifold for $m = 0 \bmod 3$ and an E symmetry manifold for the remaining levels. States in the A manifold pair with one of the ammonia proton spin functions, $I = \frac{3}{2}$, while degenerate states in the E manifold pair with the $I = \frac{1}{2}$ spin functions. The two water tunneling states (spatially symmetric and antisymmetric) are associated with each value of m leading to the prime and double prime labels. The pairing of the ortho and para water spin functions with a given water tunneling function is determined by the symmetry of the rotational wavefunction and is discussed later.

4.2 Previous experimental and computational work

4.2.1 Experimental work

Again, prior to our work in the FIR with the $H_3N\cdots H_2O$ complex there existed a seminal MW study, this time conducted by Herbine and Dyke using an MBER apparatus [12]. These authors collected MW $J = 0 \rightarrow 1$ and $J = 1 \rightarrow 2$, as well as pure nuclear hyperfine, spectra for three different isotopomers: $H_3N\cdots H_2O$, $H_3N\cdots DOH$,

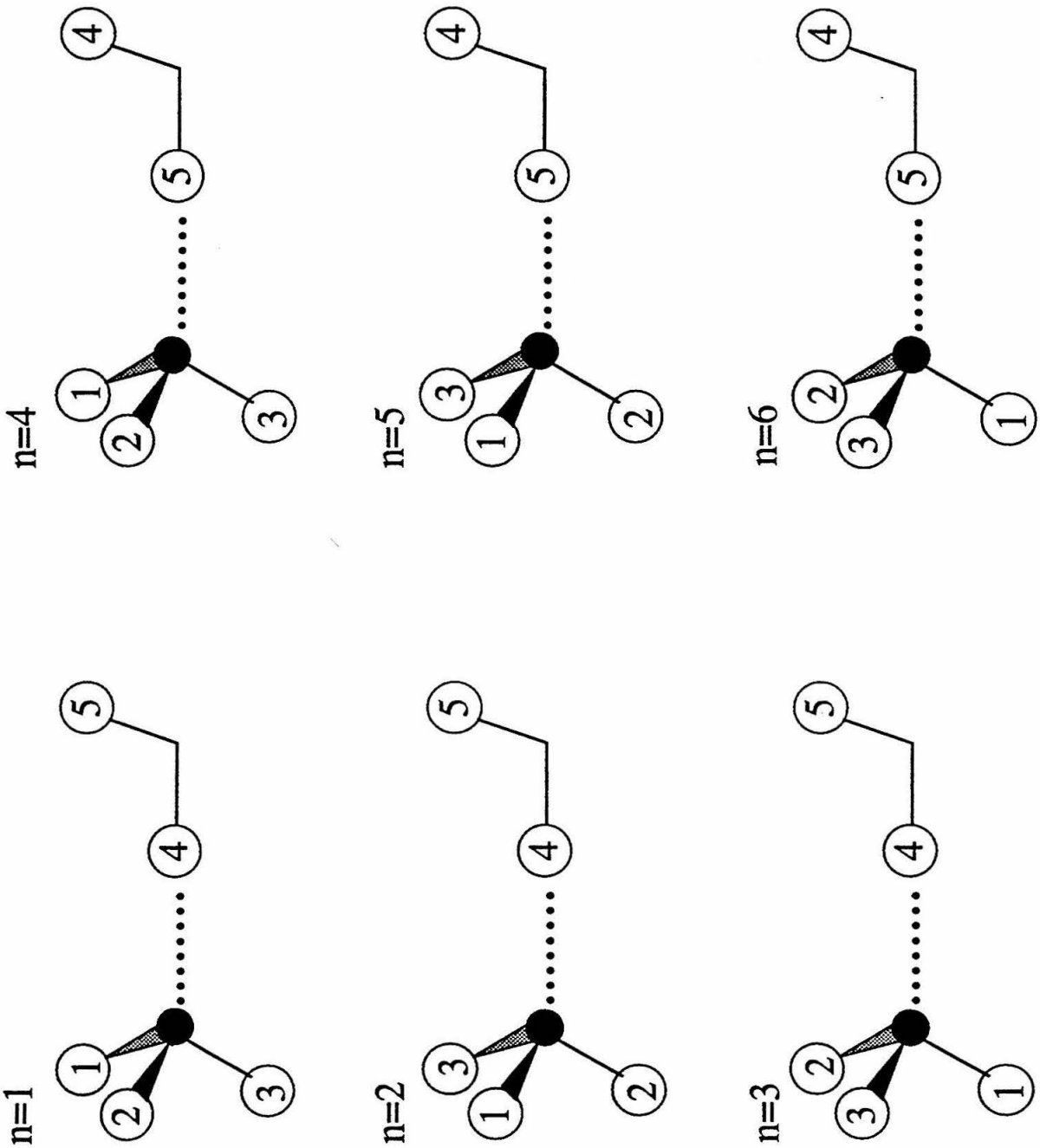

Figure 4.2: Tunneling frameworks for $H_3N\cdots H_2O$.

and $D_3N\cdots D_2O$. In addition to fitting the MW data to the $\bar{B} = (B+C)/2$ rotational constants, Herbine and Dyke also were able to measure $eQq_a(^{14}N)$ and the electric dipole moments parallel and perpendicular to the a-principal axis. Results from their structural calculations show the water subunit to reside within the C_s symmetry plane, with the following structural parameters: $R_{N\cdots O} = 2.983$ Å, $\theta_{N_2} = 23.1°$, and $\theta_{H_2O} = 56°$. Again, as in the MW studies of $N_2\cdots H_2O$ and $OC\cdots H_2O$, much of the structure determination involved evaluating the $\langle\cos^2\theta\rangle$ projections from the nuclear quadrupole coupling constants. In very similar work, Herbine, Dyke, and coworkers obtained and analyzed MBER MW spectra for $H_3N\cdots H_2S$ and several isotopomers [13]. They also recorded first-order Stark effect spectra for this asymmetric complex, which they correctly ascribed to a pairing of the excited internal rotor NH_3 E states with the $K = 1$ overall molecular rotation.

Several other experimental studies of $H_3N\cdots H_2O$, which bear less on the present discussion, have been published. Nelander and coworkers [14, 15] and Yeo and Ford [16] have all studied $H_3N\cdots H_2O$ complexes trapped in rare gas matrices. The primary focus of these works has been recording and analysing the perturbations of the ammonia and water intramolecular IR spectra. However, in the second study by Nelander, use of Mylar beam splitters enabled the researchers to measure spectra down to 10 cm^{-1} in energy. They recorded bands in Ne matrices at 19.5 cm^{-1} for both $H_3N\cdots H_2O$ and $D_3N\cdots H_2O$, which they assigned to the torsional motion of the complex. The motion which they observed, though, is likely to be much different than that seen in the present study, since the D_3N substitution had little effect on the frequency. A more probable motion is a hindered torsion of the H_2O subunit alone, with the ammonia rotation being quenched by the effects of the matrix. Supporting this interpretation is the fact that this mode was not observed for D_2O containing complexes nor for complexes formed in heavier, more perturbing rare gases.

Table 4.1: Comparison of various computed intermolecular binding energies and separations for the $H_3N\cdots H_2O$ complex.

Authors	Binding energy/(kcal mol^{-1})	$R_{N...O}$
Dykstra and Andrews	5.46	3.059
Yeo and Ford	6.43	2.960
Latajka and Scheiner	5.74	2.942

4.2.2 Computational work

The $H_3N\cdots H_2O$ complex also has been studied by several computational methods, although not to the degree given to the $N_2\cdots H_2O$ and $OC\cdots H_2O$ complexes. Some of theses papers deal with general interactions of second row hydrides and the efficacy of different computational approaches [17, 18, 19, 20]. While not focusing on $H_3N\cdots H_2O$ in particular, they provide a good comparison with other complexes among CH_4, NH_3, H_2O, and HF, as well as providing computational benchmarks for different methods. Three studies have found a global minimum geometry and binding energy for $H_3N\cdots H_2O$. The first, by Dykstra and Andrews, uses their self- developed code called molecular mechanics for clusters (MMC) [21]. This method uses high-order electrostatic properies of the monomers, many of which are calculated using conventional *ab initio* methods, to estimate the interaction in vdW complexes. Their results, along with the two *ab initio* works by Yeo and Ford [22] and Latajka and Scheiner [2], are summarized in Table 4.1. The two *ab initio* structures describe a nearly linear hydrogen bond, while the MMC calculation supports the more bent structure fit by Herbine and Dyke. More discussion of structure will follow in Section 4.3.3. Note that the D_0 binding energy calculated by Yeo and Ford is much larger than that of the other two works. The primary difference between this work and the *ab initio* work by Latajka and Scheiner is the smaller basis sets employed. Although Latajka and Scheiner do not show basis set expansion studies in their work, it is known that larger bases are needed to accommodate the long range forces associated with vdW bonds.

4.3 MW and FIR observation of rotation-tunneling modes

4.3.1 Observed data and experimental conditions

The MW absorption measurements were made in the region of 36 to 86 GHz. For a scan rate of about 200 MHz/hr, the average signal-to-noise ratio of the MW transitions was about 25 to 1. FIR spectra were collected from 520 to 800 GHz with the FIR laser tuned to the formic acid lines at 584.3882 GHz or 692.9513 GHz. A few of the low frequency FIR transitions were measured with a Rollin mode (zero field) InSb detector, but the large majority of lines were recorded using a Putley mode InSb detector at a field strength of 5.5 kGauss. For the FIR transitions, typical linewidths were only slightly broader than those observed with the microwave apparatus, 1.0 MHz (FWHM), with the strongest lines having a signal-to-noise ratio of 1000 to 1.

Ammonia-water clusters were produced by passing a stream of technical grade Ar over de-ionized H_2O, which was combined approximately 1 m upstream from the nozzle with a second line containing $NH_{3(g)}$. A third line of pure Ar was also added at this juncture. Using separate lines for Ar + H_2O and pure Ar allowed the water concentration to be adjusted at a fixed backing pressure simply by varying the relative flow rates rather than adjusting the temperature of the water. The evaporation of the water occurred at room temperature into a ~4 psig Ar stream. For both the microwave and the torsional ground states ($|m| \leq 1$) FIR measurements, a mixture of 1.116/3.427/0.0330 slm Ar/Ar + H_2O/NH_3 was found to give a maximum absorbance. Signal intensity was found to be much more dependent upon maintaining a backing pressure of ~500 Torr than upon the individual contributions of any of the gas flows. A lower flow rate of 2.000/0.0900 slm Ar + H_2O/NH_3 was used to observe torsionally hot FIR transitions ($|m| = 2$). This lowered the backing pressure to 250 Torr and raised the measured J-rotational temperature T_J from 4 K to 12 K. By eliminating either the Ar + H_2O or the NH_3 flows and compensating to the original backing pressure, signals due to ammonia, water, argon-ammonia, ammonia dimer

and argon-water species could be easily discerned from ammonia-water transitions.

Collisional cooling does not efficiently convert between nuclear spin states. Substantial populations in the lowest A' and A'' states ($m = 0, K = 0$) and the lowest E' and E'' states ($m = \pm 1$, $K = \pm 1$, $mK = +1$) are therefore produced in the molecular beam. Because the barrier to water tunneling is fairly high in this molecule (see Section 4.3.5), there is very little difference in the vibrationally averaged structure of water tunneling states. Thus, the $\Delta K = 0$ rotational transitions in the prime and double prime states (which do not cross the water tunneling splitting) are unresolved. Note that in both $N_2 \cdots H_2O$ and $OC \cdots H_2O$, where the barriers to water tunneling are smaller, the differences in the vibrationally averaged structures of the two water tunneling states produce observable splittings in the $\Delta K = 0$ transitions.

A total of 22 lines were observed in the MW spectra, of which 7 were assigned and fit as transitions of $H_3N \cdots H_2O$. Nine of the transitions appear to be hyperfine multiplets of the $J = 1 \rightarrow 2$ transitions of the lowest E and A states and were not included in the fit. Several remaining lines do not lie particularly close to any predicted pure rotational transition of $H_3N \cdots H_2O$ and have not yet been assigned. In the previous microwave work, Herbine and Dyke observed a-dipole, $J = 0 \rightarrow 1$ and $J = 1 \rightarrow 2$ rotational transitions in the A states. We were able to extend the observations of these states higher in frequency, up to the $J = 5 \rightarrow 6$ rotational transitions. We also observed an additional set of a-dipole transitions in the lowest E states. Both sets of transitions are presented in Table 4.2.

In the FIR, a total of 289 transitions were observed which required the presence of both NH_3 and H_2O. Of these, 260 were assignable to $H_3N \cdots H_2O$ transitions. Initial FIR searches in the 450–550 GHz range proved fruitless. At higher frequency were found six bands occurring in three pairs. The bands within each pair were separated by an almost constant 113 MHz, while the spacing between the pairs was wider and on the order of 10 GHz. All of the bands contained P-, Q-, and R-branches with Q-branch origins for each pair located approximately at 633, 643, and 653 GHz. Stick spectra of the Q-branches of all the observed bands are shown in Figure 4.3. In Figure 4.4, an expanded view of the Q-branches for the pair of bands at 633 GHz is

Table 4.2: Observed MW rotational-tunneling a-type transitions (*MHz*) for $H_3N\cdots H_2O$, calculated for $V_3 = 10.5$ cm^{-1}. "O–C" are the observed frequencies minus the frequencies calculated with the fit parameters.

J'	K'	J''	K''	m	measured	O–C
3	0	2	0	0	36852.32	0.08
4	0	3	0	0	49132.44	-0.17
5	0	4	0	0	61409.04	-0.44
6	0	5	0	0	73681.02	-1.13
3	1	2	1	1	36815.00	-0.53
4	1	3	1	1	49082.70	-0.72
6	1	5	1	1	73606.74	-1.41

presented. Figure 4.5 shows the signal-to-noise for a weak transition from the para 633 GHz band. By inference to the structure determined by Herbine and Dyke and because the 113 MHz splitting was approximately constant across all J's in all bands, this splitting was attributed to a tunneling effect of the water monomer. Also of note is the fact that in each pair of bands, one set of states was approximately three times stronger than the other, indicating that one band is associated with the ortho spin state of water while the other is associated with the para state. The additional splitting into three (and later we will see, five) bands is due to internal rotation of the ammonia group. Frequencies of the observed FIR transitions are given in Tables 4.3–6.

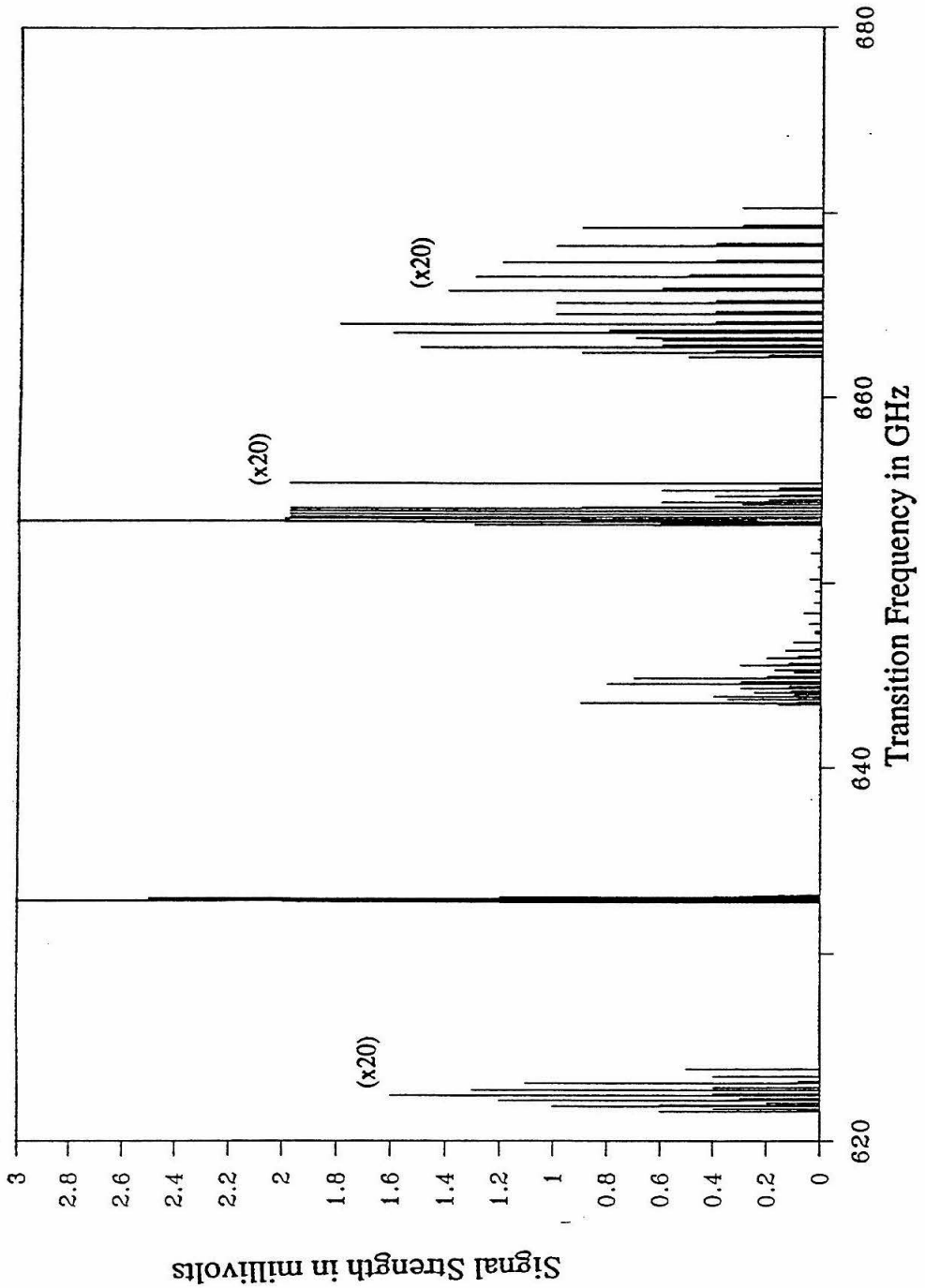

Figure 4.3: Observed FIR Q-branches for $H_3N\cdots H_2O$.

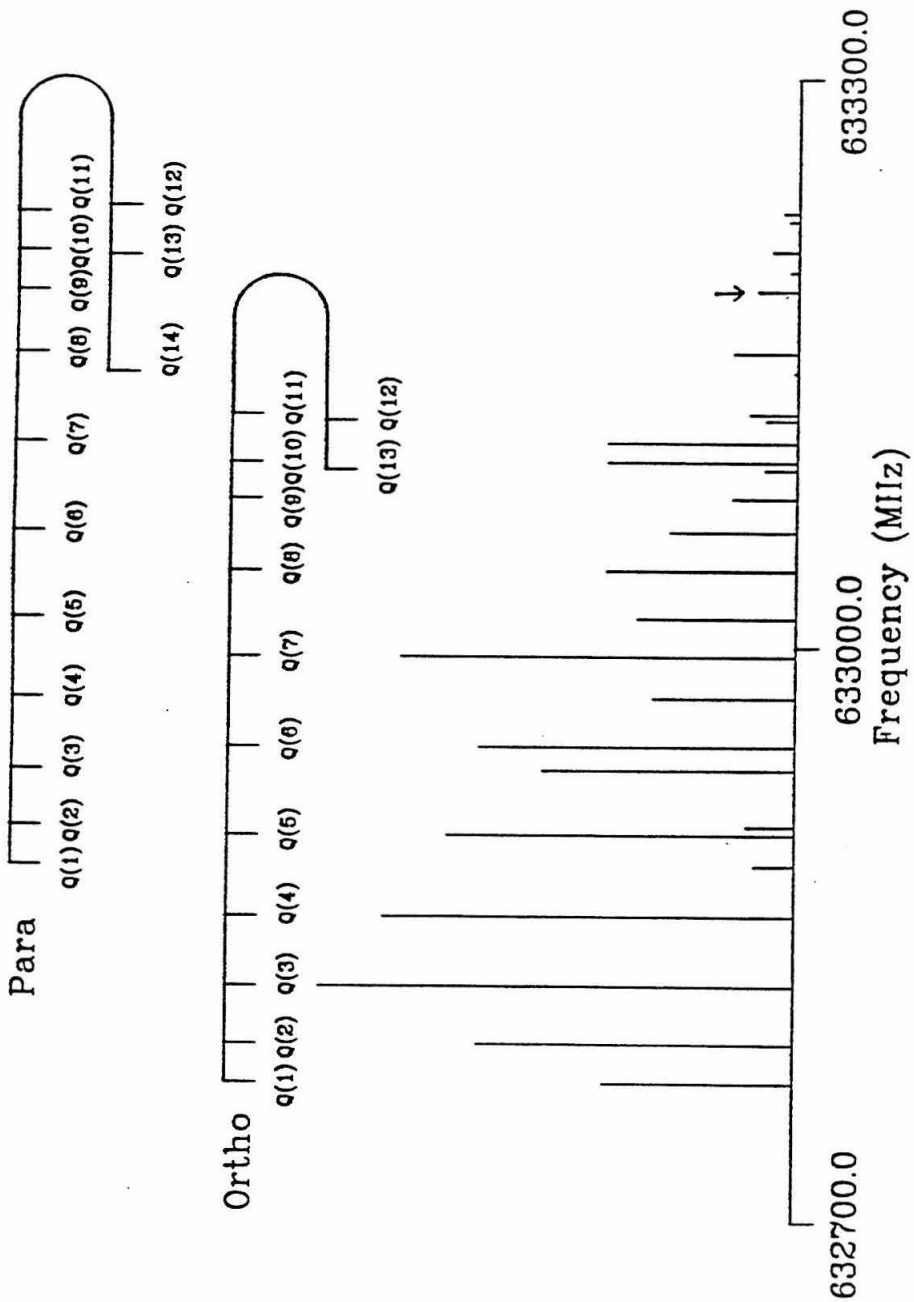

Figure 4.4: Ortho and para Q-branches for $H_3N\cdots H_2O$ 633 GHz bands. Note the constant 113 MHz separation between correponding ortho and para transitions and the approximate 3:1 intensity ratio. The para Q(9) transtion, maked with an arrow, is shown in Figure 4.5.

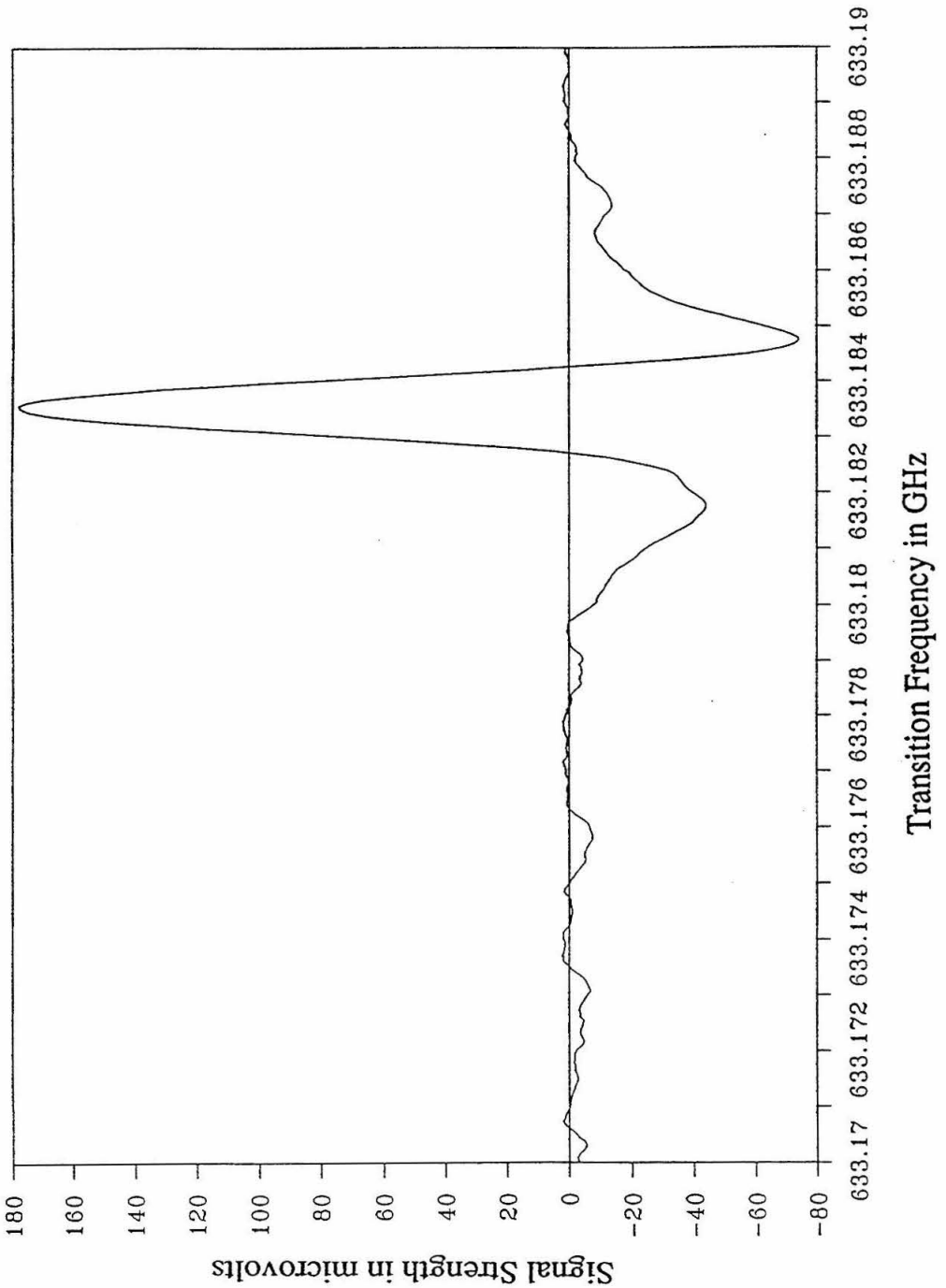

Figure 4.5: Signal-to-noise ratio for 633 GHz para Q(9) transition. S/N = 17/1 with a FWHM of 1 MHz.

Table 4.3: Observed FIR rotational-tunneling b-type transitions (MHz) for ortho and para water tunneling states of $H_3N\cdots H_2O$, calculated for $V_3 = 10.5$ cm^{-1}. "O–C" are the observed frequencies minus the frequencies calculated with the fit parameters.

K'	K''	m	ortho	O–C	para	O–C	
P(9)	-1	0	0	531565.6	1.3		
P(8)	-1	0	0	544107.0	-0.6	544218.4	-2.0
P(6)	-1	0	0	569103.0	-2.0	569219.2	-0.2
P(5)	-1	0	0	581555.3	-2.2	581672.9	0.4
P(4)	-1	0	0	593977.6	-0.7	594093.9	0.2
P(3)	-1	0	0	606366.3	-0.1	606484.0	2.0
P(2)	-1	0	0	618720.5	-0.5	618837.0	0.1
Q(1)	1	0	0	643360.5	1.0	643474.3	-1.2
Q(2)	1	0	0	643426.7	1.3	643542.7	1.3
Q(3)	1	0	0	643525.4	1.1	643641.4	1.2
Q(4)	1	0	0	643657.2	1.1	643772.6	0.7
Q(5)	1	0	0	643820.7	0.0	643936.5	0.1
Q(6)	1	0	0	644018.5	0.4	644134.0	0.3
Q(7)	1	0	0	644248.9	0.5	644361.4	-2.4
Q(8)	1	0	0	644512.7	1.3	644627.1	0.6
Q(9)	1	0	0	644807.8	0.8	644921.9	0.1
Q(10)	1	0	0	645135.2	-0.1	645249.4	-0.2
Q(11)	1	0	0	645496.3	0.2	645609.4	-0.4
Q(12)	1	0	0	645888.5	-0.8	646001.6	-0.7
Q(13)	1	0	0	646314.7	-0.2	646426.4	-0.5
Q(14)	1	0	0	646772.5	-0.3		
Q(15)	1	0	0	647262.1	-0.6		
Q(16)	1	0	0	647783.6	-1.1		
Q(17)	1	0	0	648336.9	-1.7		
Q(18)	1	0	0	648923.5	-0.6		
Q(19)	1	0	0	649540.8	-0.5		
Q(20)	1	0	0	650189.9	-0.1		
Q(21)	1	0	0	650870.2	0.3		
Q(22)	1	0	0	651582.0	1.0		
Q(23)	1	0	0	652324.1	1.1		
R(0)	-1	0	0	655577.6	1.7	655692.5	0.8
R(1)	-1	0	0	667790.2	1.8	667904.2	0.3
R(2)	-1	0	0	679964.6	1.3	680080.0	1.7
R(3)	-1	0	0	692097.4	-2.2	692212.8	-1.3
R(4)	-1	0	0	704196.3	-0.3	704310.3	0.0

Table 4.4: Observed FIR rotational-tunneling b-type transitions for $H_3N\cdots H_2O$, continued.

K'	K''	m	ortho	O–C	para	O–C	
R(5)	-1	0	0	716252.1	-1.3	716364.7	-1.4
R(6)	-1	0	0	728267.2	-1.7	728377.8	-2.6
R(7)	-1	0	0	740241.9	-0.6	740353.1	0.5
R(9)	-1	0	0	764059.7	0.0	764165.1	-1.0
R(10)	-1	0	0	775901.2	-0.3	776005.3	-0.4
R(11)	-1	0	0	787699.3	1.6	787802.1	2.8
P(8)	0	1	1	534884.7	2.6	534995.0	0.2
P(7)	0	1	1	547085.9	1.4	547196.8	-0.7
P(5)	0	1	1	571512.1	0.7	571623.5	-1.2
P(4)	0	1	1	583737.9	-1.2	583851.1	-1.5
P(3)	0	1	1	595977.0	-0.8	596090.8	-0.5
P(2)	0	1	1	608227.2	-0.8	608341.1	-0.4
P(1)	0	1	1	620488.8	-1.0	620603.0	-0.3
Q(1)	0	1	1	632772.2	-0.9	632885.7	-0.8
Q(2)	0	1	1	632792.5	-0.8	632906.2	-0.4
Q(3)	0	1	1	632822.2	-0.3	932935.2	-0.4
Q(4)	0	1	1	632859.1	-0.1	632973.0	0.8
Q(5)	0	1	1	632901.8	0.0	633015.0	0.7
Q(6)	0	1	1	634947.9	0.1	633060.7	0.9
Q(7)	0	1	1	632995.0	0.5	633107.2	1.2
Q(8)	0	1	1	633040.0	1.2	633149.5	-0.1
Q(9)	0	1	1	633078.0	0.6	633187.4	0.3
Q(10)	0	1	1	633107.2	0.9	633215.1	0.3
Q(11)	0	1	1	633122.1	0.6	633228.6	0.0
Q(12)	0	1	1	633119.1	0.2	633224.1	-0.1
Q(13)	0	1	1	633093.1	-1.0	633197.4	-0.1
Q(14)	0	1	1			633144.0	-0.2
R(1)	0	1	1	657337.9	-0.5	657453.1	1.5
R(2)	0	1	1	669638.4	0.4	669750.3	-0.6
R(3)	0	1	1	681943.4	0.7	682055.7	0.5
R(4)	0	1	1	694247.8	-1.9	694360.9	-0.8
R(5)	0	1	1	706556.4	0.5	706668.7	1.5
R(6)	0	1	1	718857.3	-0.5	718967.5	-0.8
R(7)	0	1	1	731150.7	-0.6	731261.6	0.9
R(8)	0	1	1	743433.9	1.5	743543.3	3.0
R(9)	0	1	1	755696.7	0.8	755801.0	-1.4
R(10)	0	1	1	767937.9	0.5	768041.0	-0.8
R(11)	0	1	1	780151.2	-0.5	780253.0	-0.7
R(12)	0	1	1	792333.8	0.0		
R(13)	0	1	1	804476.1	-2.5		

The bands at 643 and 633 GHz were assigned and matched with the microwave data by the method of combination differences. The two bands originating near 643 GHz matched with the states previously seen in the Dyke lab and the two bands near 633 GHz correspond to the new set of microwave transitions. The branches with origins at 643 GHz were $K = 0 \rightarrow 1$ in character and were assigned to the A-state $(m'', K'', m''K'' \rightarrow m', K', m'K' = 0, 0, 0 \rightarrow 0, \pm 1, 0)$ transition while the bands at 643 GHz were $K = 1 \rightarrow 0$ and were assigned as E-state $(m'', K'', m''K'' \rightarrow m', K', m'K' = \pm 1, \pm 1, +1 \rightarrow \pm 1, 0, 0)$ transitions. P-branches of the bands at 653 GHz were very weak and initially precluded their detection and a definite assignment. The constants obtained from a combined fit of the microwave data and the first four FIR bands were then used to predict a preliminary energy level diagram. From the calculated energy levels, we were able to assign the 653 GHz bands as $(m'', K'', m''K'' \rightarrow m', K', m'K' = \pm 1, \pm 1, +1 \rightarrow \pm 1, \pm 2, +2)$, find several P-branch transitions and include the bands into the fits. Our predicted energy level diagram also showed that the $(m, K, mK = \pm 2, \pm 2, +4)$ state was fairly low lying, ~540 GHz above $(m, K, mK = \pm 1, \pm 1, +1)$, and had allowed transitions to the $(m, K, mK = \pm 2, \pm 1, +2)$ and $(m, K, mK = \pm 2, \pm 3, +6)$ states between 600 and 700 GHz. Since V_3, the barrier to NH_3 internal rotation, was not well determined from the data accessing only the $m = 0$ and $m = \pm 1$ states, a search was mounted for transitions from the $(m, K, mK = \pm 2, \pm 2, +4)$ state. By raising the beam temperature as described above from T_J=4 to 12 K, these two transitions were indeed observed within 10 GHz of the predictions. Band origins occurred at 621 and 662 GHz, again with separate bands for both water tunneling states split by ~113 MHz.

4.3.2 Hamiltonian and data fitting

Since the NH_3 internal rotation is a low barrier case and the H_2O tunneling is a high barrier case, the observed band positions are mostly determined by the internal rotation part of the Hamiltonian with a secondary small splitting due to the water tunneling. The elegant tunneling path approach developed for the water dimer by

Table 4.5: Observed FIR rotational-tunneling b-type transitions for $H_3N\cdots H_2O$, continued.

K'	K''	m	ortho	O–C	para	O–C	
P(7)	2	1	1	567441.0	-0.4		
P(6)	2	1	1	579613.7	-0.7	579730.7	-1.5
P(5)	2	1	1	591811.1	0.9	591928.4	0.3
P(4)	2	1	1	604024.2	-1.6	604141.6	-2.2
P(3)	2	1	1	616256.7	-1.9		
Q(2)	2	1	1	653073.0	-1.1	653192.0	0.2
Q(3)	2	1	1	653109.3	0.0	653226.4	-0.4
Q(4)	2	1	1	653158.7	0.6	653279.1	3.6
Q(5)	2	1	1	653222.6	0.0	653340.4	0.7
Q(6)	2	1	1	653305.6	1.0	653421.6	0.2
Q(7)	2	1	1	653408.0	1.1	653524.4	1.1
Q(8)	2	1	1	653533.5	1.3	653649.2	1.0
Q(9)	2	1	1	653685.6	1.5	653800.2	0.6
Q(10)	2	1	1	653867.9	1.9	653981.5	0.6
Q(11)	2	1	1	654082.8	1.2	654196.7	0.9
Q(12)	2	1	1	654335.2	0.3	654449.3	1.0
Q(13)	2	1	1	654629.1	-0.6	654742.3	0.0
Q(14)	2	1	1	654967.9	-2.0	655080.1	-1.3
Q(15)	2	1	1	655355.7	-3.5		
R(1)	2	1	1	677617.2	-2.0	677735.9	-0.8
R(2)	2	1	1	689923.4	-1.4	690041.4	-0.7
R(3)	2	1	1	702241.2	-0.4	702358.2	-0.3
R(4)	2	1	1	714569.4	-1.1	714687.3	0.3
R(5)	2	1	1	726913.2	0.5	727026.2	-2.6
R(6)	2	1	1	739271.3	1.1	739387.4	1.8
R(8)	2	1	1	764040.3	1.3	764151.6	-1.2
R(9)	2	1	1	776457.0	1.3	776567.7	-0.6
R(10)	2	1	1	788898.1	0.6	789008.6	-0.4
R(11)	2	1	1	801369.5	1.8	801477.5	-0.3
P(7)	1	2	2	536803.6	2.3		
Q(2)	1	2	2	621577.6	-2.4	621690.1	0.4
Q(3)	1	2	2	621719.0	-1.6	621830.6	0.1
Q(4)	1	2	2	621906.2	0.2	622017.8	1.9
Q(5)	1	2	2	622135.1	0.9	622244.2	0.0
Q(6)	1	2	2	622404.6	1.8	622512.8	0.1
Q(7)	1	2	2	622710.4	1.3	622818.2	-0.6
Q(8)	1	2	2	623050.4	0.7	623159.6	0.4
Q(9)	1	2	2	623420.2	-0.8		
Q(10)	1	2	2	623815.6	-3.4		
R(3)	1	2	2	670836.5	-3.8	670947.9	-1.8

Table 4.6: Observed FIR rotational-tunneling b-type transitions for $H_3N\cdots H_2O$, continued.

K'	K''	m	ortho	O–C	para	O–C	
R(4)	1	2	2	683294.5	-1.0	683404.3	-0.4
R(5)	1	2	2	695791.3	4.5	695894.6	-1.0
R(6)	1	2	2	708311.4	0.9	708419.6	0.9
Q(4)	3	2	2	662127.5	0.6	662246.6	-0.1
Q(5)	3	2	2	662376.0	0.2	662494.7	-0.4
Q(6)	3	2	2	662677.6	-0.3	662796.1	-0.7
Q(7)	3	2	2	663034.3	-1.0	663152.6	-1.0
Q(8)	3	2	2	663450.3	0.2	663566.9	-0.8
Q(9)	3	2	2	663923.2	-1.5	664041.5	-0.2
Q(10)	3	2	2	664461.5	-0.5	664577.9	-0.3
Q(11)	3	2	2	665065.5	0.8	665179.7	-0.5
Q(12)	3	2	2	665736.7	0.5	665850.8	0.1
Q(13)	3	2	2	666480.3	0.9	666595.7	2.6
Q(14)	3	2	2	667297.8	0.1	667410.4	-0.1
Q(15)	3	2	2	668194.3	0.0	668306.1	-0.2
Q(16)	3	2	2	669171.8	-0.5	669282.7	-0.7
R(2)	3	2	2	698634.1	0.6	698754.2	0.9
R(3)	3	2	2	711060.7	-0.5	711181.6	1.2
R(4)	3	2	2	723537.5	0.4	723655.9	0.3

Hougen [24] and Coudert and Hougen [25] could in principle be used to fit matrix elements and tunneling splittings for both motions simultaneously, but is beyond the scope of the present work and hardly justified for the amount of data currently available for the $H_3N\cdots H_2O$ complex. Here, we have found it convenient to treat the problem as one of internal rotation in two separate water vibrational states. For an asymmetric top with a single 3-fold internal rotor, the Hamiltonian can be written as:

$$\hat{H} = \hat{H}_{Rot} + F(\vec{p} - \vec{P})^2 + \frac{1}{2}V_3(1 - cos(3\chi_{NH_3})). \tag{4.1}$$

Here, $\hat{H}_{Rot}$ is the standard asymmetric top rotational Hamiltonian used in Equation (3.2), while F is the effective rotational constant for the internal motions of the ammonia rotor about its symmetry axis. F is calculated as follows:

$$F = \frac{\hbar}{2I_{top}}, \tag{4.2}$$

$$r = 1 - \sum_g \frac{I_{top}\lambda_g}{I_g}, \qquad g = (a,b,c) \; or \; (z,x,y), \tag{4.3}$$

where I_{top} is the moment of inertia of the internal rotor about its symmetry axis, I_g is the moment of inertia of the molecule about the g principal axis, λ_g is the directional cosine between the symmetry axis of the top and the g axis, and $\vec{p}$ - $\vec{P}$ is the relative angular momentum between the top and the frame. The derivation of the Hamiltonian may be found in reference [26]. It is useful to examine some parts of the Hamiltonian and matrix elements in order to understand the spectrum. Hence, even though the matrix elements for the above Hamiltonian have been given in reference [27], they are reproduced here. $\hat{H}$ may be expanded to yield:

$$\begin{aligned}\hat{H} = {} & A'P_a^2 + B'P_b^2 + CP_c^2 \\ & -2F(\alpha P_a p + \beta P_b p) + F\alpha\beta(P_aP_b + P_bP_a) + Fp^2 \\ & +V(\chi_{NH_3}) + \hat{H}_{dist},\end{aligned} \tag{4.4}$$

where

$$\begin{aligned} A' = \; & A + F\alpha^2, & B' \; &= B + F\beta^2, \\ \alpha = \; & \lambda_a I_{top}/I_a, & \beta \; &= \lambda_b I_{top}/I_b. \end{aligned} \tag{4.5}$$

It has been assumed that λ_c is zero (*i.e.*, the C_3 axis of NH_3 lies in the a-b plane). $\hat{H}_{dist}$ contains quartic and hextic rotational distortion terms plus additional distortion terms which allow for changes in the rotational constants in the various internal rotor states. The non-zero matrix elements of the Hamiltonian used, Equation (4.4), in the prolate top-free rotor basis are:

$$\begin{aligned} \langle JKMm|\hat{H}|JKMm\rangle &= A'K^2 + \frac{1}{2}B' + C)[J(J+1) - K^2] \\ &\quad - 2F\alpha Km + Fm^2 + \frac{1}{2}V_3 \\ &\quad + \text{quartic and hextic distortion terms} \qquad (4.6) \\ \langle JKMm|\hat{H}|JK \pm 1Mm\rangle &= F\beta[\frac{1}{2}\alpha(2K \pm 1) - m][J(J+1) \\ &\quad - K(K \pm 1)]^{1/2} \qquad (4.7) \\ \langle JKMm|\hat{H}|JK \pm 2Mm\rangle &= \frac{1}{4}(B' - C)[J(J+1) - K(K \pm 1)]^{1/2}[J(J+1) \\ &\quad - (K \pm 1)(K \pm 2)]^{1/2} \\ &\quad + \text{quartic and hextic distortion terms} \qquad (4.8) \\ \langle JKMm|\hat{H}|JKMm \pm 3\rangle &= -\frac{V_3}{4}. \qquad (4.9) \end{aligned}$$

The quartic and hextic distortion corrections used in Equations (4.6) and (4.8) are the standard terms of the Watson A-reduced Hamiltonain in the I_r basis.

A few features of the above equations are particularly noteworthy. In Equation (4.4), it can be seen that one of the effects of internal rotation is to modify the effective rotational constants about the principal axes for which λ_g is non-zero. The diagonal matrix element term of -$2F\alpha Km$ in Equation (4.6) arises from the coupling of overall and internal rotation. For $mK \neq 0$, this term produces a large splitting, lowering the energy of states with a positive mK product and raising the energy of

the states with a negative mK product, with the splitting being directly proportional to F and α. The result is that for b-dipole transitions in states with $mK \neq 0$, the P-, Q- and R-branches all terminate on degenerate levels. This situation greatly aids in the assignment of b-dipole spectra for $mK \neq 0$ states since ground state combination differences with a-dipole transitions can be formed between Q-branches and P- or R-branches rather than just between P-branches and R-branches. A markedly different situation arises in a near prolate asymmetric top with a similar $(B-C)$ value in that the P and R branch transitions terminate on the lower level of an asymmetry split doublet while Q-branches terminate on the upper level. Since K_O is not a particularly useful quantum number for states with $m \neq 0$, all states are labeled with m, K and mK. Also since we are very near the prolate limit, we will drop the prolate subscript from K_P. For $m = 0$ states, a negative value of K indicates the lower level of an asymmetry doublet.

The assigned bands (two per water tunneling state) were fit to the Hamiltonian of Equation (4.6) in a non-linear least squares fit. The basis set was factored into A and E symmetry blocks and truncated at $|K| = 4$ and $|m| = 9$. Numerical tests showed that the energy levels of interest had converged to better than 50 kHz with this size basis. In order to reproduce our data to near experimental uncertainty, we found it necessary to allow λ_x and λ_z to vary independently in the fits, as opposed to constraining the sum $\lambda_x^2+\lambda_z^2$ to unity. There are two reasons for this. First, vibrational averaging will project a small amout of the internal top's angular momentum out of the x-z plane, and second, even in the limit of λ_y exactly zero, $\langle\lambda_x\rangle^2+\langle\lambda_z\rangle^2 \neq 1$. After all ten rotation-tunneling bands had been assigned and fit, an energy level diagram for the internal rotor states, showing both the observed transitions and the predicted energies for higher states, was calculated and is presented in Figure 4.6.

Once the additional bands were added to the fit (now 5 bands per water tunneling state) we found that several extra distortion terms were required. Specifically, we needed to permit $\bar{B} = (B+C)/2$ in the various m, K states and A in the $m = \pm 2$ states to vary relative to the $m = 0$ states. To accomplish this we added the following

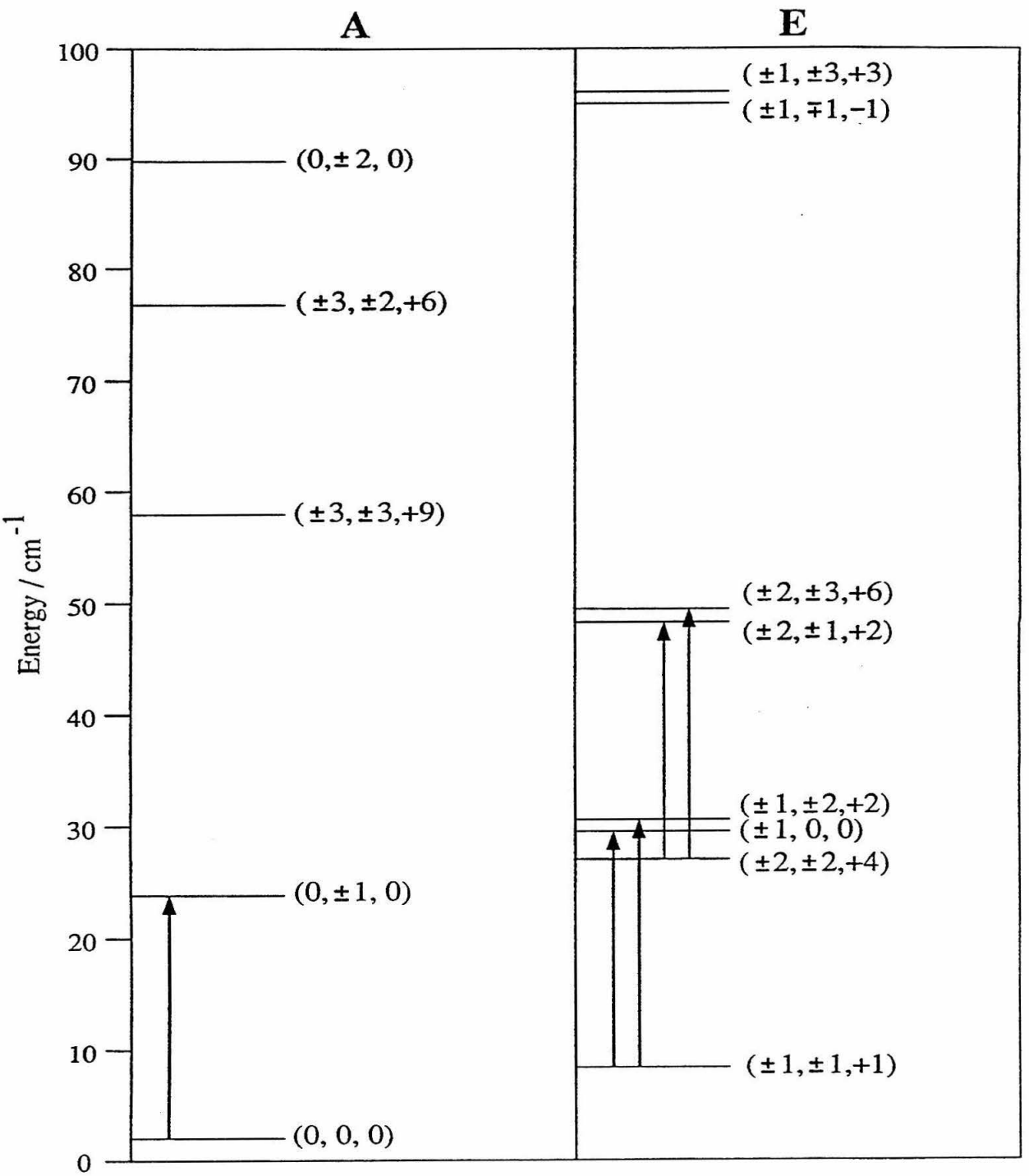

Figure 4.6: Energy level diagram for $H_3N\cdots H_2O$. States are separated into A and E symmetry manifolds and (m,K,mK) labeling is used.

terms to the diagonal of the Hamiltonian matrix:

$$\langle JKMm|\hat{H}_{int\ dist}|JKMm\rangle = \Delta\bar{B}_{m,K,mK}J(J+1), \quad (4.10)$$

$$\langle JKM,\pm 2|\hat{H}_{int\ dist}|JKM,\pm 2\rangle = \Delta A_{m=2}K^2. \quad (4.11)$$

In addition, it was also necessary to allow Δ_K and Δ_J for the $m = \pm 2$ states to assume different values than in the $m = 0$ and $m = \pm 1$ states. When all the additional distortion parameters necessary to reproduce the data to near experimental accuracy were included, there were again high correlations between V_3, the terms multiplied by the various powers of K in Equations (4.6)–(4.8) and the λ's. Note that the additional distortion terms are for specific values of mK. A more standard approach is to include higher order terms of the angular momentum cross product $f(i,j)P^ip^j$, where $i+j \geq 3$; $i,j \geq 1$; and $f(i,j)$ is a distortion constant. In this approach, *each* term operates on *all* $|m,K\rangle$ states [28]. However, our attempts to use distortion terms based on such angular momentum cross products never produced fits close to experimental error, and hence, we chose to use the distortion terms discussed above.

4.3.3 Structural analysis

The coordinate system and notation used to describe the complex are shown in Figure 4.1 and are the same as were used by Herbine and Dyke. Since only five of the six angles are independent, ϕ_{H_2O} was fixed at zero. As noted earlier in the MW work, the inertia tensor is invariant to rotation of the ammonia top about its symmetry axis, so no information about the average ammonia conformation is available from the rotational constants, and thus χ_{NH_3} was also set to zero. This leaves five structural parameters to be determined: $R_{N\cdots O}$, θ_{NH_3}, ϕ_N, θ_{H_2O} and χ_{H_2O}.

Intuition would lead to the prediction of C_S symmetry for the dimer structure. This is borne out in *ab initio* calculations discussed above and in the fact that $\lambda_x^2 + \lambda_z^2 \approx 1$. For a C_S structure, only $R_{N\cdots O}$, $\theta - NH_3$, and θ_{H_2O} need to be determined. Our data allows the determination of all three rotational constants for the single isotopomer, $H_3N\cdots H_2O$. In principle, all three structural parameters are obtainable

from the rotational constants of $H_3N\cdots H_2O$ alone. However, the main contribution to $(B-C)$ is due to the out-of-plane protons on the ammonia and $(B-C)$ is only weakly dependent on θ_{NH_3} or θ_{H_2O}. Hence, we must fix one of the two angles at a value determined by other data or use data from other isotopomers. Since we have determined λ_z from the internal rotor analysis, we have an independent measure of the average projection of the ammonia symmetry axis onto the a-axis. One method of approximating θ_{NH_3} is from the measured value of λ_z,

$$\lambda_z \simeq \langle\cos(\theta_{NH_3})\rangle \simeq \cos\langle\theta_{NH_3}\rangle, \tag{4.12}$$

where the average is taken over the complete vibrational wavefunction. Using Equation (4.12), we obtain $\theta_{NH_3}^{\lambda_z}$=11°. This differs significantly from the 23.1° value obtained by simple projection of the free monomer's nuclear quadrupole coupling constant onto the dimer a-axis and merits some discussion.

The nitrogen quadrupole coupling constant is a measure of $\langle\cos^2(\gamma_{NH_3})\rangle$, while λ_z is a measure of $\langle\cos(\gamma_{NH_3})\rangle$, where γ_{NH_3} is the angle between the C_3 axis of NH_3 and the a-axis of the complex. For a one-dimensional harmonic oscillator in θ with wave functions of the form

$$\Psi = (\frac{\alpha}{\pi})^{\frac{1}{4}} e^{-[\alpha(\theta-\theta_{eq})^2]/2}, \tag{4.13}$$

vibrational averaging yields

$$\langle\cos\theta\rangle \approx \cos\theta_{eq}\cdot e^{-\frac{1}{4\alpha}} \text{ and} \tag{4.14}$$

$$\langle\cos^2\theta\rangle \approx \cos^2\theta_{eq}\cdot e^{-\frac{1}{\alpha}} + \frac{1}{2}(1-e^{-\frac{1}{\alpha}}), \tag{4.15}$$

$$\tag{4.16}$$

where it has been assumed that the wavefunctions are localized enough to allow replacement of $\pm\pi$ in the integration limits with $\pm\infty$. From Equations (4.14) and (4.15) it can be seen that $\langle\cos\theta\rangle$ lies closer to the value of $\cos\theta_{eq}$ than does $[\langle\cos^2\theta\rangle]^{\frac{1}{2}}$ because of the difference in the exponential factors, $e^{-\frac{1}{4\alpha}}$ *vs.* $e^{-\frac{1}{2\alpha}}$. Hence, even for a one-dimensional harmonic oscillator, there is a difference between $\cos^{-1}[\langle\cos\theta\rangle]$ and

$\cos^{-1}[\langle\cos^2\theta\rangle]^{\frac{1}{2}}$.

If the ammonia projection on the a-axis were a one-dimensional *problem* (*i.e.*, $\gamma_{NH_3} = \theta_{NH_3}$), Equations (4.14) and (4.15) would allow an estimation of both $[\theta_{NH_3}]_{eq}$ and α from the values of $\langle\cos\gamma_{NH_3}\rangle$ and $\langle\cos^2\gamma_{NH_3}\rangle$ determined from λ_z and the nitrogen quadrupole coupling constant. However, the angle γ_{NH_3} is a function of both θ_{NH_3} and ϕ_{NH_3}. For $H_3N\cdots H_2O$, the in-plane and out-of-plane NH_3 bending modes are calculated by *ab initio* methods [2] to differ by only 19%. Therefore, the root-mean-square displacement from equilibrium of the ammonia symmetry axis will be similar in both the θ_{NH_3} and ϕ_N coordinates. Inclusion of out-of-plane vibrational averaging will magnify the difference between and $\cos^{-1}[\langle\cos\gamma_{NH_3}\rangle]$ and $\cos^{-1}[\langle\cos\gamma^2_{NH_3}\rangle]^{\frac{1}{2}}$ and make the extraction of θ from the measurement of these quantities ambiguous.

Because of the uncertainty in the value of $\langle\theta_{NH_3}\rangle$, we chose to examine structures with θ_{NH_3} fixed at both 11° and 23°. Fits of θ_{H_2O} and $R_{N\cdots O}$ were performed to the $m = 0$ rotational constants obtained in this work. The FORTRAN program `STRFTQ` developed by Schwendeman [22] and later modified by Frank Lovas at NIST, Gaithersburg was used. The usual assumption that the structures of the monomers remain unchanged upon complexation were made. The values of the vibrationally averaged structural constants for water and ammonia were taken from Harmony *et al.* [23]. Preliminary surveys of the θ_{H_2O} parameter space revealed the existence of four structures consistent with the rotational constants for each value of $|\theta_{NH_3}|$ chosen. Two of these structures had the H_2O protons pointing away from the ammonia and can be discounted by the deuterium substitution measurements of Herbine and Dyke. The values of θ_{H_2O} and $R_{N\cdots O}$ for the remaining two structures (1) and (2) are reported in Table 4.7 for a) $\theta_{NH_3} = 11°$ and b) 23°, and also for the *ab initio* calculated equilibrium structure (3) of Latajka and Scheiner.

Of the two remaining fitted structures, (1) and (2), structure (1) points the bonding hydrogen of the water monomer away from the lone pair of the ammonia nitrogen, and conversely, structure (2) aligns them. Calculations on a one-dimensional water tunneling potential (discussed below), indicate the vibrationally averaged in-plane water angle lies within a few degrees of the equilibrium value. Hence, we prefer struc-

Table 4.7: Fitted structural parameters for $H_3N\cdots H_2O$ and comparison with *ab initio* values of Latajka and Scheiner.

	θ_{H_2O}/°	$R_{N\cdots O}$ /Å
structure (1a) $\theta_{NH_3} = 11.1°$	-62.9	2.972
structure (1b) $\theta_{NH_3} = 23.1°$	-49.2	2.989
structure (2a) $\theta_{NH_3} = 23.1°$	63.2	2.972
structure (2b) $\theta_{NH_3} = 23.1°$	49.8	2.989
ab initio $\theta_{NH_3} = 9.5°$	59.2	2.942

ture (2) since it is similar to the structure obtained by *ab initio* calculations and since it has a more linear hydrogen bond. Comparison of (2a) and (2b) shows very similar values for $R_{N\cdots O}$ but significantly different values for θ_{H_2O}, with (2b) being more linearly hydrogen bonded than (3a). The *ab initio* structure has a θ_{NH_3} similar to (2a) and θ_{H_2O} between those of (2a) and (2b); $R_{N\cdots O}$ is 0.03 Å less than the experimental value. The average structure from this work (2a) has an NOH angle of $\sim 13°$. If we assume that the change in water H_2O angle upon complexation is +3° as calculated by Latajka *et al.*, we can reduce the average NOH angle to 10°. This compares to an *ab initio* equilibrium value of 4.8°.

4.3.4 Barrier to internal rotation of NH_3 subunit

Since it was not possible to absolutely determine V_3 from the data at hand, fits were performed over a range of V_3's. Examination of the sum $\lambda_x^2 + \lambda_z^2$ for a variety of V_3 values showed that the sum increased monotonically with the barrier height, and reached a value of unity near $V_3 = 25.0$ cm^{-1}. Hence, 25.0 cm^{-1} is taken as an approximate upper limit to V_3. It should be noted that with the current data set, correlations between various parameters only allow us to place limits of 0.0 cm$^{-1} \leq V_3 \leq 25$ cm^{-1}. However, when $\lambda_x^2+\lambda_z^2$ was constrained to unity, the standard deviation of the fit was several fold worse but V_3 was not significantly correlated with other parameters and was determined to be $\sim$10.5 cm^{-1}. Also, the fitted changes in A and Δ_K relative to the $m = 0$ state are significantly lower for $V_3 = 10.5$ cm^{-1} than $V_3 = 0.0$ cm^{-1}. Hence, we feel $V_3 = 10.5 \pm 5.0$ cm^{-1} is a good estimate of the barrier

Table 4.8: Fitted spectroscopic constants for the ortho tunneling state of $H_3N\cdots H_2O$.

	$V_3 = 0.0$ cm^{-1}	$V_3 = 10.5$ cm^{-1}
A (MHz)	147709.59 (30)	147608.29(30)
B (MHz)	6168.864(74)	6168.860(75)
C (MHz)	6110.564(49)	6110.556(49)
Δ_J (kHz)	34.69(15)	34.69(15)
Δ_{JK} (MHz)	1.0243(74)	1.0221(74)
Δ_K (MHz)	70.319(71)	46.215(71)
δ_K (MHz)	-1.159(24)	-1.160(24)
H_{JK} (Hz)	-536.4(96)	-536.3(96)
H_{KJ} (kHz)	285.3(23)	284.1(23)
λ_x	0.17270(22)	0.17289(23)
λ_z	0.9813315(25)	0.9819034(25)
$\Delta A_{m=\pm2}$(MHz)	653.01(53)	23.08(53)
$\Delta_{K,m=\pm2}$(MHz)	97.899(42)	37.341(42)
$\Delta\bar{B}_{\pm1,\pm1,+1}$ (MHz)	-2.089 (33)	-2.084(33)
$\Delta\bar{B}_{\pm1,0,0}$ (MHz)	-2.089(33)	-2.084(33)
$\Delta\bar{B}_{\pm2,\pm1,+2}$ (MHz)	6.019 (58)	6.009(59)
$\Delta\bar{B}_{\pm2,\pm2,+4}$ (MHz)	16.049 (94)	16.04(94)
$\Delta\bar{B}_{\pm2,\pm3,+6}$ (MHz)	27.67 (19)	27.61(20)
$\Delta_{J,\pm2,\pm3,+6}$(kHz)	37.8(17)	37.3(42)

height. In Tables 4.8 and 4.9 fitted parameters for both water tunneling states are reported with V_3 fixed at 10.5 cm^{-1} and 0.0 cm^{-1} for comparison.

4.3.5 Water tunneling in $H_3N\cdots H_2O$

The nearly constant value of 113 MHz ($\pm$ 3 MHz) between the lower and higher frequency tunneling state transitions along with an approximate 3:1 intensity ratio for lower relative to higher frequency transitions allows the construction of an energy level diagram including the effect of water tunneling. The 3:1 intensity ratio is indicative of an ortho:para partition of the spin states of the water protons. Because the splitting is constant in each of the five pairs of transitions observed, all transitions must be crossing a water tunneling splitting which is *not* a strong function of m or K. Also, because the intensity ratio always favors the lower frequency transitions, we conclude that these transitions are associated with the ortho water spin state. As is discussed in

Table 4.9: Fitted spectroscopic constants for the para tunneling state of $H_3N\cdots H_2O$.

	$V_3 = 0.0$ cm^{-1}	$V_3 = 10.5$ cm^{-1}
A(MHz)	147713.78(41)	147612.51(41)
B(MHz)	6168.74(10)	6168.73(10)
C(MHz)	6110.750(75)	6110.744(75)
Δ_J (kHz)	34.96(16)	34.95(16)
Δ_{JK}(MHz)	1.070(16)	1.068(11)
Δ_K(MHz)	70.378 (64)	46.283 (65)
δ_K(MHz)	-1.288 (37)	-1.289 (37)
H_{JK}(Hz)	-632(37)	-633(37)
H_{KJ}(kHz)	297.0(29)	295.8(29)
λ_x	0.17149(31)	0.17169(31)
λ_z	0.9813462(35)	0.9819178(35)
$\Delta A_{m=\pm 2}$(MHz)	654.25(55)	24.65(55)
$\Delta_{K,m=2}$(MHz)	98.019(45)	37.490(45)
$\Delta\bar{B}_{\pm 1,\pm 1,+1}$ (MHz)	-2.123(34)	-.118(34)
$\Delta\bar{B}_{\pm 1,0,0}$ (MHz)	-2.123(34)	-.118(34)
$\Delta\bar{B}_{\pm 2,\pm 1,+2}$ (MHz)	5.985(62)	5.974(62)
$\Delta\bar{B}_{\pm 2,\pm 2,+4}$ (MHz)	16.46(12)	16.45(12)
$\Delta\bar{B}_{\pm 2,\pm 3,+6}$ (MHz)	28.64(24)	28.57(24)
$\Delta_{J,\pm 2,\pm 3,+6}$(kHz)	38.26(22)	38.24(22)

more detail below, the observed selection rules are "top-to-bottom" and "bottom-to-top." That is, the lower frequency transitions originate from the upper water tunneling state and terminate on the lower water tunneling state, while the higher frequency transitions originate from the lower water tunneling state and terminate on the upper water tunneling state. The lower water tunneling state is always spatially symmetric while the upper tunneling state is spatially antisymmetric. Consequently, in order to reproduce both the observed intensity and tunneling splitting data, the pairing of the ortho and water spin functions with the spatial water tunneling functions must be a function of both m and K. Specifically, when $m + K$ is even, the ortho water spin function pairs with antisymmetric spatial function and the para spin function pairs spatially symmetric water tunneling function. When $m + K$ is odd, the pairing is reversed. This yields the symmetry state pairing diagram shown in Figure 4.7, which is consistent with the observed spectra.

The water tunneling splitting of 113 MHz is a measure of the the barrier to H_2O proton exchange. The "top-to-bottom, bottom-to-top" selection rules for this motion demonstrate that the tunneling motion is in the a-b plane of the dimer and give rise to transitions separated by twice the energy level splitting. Consequently, the tunneling energy level splitting should be roughly half of the observed splitting or 56.5 MHz. If we assume the equilibrium position of the water and ammonia monomers are close to their vibrationally averaged positions, then a simple one-dimensional model may be used to *estimate* the barrier to water tunneling. Like for $OC\cdots H_2O$, we write the potential as a two term Fourier expansion in the water angle θ_{H_2O}:

$$V(\theta_{H_2O}) = \frac{V_1}{2}(1 - \cos\theta_{H_2O}) + \frac{V_2}{2}(1 - \cos(2\theta_{H_2O})), \tag{4.17}$$

which determines

$$-\frac{V_1}{4V_2} = \cos\theta_{eq}, \tag{4.18}$$

where θ_{eq} is the equilibrium angle which we estimate at 63° from the STRFTQ results.

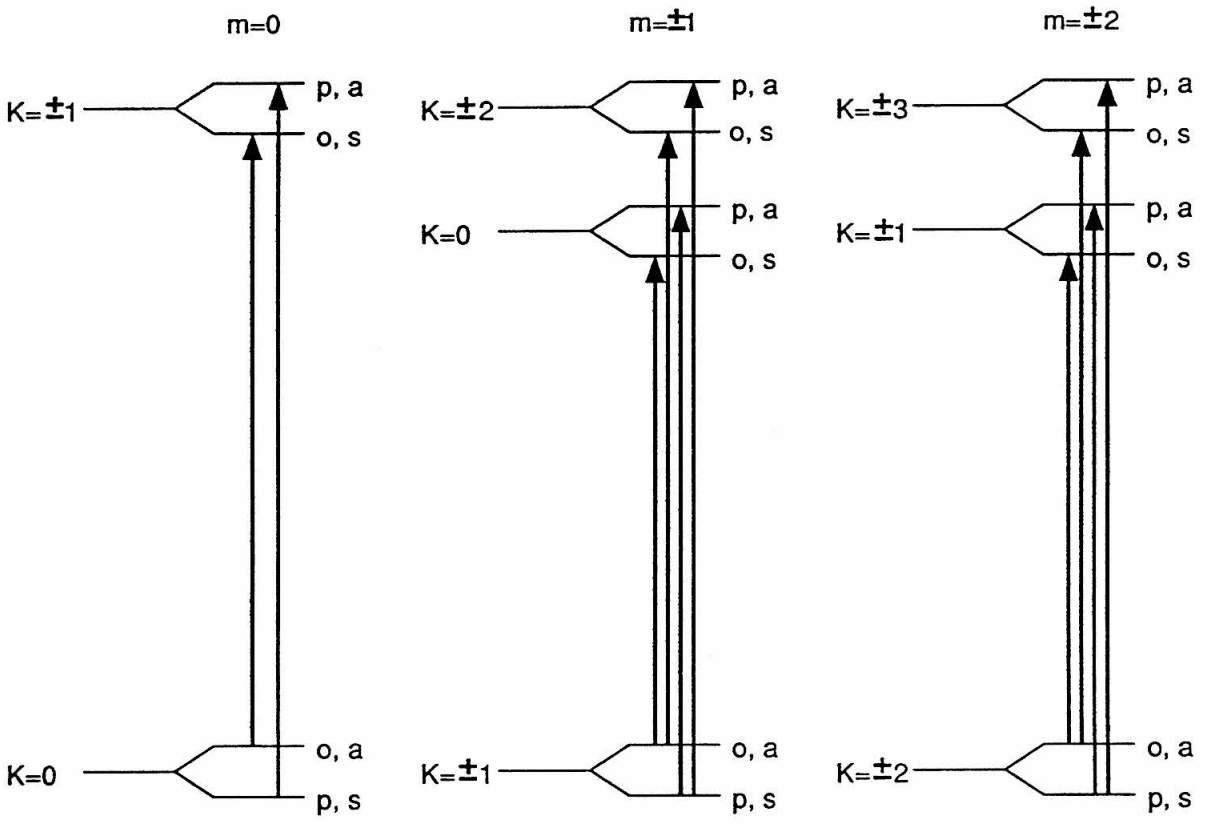

Figure 4.7: Symmetry state pairing diagram for $H_3N\cdots H_2O$. The ortho and para water proton nuclear spin states are labeled with o or p. The symmetry of the water tunneling wavefunction is given by s or a for symmetric or antisymmetric. Note that the pairing of o/p with s/a is a function of both m and K.

The energy is calculated using the following internal rotor Hamiltonian

$$\hat{H} = -\frac{\hbar^2}{2I_{tunnel}}\left(\frac{d^2}{d\theta^2_{H_2O}}\right) + V(\theta_{H_2O}). \tag{4.19}$$

If the equilibrium structure is such that the C_3 axis of ammonia is at an angle to the a-axis of the complex, both NH_3 and H_2O must move during water tunneling. We can use a "gear ratio" to reduce the motion to one dimension by writing I_{tunnel}, the moment of inertia for the tunneling motion, as

$$I_{tunnel} = I_c(H_2O) + \alpha I_b(NH_3), \tag{4.20}$$

where α = (angular displacement of ammonia/angular displacement of water) $\sim$ $(11.10°/63.22°) = 0.1756$. From this treatment, our estimated barrier height is 704 cm^{-1} and the fitted V_1 and V_2 are 4345 and -2411 cm^{-1}. The effective angles determined from $\langle\cos\theta\rangle$ and $\langle\cos^2\theta\rangle$ averaged over the one-dimensional wavefunctions are 62.2° and 60.5° . If we assume only water is moving in the tunneling process ($\alpha = 0°$), the barrier height is estimated at 840 cm^{-1}.

4.4 Summary

Microwave and far-infrared spectra of the $H_3N\cdots H_2O$ dimer were recorded from 36 to 86 GHz and 520 to 800 GHz with a planar supersonic jet/tunable laser sideband spectrometer. The a-type pure rotational microwave data extend the previous $m = 0, K = 0$ A symmetry manifold measurements of Herbine and Dyke [12] to higher frequency and also provide an additional set of microwave transitions in the $mK = +1$ E symmetry manifold. Two sets of five b-type rotation-tunneling bands, one set shifted from the other by an approximately constant 113 MHz, were observed in the far-infrared. The splitting into two sets arises from water tunneling, while the overall band structure is due to internal rotation of the ammonia top. Non-linear least-squares fits to an internal rotor Hamiltonian provided rotational constants, and an estimation of V_3=10.5 $\pm$5.0 cm^{-1} for the barrier height to internal rotation for

the NH_3 monomer. A non-linear *equilibrium* hydrogen bond is most consistent with the vibrationally averaged rotational constants; with the angle $\cos^{-1}[\langle\lambda_z\rangle]$ determined from $\langle\lambda_z\rangle$, the projection of the ammonia's angular momentum onto the framework. The water tunneling splitting and observed selection rules place constraints on the barrier height for proton exchange of the water as well as the most feasible water tunneling path along the intermolecular potential energy surface. An estimated barrier of 704 cm^{-1} was derived for the water tunneling motion about its *c*-axis.

Bibliography

[1] F.J. Lovas, R.D. Suenram, G.T. Fraser, C.W. Gillies, and J. Zozom. The Microwave Spectrum of Formamide-Water and Formamide-Methanol Complexes. *J. Chem. Phys.*, 88:722, 1988.

[2] D.A. Rodham, S. Suzuki, R.D. Suenram, F.J. Lovas, S. Dasgupta, W.A. Goddard, and G.A. Blake. Hydrogen-bonding in the Benzene Ammonia Dimer. *Nature*, 362:735, 1993.

[3] D.D. Nelson, Jr., G.T. Fraser, and W. Klemperer. Does Ammonia Hydrogen Bond? *Science*, 42:2563, 1965. The case of ammonia dimer might also be an exception; see the next sequential reference.

[4] R.M. Baum. Structure of Ammonia Dimer Sparks Debate among Physical Chemists. *Chem. and Eng. News*, October, 19:20, 1992.

[5] S.L. Miller. *Physics and Chemistry of Ice.* Royal Society of Canada, Ottawa, 1973.

[6] K. Ellsworth and G. Schubert. Saturn's Icy Satellites—Thermal and Structural Models. *Icarus*, 54:490, 1983.

[7] J.I. Lunine and D.J. Stevenson. Thermodynamics of Clathrate Hydrate at Low and High Pressures With Application to the Outer Solar System. *Astrophys. J. Supp.*, 58:493, 1985.

[8] J.E. Bertie and M.R. Shehata. Ammonia Dihydrate—Preparation, X-ray-Powder Diffraction Pattern and Infrared-Spectrum of $NH_3 \cdot H_2O$ at 100 K. *J. Chem. Phys.*, 81:27, 1984.

[9] F.A. Cotton and G. Wilkinson. *Advanced Inorganic Chemistry.* John Wiley and Sons, New York, 5th edition, 1988.

[10] P.R. Bunker. *Molecular Symmetry and Spectroscopy.* Academic Press, New York, 1979.

[11] N. Ohashi and J.T. Hougen. The Torsional Wagging Tunneling Problem and the Torsional Wagging Rotation Problem in Methylamine. *J. Mol. Spec.*, 121:474, 1987.

[12] P. Herbine and T.R. Dyke. Rotational Spectra and Structure of the Ammonia-Water Complex. *J. Chem. Phys.*, 83:3768, 1985.

[13] P. Herbine, T.A. Hu, G. Johnson, and T.R. Dyke. The Structure of $NH_3 \cdot H_2S$ and Free Internal Rotation Effects. *J. Chem. Phys.*, 93:5485, 1990.

[14] B. Nelander and L. Nord. Complex between Water and Ammonia. *J. Phys. Chem.*, 86:4375, 1982.

[15] A. Engdahl and B. Nelander. The Intramolecular Vibrations of the Ammonia Water Complex. A Matrix Isolation Study. *J. Chem. Phys.*, 91:6604, 1989.

[16] G.A. Yeo and T.A. Ford. The Matrix Isolation Infrared Spectrum of the Water-Ammonia Complex. *Spectr. Acta*, 47:485, 1991.

[17] Z. Latajka and S. Scheiner. Basis Sets for Molecular Interactions. 2. Application to H_3N—HF, H_3N—HOH, H_2O—HF, $(NH_3)_2$, and H_3CH—OH_2. *J. Comp. Chem.*, 8:674, 1987.

[18] W. Rijks and P.E.S. Wormer. Correlated van der Waals Coefficients. II. Dimers Consisting of CO, HF, H_2O, and NH_3. *J. Chem. Phys.*, 90:6507, 1989.

[19] E.C. Vauthier, V. Barone, and S. Fliszár. Xα Local Spin Density Calculations of the 1:1 Hydrogen-Bonded Complexes Formed by Water, Ammonia, and Hydrogen Fluoride. *Can. J. Chem.*, 68:1233, 1990.

[20] K.A. Olszewski, M. Gutowski, and L. Piela. Interpretation of the Hydrogen-Bond Energy at the Hartree-Fock Level for Pairs of the HF, H_2O, and NH_3 Molecules. *J. Phys. Chem.*, 94:5710, 1990.

[21] C.E. Dykstra and L. Andrews. Structures, Stabilities, and Intermolecular Vibrational Frequencies of Small Ammonia Complexes by Molecular Mechanics for Clusters Analysis. *J. Chem. Phys.*, 92:6043, 1990.

[22] G.A. Yeo and T.A. Ford. *Ab Initio* Molecular Orbital Calculation of the Infrared Spectra of Hydrogen Bonded Complexes of Water, Ammonia, and Hydroxylamine. Part 6. The Infrared Spectrum of the Water-Ammonia Complex. *Can. J. Chem.*, 69:632, 1991.

[23] Z. Latajka and S. Scheiner. Structure, Energetics, and Vibrational Spectrum of $H_3N \cdots HOH$. *J. Phys. Chem.*, 94:217, 1990.

[24] J.T. Hougen. A Generalized Internal Axis Method for High Barrier Tunneling Problems, as Applied to the Water Dimer. *J. Mol. Spec*, 114:395, 1985.

[25] L.H. Coudert and J.T. Hougen. Tunneling Splittings in the Water Dimer—Further Development of the Theory. *J. Mol. Spec.*, 130:86, 1988.

[26] B.L. Crawford. The Partition Function and Energy Levels of Molecules with Internal Torsional Motions. *J. Chem. Phys.*, 8:273, 1940.

[27] P.H. Turner, M.J. Corkill, and A.P. Cox. Microwave Spectra and Structure of *cis-* and *trans*-Methyl Nitrite. Methyl Barrier in *trans*-Methyl Nitrite. *J. Phys. Chem.*, 42:2563, 1965.

[28] J.K.G. Watson. *Vibrational Spectra and Structures*, volume 6. Elsevier Science, New York, 1977.

[29] R.H. Schwendeman. *Critical Evaluation of Chemical and Physical Structural Information.* National Academy of Sciences, Washington, D.C., 1972.

[30] M.D. Harmony, V.W. Laurie, R.L Kuczkowski, R.H. Schwendeman, D.A. Ramsay, F.J. Lovas, W.J. Lafferty, and A.G. Maki. Molecular Structure of Gas-Phase Polyatomic Molecules Determined by Spectroscopic Methods. *J. Phys. Chem. Ref. Data*, 8:619, 1979.

Chapter 5 Rotation-Tunneling Spectroscopy and Results for Methanol-Water Dimer

5.1 Introduction

5.1.1 Motivation

The last water-containing, hydrogen-bonded complex studied in this thesis is the methanol-water dimer. As with $H_3N\cdots H_2O$, this is a polyatomic$\cdots$polyatomic complex possessing a full six degrees of intermolecular freedom. It has a strong dipole-dipole interaction, 16.2×10^{-31} C^2m^{-1}, which again places it among some of the strongest vdW electrostatic potentials. This dimer also probes the interactions of two fundamental chemical units that occur naturally together as azeotropic mixtures and are often used together as the supporting liquid phase in reactive and non-reactive chemistry. In fact, the methanol-water system is an example of a solvent system which is miscible in all proportions, which makes it useful for liquid chromotography and other solvent-based separation techniques. But this system also elevates the level of study to include molecules with multiple functional groups. With both a hydrophilic hydroxyl group and a hydrophobic methyl group, the IPS for the methanol-water complex should be the most anisotropic one of the series discussed here. In addition, the methanol-water dimer will provide a test of the adaptability of pair-pair IPSs of simpler complexes to larger, multifunctional interactions. Some of these solution and chemical issues are addressed below.

Mixed solvent systems are inherently more difficult to model than single component ones, and increase the types and complexity of possible solvent-solute and solvent-solvent interactions. This is especially easy to envision for the methanol-water system, where methanol has the propensity to accept two hydrogen bonds but donate only one, breaking the high order of symmetry shown in Figure 1.1a for the

near T_d symmetry ice lattice. Moreover, even though a solvent system like methanol-water is completely miscible in all proportions, the solution resulting from the mixing of the two liquids is not necessarily homogeneous. Using statistical mechanics methods, Matsumoto and coworkers simulated the bulk structure of different mixtures of methanol and water [1]. Not surprisingly, the hydrodrophobic methyl groups caused the methanol to prefer surface and near-surface sites, and the interactions were strong enough to create a net alignment of methanol molecules in these enriched surface regions. The effect is particularly dramatic for low molar volume of methanol solutions which are shown to have most of the methanol pooling in these near-surface volumes. The picture of non-homogeneous mixing is reinforced by kinetic studies which show that the free energy of mixing of methanol and water is driven by excess entropy, not excess enthalpy [2]. This difference in solution dynamics between methanol and water on a macroscopic *vs.* microscopic level has led researchers to describe methanol alternately as a soluble hydrocarbon and as an alkylated water. As we saw in Table 1.1, which lists the solubilities of n-alcohols, the addition of a single methylene group can have a large effect on solubility. Such a dual nature stems from the bifunctionality of methanol and the very different interactions that water has with each portion of the molecule.

By far the most studied polyatomic$\cdots$polyatomic vdW complex, both computationally and experimentally, is the water-water dimer. The methanol-water dimer provides a heteromolecular analog to this well-studied system, not only to the IPS developed for this complex but also to the PI and VRT formalism developed especially for this dimer. Of course, methanol is chemically much different from water, but the dynamics of the unsubstituted position, whether it turns out to be donor or acceptor, should be largely conserved if the present IPS and formalism for water-water dimer is correct and adaptable to other hydroxyl-hydroxyl interactions. The methanol-water complex also provides the opportunity to synthesize an IPS from two other previously determined IPSs without the perturbing effects of three-body forces encountered in previous attempts. For example, Elrod and coworkers have studied the $Ar_2\cdots DCl$ complex to determine the additivity of two-body IPSs to give the

IPS for this vdW trimer [3]. They have found that three-body forces contribute a very significant 8% to the overall energetics of the complex. This complication should be avoidable for synthesizing the IPS of methanol-water from the water-water and methane-water potentials. Studies of water-water, documented in Section 1.3, and methane-water, investigated experimentally by Dore and coworkers [8], provide the basis for such a comparison during the ongoing research of all three of these complexes. While three-body and larger-body contributions to IPSs are definitely the rule and not the exception in the study of solution dynamics, the approach outlined above for the methanol-water dimer has applicability in the modeling of large biomolecular interactions, such as protein folding. Here, the complexity of the system derives not from a myriad of small solvent molecule interactions, which can be varied in an infinite number of permutations, but rather one long backbone which gives the polyfunctional sidegroups of the protein a high degree of order. Some protein folding approaches already use a matrix of dimeric, albeit crude, IPSs to form intramolecular potentials. The methanol-water dimer will be a good test of this method and will also provide refined potentials for its application.

5.1.2 Structural frameworks

The role of hydrogen bond donor and hydrogen bond acceptor in the methanol-water complex has not been addressed yet in this chapter, and in fact determining this fundamental structural framework is a primary goal in this first high resolution study of the complex. Because hydroxyl groups are amphoteric with respect to hydrogen bonding, methanol and water have the same availability to donate and accept hydrogen bonds. Proton affinity (PA) and gas phase basicity (GPB) have been used by other researchers to determine the propensity for hydrogen bond donation and acceptance within vdW complexes. In the gas phase equilibrium established between two species, MH^+ and N,

$$MH^+ + N \rightleftharpoons M + N^+, \tag{5.1}$$

PA is ΔG for the reaction and GPB is ΔH. The results for the comparison of methanol and water show equivalent differences in these values— PA(CH_3OH) - PA(H_2O) = 15 kcal/mol and GPB(CH_3OH) - GPB(H_2O) = 15 kcal/mol —indicating little entropic differences between the two forms of the complex [5]. More important, though, is the decided enthalpic preference for water:donor::methanol:acceptor roles with the complex. This confirms a simple Lowry-Brønsted picture of hydrogen bond donor and acceptor roles. In spite of this, both previous experimental and computational results have been mixed as to which conformer is the global minimum, and are discussed in more detail in the next section.

For the sake of clarity and brevity, the two forms are represented as follows: the order of roles is specified as donor$\cdots$acceptor (D$\cdots$A) and methanol and water are abbreviated as M and W, so that the methanol donor-water acceptor complex $CH_3OH\cdots OH_2$ becomes M$\cdots$W, and the water donor-methanol acceptor complex $CH_3O(H)\cdots H_2O$ becomes W$\cdots$M. The M$\cdots$W and W$\cdots$M designations will only be used when discussing structural details, and the more generic methanol-water will be used otherwise. When referring to isotopomers, the notation $CH_3OH\cdots H_2O$ and so on will be used without regard to proton donor/acceptor roles.

Figure 5.1ab depicts the two donor-acceptor complexes. Notice that the M$\cdots$W structure has a C_s plane of symmetry, while the W$\cdots$M structure has no point group symmetry elements other than the identity. Because these structures are more complex than the ones previously examined in this work, and in particular because their Euler angles do not coincide with likely normal mode coordinates, the R_{cm},θ, ϕ, and χ coordinates applied to Ar$\cdots H_2O$, $N_2\cdots H_2O$, OC$\cdots H_2O$, and $H_3N\cdots H_2O$ are not appropriate. Specific details of structural coordinates are addressed in Section 5.3.3.

Although *a priori* the structure for the methanol-water complex is not known, the M$\cdots$W and W$\cdots$M structures do have a number of commonalities that allow some prediction of the major features of the MW spectra. First of all, the complex is asymmetric, meaning that the asymmetry-split K degeneracies will be resolvable in the spectra. Also, the complex should have significant dipole moments along the a- and b-axes of the complex. A W$\cdots$M structure will have a small c-component as

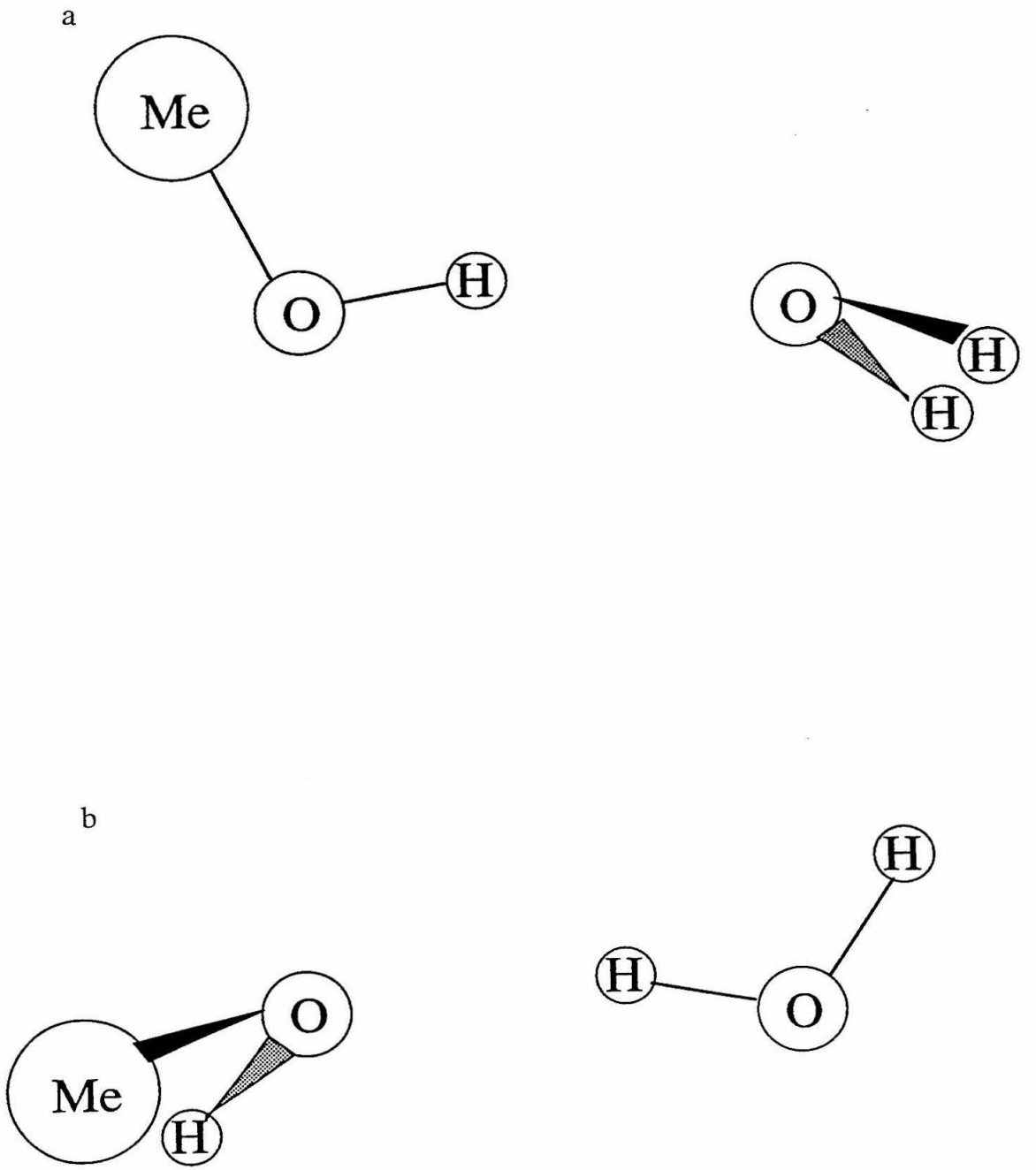

Figure 5.1: Structural frameworks for a) M···W and b) W···M.

well; the c-component for M···W should be zero by symmetry. Coupled with the fact that the A rotational constant is between 20 and 35 GHz, both a-type and b-type transitions should be observable in the MW. We can also anticipate complicated internal rotor effects from the methyl top, which in this instance will have significant projections along the a-, b-, and in the case of W···M, c-axes. This time, the internal rotation is formally an intramolecular mode, and the V_3 barrier should be much larger than that for NH_3 in $H_3N\cdots H_2O$.

5.1.3 Tunneling frameworks

The two different structural frameworks for the methanol-water complex each generate a set of unique tunneling frameworks. As before, we need to consider sets of equivalent nuclei and their exchange pathways. In each structure, the methyl group has three equivalent hydrogens which can interchange about the C_3 axis of the group. This motion leads to A and E symmetry states, analogous to those seen for the NH_3 internal rotation in $H_3N\cdots H_2O$. Each H_2O subunit has two hydrogens which can exchange about the water C_2 axis and, in the case of W···M, about the water c-axis. Also exchangeable are the two oxygen lone pair binding sites on each *acceptor* oxygen atom. Note, the entity which is exchangeable is the binding site, not the electrons which occupy the lone pair orbitals. We can think of the acceptor oxygen atom as a potentially chiral center: in the case of M···W, the oxygen is not chiral because the two hydrogens are equivalent; in W···M, however, the oxygen is chiral with four different substituents—H, CH_3, $\cdots H_2O$, and an unbound lone pair—arrayed in a near tetrahedral geometry. Hence, the chirality of the hydrogen-bonded oxygen doubles the number of nonsuperimposable frameworks for W···M. Figures 5.2 and 5.3 show the sets of tunneling frameworks for M···W and W···M.

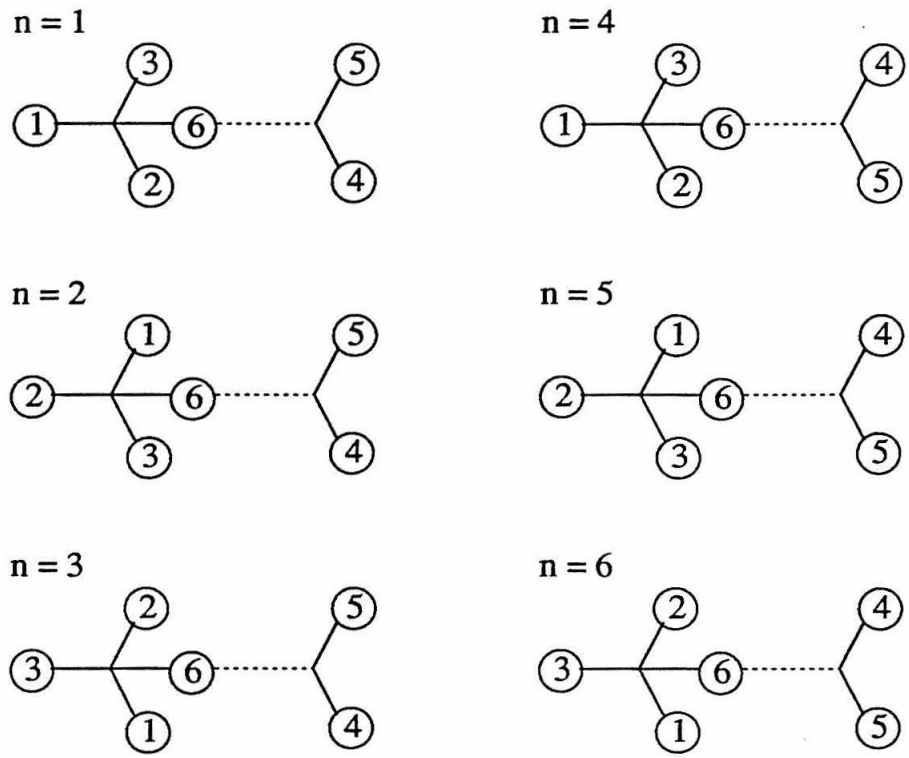

Figure 5.2: Tunneling frameworks for M···W. Hydrogens 1,2, and 3 are on methyl group; 4 and 5 are on the water; and 6 is the hydroxyl hydrogen of methanol.

Figure 5.3: Tunneling frameworks for W···M, next page.

n = 1

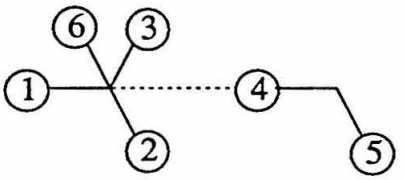

n = 2

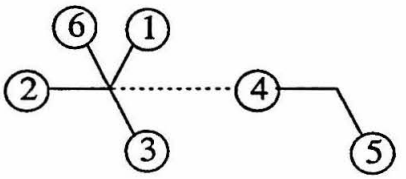

n = 3

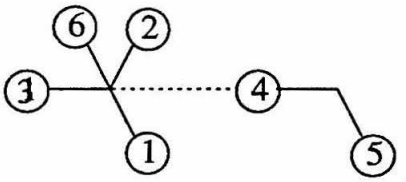

n = 4

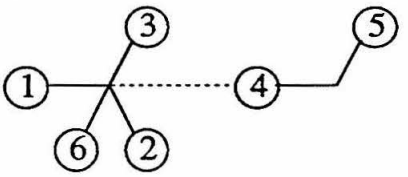

n = 5

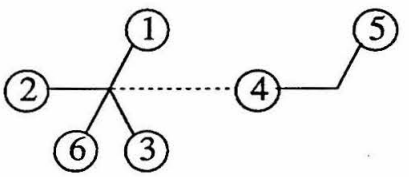

n = 6

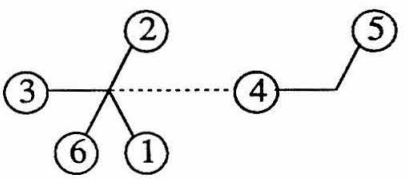

n = 7

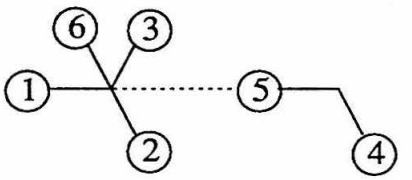

n = 8

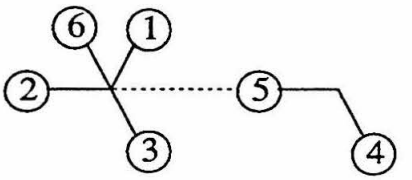

n = 9

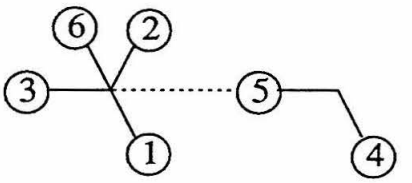

n = 10

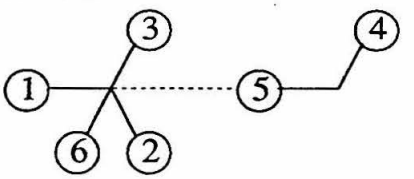

n = 11

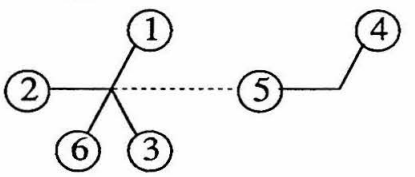

n = 12

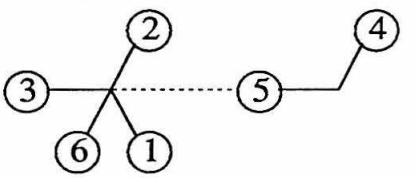

Hougen and Ohashi have made a detailed PI theory investigation of the methanol-water dimer in the $K = 0$ rotational manifold, and their work is helpful in interpreting the MW spectra of this complex and determining its structure [6]. They begin by evaluating the feasibility for each of the tunneling paths ($1 \rightarrow n$) in the two different conformers, based on previous spectroscopic results for other vdW complexes. For M$\cdots$W, they guess that the water C_3 tunneling ($1 \rightarrow 4$) has a splitting of $\sim$3 cm^{-1}, and estimate that the methyl torsion ($1 \rightarrow 2,3$) is $\sim$0.06 cm^{-1}; the combination modes are deemed unfeasible. The considerations for W$\cdots$M, with twice as many possible tunneling pathways, are substantially more complex, with all feasible tunneling splittings having similar estimated values of 0.04–0.09 cm^{-1}. Those deemed feasible are the methyl torsion ($1 \rightarrow 2,3$), exchange of lone pairs on the acceptor ($1 \rightarrow 4$), exchange of donor protons ($1 \rightarrow 7$), and simultaneous exchange of both acceptor lone pairs and donor protons ($1 \rightarrow 10$). Hougen and Ohashi then proceed to develop a flexible coordinate system in which all of these motions can be parameterized to derive the matrix elements for tunneling splittings and the selection rules for a-type spectra. The two feasible tunneling motions of M$\cdots$W split rotational levels into four states. In W$\cdots$M, the methyl torsion gives one set of splittings. The group of acceptor lone pair ($1 \rightarrow 4$), donor proton ($1 \rightarrow 7$), and combination ($1 \rightarrow 10$) modes are analogous to the tunneling pathways in $N_2 \cdots H_2O$, in that the three pathways represent only two unique tunneling modes. Hougen and Ohashi reckon that the dominant pathway is the donor proton tunneling, and the other two combine into a superpostion of splittings $H_{1,4} \pm H_{1,10}$. These rotational-tunneling manifolds are reproduced in Figure 5.4ab, along with the derived selection rules. These rules predict "top-to-top, bottom-to-bottom" for the a-type spectra, which means that the tunneling splittings will not be easily measurable using the lowest frequency a-type MW data. They also predict a total of four rotation-tunneling components for M$\cdots$W, and eight for W$\cdots$M.

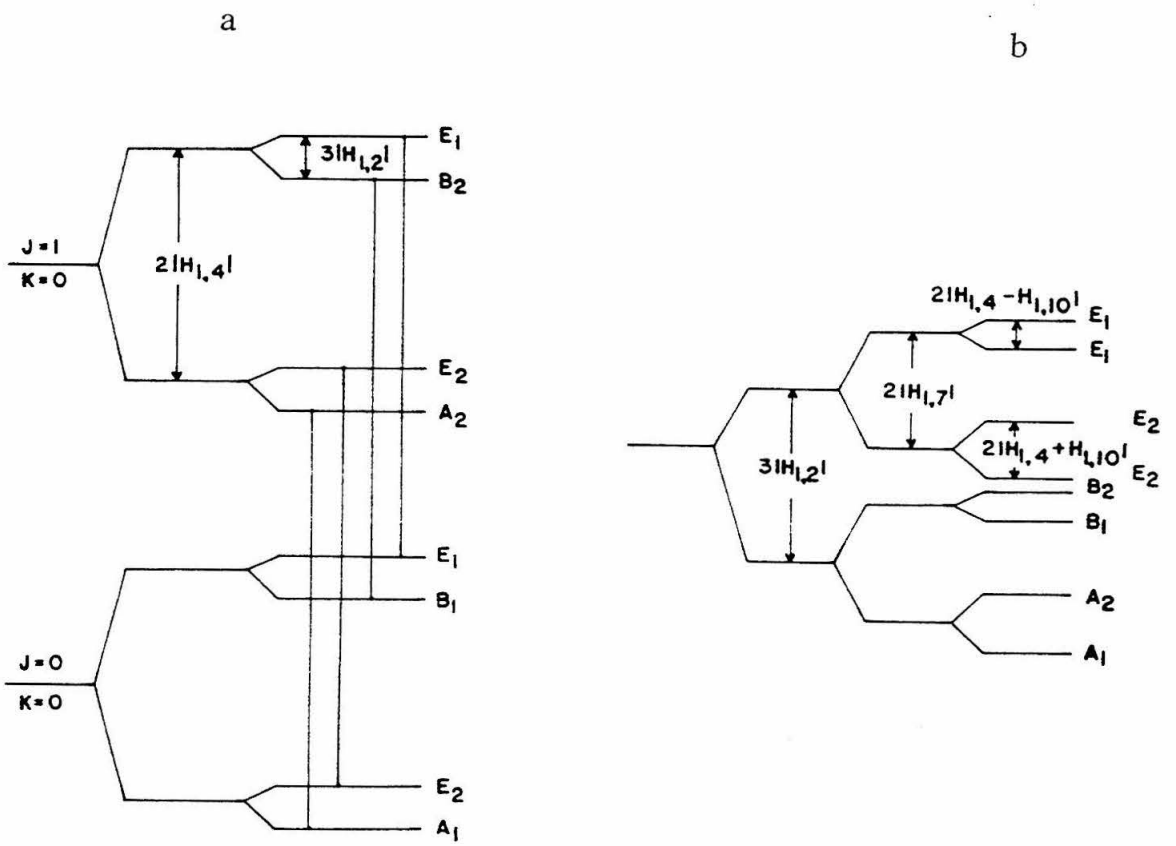

Figure 5.4: Rotational-tunneling manifolds for a) M···W, and b) W···M, from Hougen and Ohashi.

5.2 Previous experimental and computational work

Past researchers have conducted numerous experiments and computations on the interaction of methanol and water, but the large majority of these studies, like the few cited above, probe only the bulk solution. The MW experiments described in this chapter focus on the subtle interplay of donor and acceptor roles in amphoteric methanol and water, information which averaging obscures in the the bulk studies. For this reason, only those studies which treated discrete methanol-water dimer complexes are addressed.

5.2.1 Experimental work

The paucity of experimental work with the methanol-water complex is somewhat surprising, considering the ease with which they are formed from two volatile, relatively unreactive, and commonly available liquids. However, with only 9 atoms, the complex already possesses 15 intramolecular modes and the full 6 intermolecular ones, making vibrational spectroscopy complicated. Moreover, the rotational-torsional spectroscopy of methanol itself is highly affected by angluar momentum coupling and is still the subject of experimental and theoretical treatments [7].

Notwithstanding these challenges, several researchers have presented reasonable interpretations of vibrational spectra for isolated methanol-water complexes. Bakkas and coworkers first isolated the complex in a nitrogen matrix and observed the spectral changes for all 3 intramolecular water modes and 10 out of 12 modes for methanol using an FTIR spectrometer [8]. By measuring a distinctive red shift for the methanol O—H and a corresponding blue shift of the C—O stretch, they concluded that the complex was M···W. *Ab initio* calculations performed by the authors at the MP2 6-31G** level with harmonic frequency approximations confirmed the basic spectral shifting pattern from the experiments. When the authors followed this work with a similar matrix isolation experiment in argon, the results were completely different,

with spectral shifts in argon supporting a W···M structure [9]. In neither experiment was evidence of the second conformer found. This matrix effect is particularly remarkable when considered in the light of the authors' *ab initio* computations which showed that the conformers differed in binding energy by a mere 0.084 kcal/mol. However, this computational result is questionable, considering the sizable difference in PA and GPB for methanol and water, and in fact, more comprehensive *ab initio* studies by Kim, Jhon, and Scheraga, cited below, offer a more reasonable difference of $\sim$ 1.0 kcal/mol [10]. If one assumes that this estimate is closer to the truth, the matrix effect of the two Bakkas *et al.* reports can be ascribed to a strong, and interesting, methanol-water-nitrogen three-body interaction.

Isolated methanol-water dimer complexes have also been identified in a molecular beam by Huisken and Stemmler using an IR dissociation/depletion probe coupled with a time-of-flight mass spectrometer [11]. The probe used is a line-tunable CO_2 laser acting on the C—O stretch chromophore, and individual cluster sizes were resolved by scattering off of a perpendicular beam of He atoms. In previous experiments with methanol dimer, they were able to observe two separate peaks, one to the red and one to the blue of C—O fundamental at 1033.9 cm^{-1}, and assigned them to the donor and acceptor subunits, respectively. By analogy, they only observed a red shifted C—O stretch for the methanol-water complex at 1027.8 cm^{-1}, in good agreement with the Ar-matrix isolation frequency of 1031.7 cm^{-1}. Thus, in the only gas-phase experiment before the present MW work, evidence was found only for the W···M conformer.

5.2.2 Computational work

Five computational studies of the methanol-water complex have been performed, and the results for the binding energy of both M···W and W···M minima are summarized in Table 5.1 [12, 13, 14, 10, 8]. Taken as whole, they fall 3:2 in favor of the M···W global minimum and there are results which find the minima separated by $\sim$ 1 kcal/mol for both conclusions. It is enough to make one summarily discount all *ab initio* efforts for vdW clusters. However, as Hougen and Ohashi point out,

Table 5.1: Summary of *ab initio* results for methanol-water dimer. Binding energies are D_e in kcal/mol.

Authors	M···W	W···M
Del Bene	6.26	5.22
Bolis *et al.*	7.5	7.0
Tse, Newton, and Allen	5.55	5.73
Bakkas *et al.*	5.517	5.433
Kim, Jhon, and Scheraga	6.74	7.78

the findings of the studies are correlated with basis set size, with the larger bases determining that the W···M structure is more stable. Moreover, none of these computational studies explored basis set expansion or performed BSSE corrections, both of which have been shown to greatly affect the results for vdW clusters. Remember that when these techniques were employed for $N_2\cdots H_2O$ and $OC\cdots H_2O$, the surfaces generated corresponded well with experimental results. The lesson here is that experiments are still needed to confirm *ab initio* results (or predate them) at this level of detail.

5.3 MW observation of methanol-water spectra

5.3.1 Observed data and experimental conditions

Measurements of the MW spectrum of $CH_3OH\cdots H_2O$ were begun independently and nearly concurrently at Caltech and at NIST, Gaithersburg in the Molecular Physics division. The NIST work stemmed from an on-going effort to measure the spectrum of methanol dimer. Because the MW spectrometers at the two locations are complimentary in several ways, including spectral coverage, we decided to collaborate on this project after learning early into the work about each others' initial results.

The advantages of each instrument for this work are as follows. The NIST Balle-Flygare type FTMW spectrometer, described in Section 2.8, is a high resolution instrument, $\Delta\nu \approx 2$ kHz, capable of measuring many of the small tunneling splittings associated with more strongly bound vdW complexes, and can record them with

accurate relative intensities. The instrument is also equipped with a high voltage Stark cell, ± 5 kV over 26 cm, that can measure the dipole moment of complexes with high precision. Its limitations are that it has a slow scanning rate, making first order Stark transitions difficult to track and limiting the amount of data collected. The FT cavity can also scan only from 7 GHz to about 22 GHz, and even then, the cavity must be manually adjusted to switch between sub-ranges within that 15 GHz. On the otherhand, the Caltech MW spectrometer, described in Section 2.3, begins coverage at about 18 GHz and can reach up to 80 GHz. This machine has a much lower resolution of a few hundred kHz, but can scan quickly, up to 20 MHz/min or 1.2 GHz/hour, allowing a broad, automated collection of data. The MW spectrometer is also equipped with a low voltage Stark cell, used in these experiments primarily to discriminate between A and E methyl rotor states [12].

A total of 73 transitions between 21.9 and 55.6 GHz were recorded at Caltech for the $CH_3OH\cdots H_2O$ isotopomer which required both methanol and water (Figure 5.5a). Initial efforts at scanning were slowed due to the much more numerous methanol dimer lines. The methanol dimer complex has 16 tunneling transitions which, along with transitions from different populated K_a manifolds, obscured hundreds of MHz of spectral coverage, and required a large amount of time to distinguish from the more sparse methanol-water lines. Later on, approximate rotational constants for the methanol dimer from NIST allowed us to selectively avoid these congested areas. At the same time, 8 transitions corresponding to a methanol + water chemistry were recorded at NIST: 2 between 7.7 and 8.0 GHz and 6 between 15.4 and 16.5 GHz. Some tunneling splittings on the order of tens of kHz were observed in the NIST spectra. Once some of these $CH_3OH\cdots H_2O$ transitions were fit to an asymmetric rotor Hamiltonian, transitions from other isotopomers were predicted, and therefore preassigned, from a crude W$\cdots$M structure and observed. These included 3 NIST and 17 Caltech lines for $CH_3OD\cdots D_2O$, 5 NIST lines each for $CD_3OH\cdots H_2O$ and $CH_3OH\cdots DOH$, and 6 NIST lines for $^{13}CH_3OH\cdots H_2O$. The Caltech data corresponds to transitions in J from $J = 2$ up to $J = 6$ or 7 in the $K_a = 0, 1, 2$ manifolds; NIST lines were from $J = 0, K_a = 0$ and $J = 1, K = 0, 1$. The NIST work also measured

the following dipole moment components: $\mu_a = 2.385 \pm 0.008$ D, $\mu_b = 1.090 \pm 0.006$ D, and $\mu_c = 0.13 \pm 0.14$ D.

The lines at Caltech were observed with a flow rate of 3.60 slm Ar/6.00 slm Ar + H_2O/0.270 slm Ar + CH_3OH. In the NIST experiments, CH_3OH and H_2O, entrained in separate flows of Ar, were introduced into the cavity through a 0.5 mm diameter pulsed solenoid valve over 200-400 μs durations at rates up to 35 Hz. The total backing pressure in the Caltech experiment was $\sim$ 2 atm and for the NIST experiment it was 1 atm. No special attention was given to the purity of the CH_3OH or H_2O used; deuterated liquids were obtained from Cambridge Isotope Laboratories.

5.3.2 Data assignment and fitting

The initial assignments were greatly facilitated by the much simpler rotational structure in the low quantum number NIST data. Only two lines for $CH_3OH\cdots H_2O$ were observed in the $J = 0 \rightarrow 1$ region, and these were separated by $\sim$ 200 MHz. Stark measurements indicated that the lower frequency transition had a first order Stark effect, while the higher frequency transition had only a second order Stark effect. As seen earlier with $H_3N\cdots H_2O$, internal rotation of three-fold rotors leads to an A symmetry state and a doubly degenerate E symmetry state. The degeneracy of the E state supports the first order Stark effect. Assignments based upon the higher frequency of the two led to a set of lines which could be fit to a standard asymmetric rotor Hamiltonian, Equation (3.2), including transitions with $J = 0$ to 7 and $K_a = 0, 1, 2$. These assigned spectra are seen in Figure 5.5b; Table 5.2 contains the line list with observed and calculated frequencies as well as a complimentary set of A symmetry state data for the $CH_3OD\cdots D_2O$ isotopomer. Table 5.3 lists the transitions of the smaller data sets from NIST for $CD_3OH\cdots H_2O$, $CH_3OH\cdots DOH$, and $^{13}CH_3OH\cdots H_2O$. Tables 5.4 and 5.5 give the corresponding fitted spectroscopic constants for these complexes; because of the limited data set for the last three complexes, the A rotational constant was not well determined, and fixed at an estimated value for the final fit of the data.

Assignment and fitting of the E state data are not so straightforward, and cur-

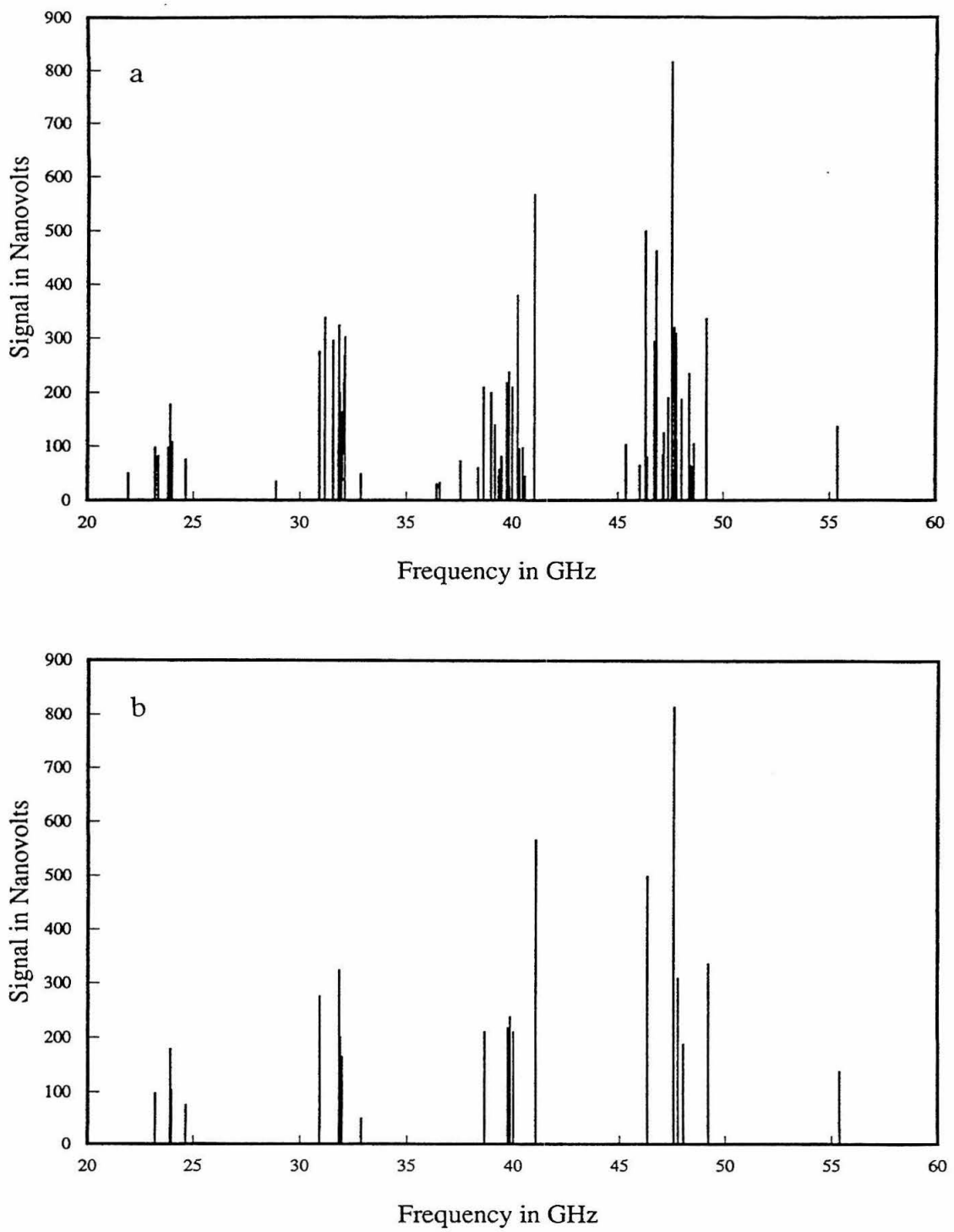

Figure 5.5: a) observed and b) assigned A state MW transitions for the $CH_3OH\cdots H_2O$ complex.

Table 5.2: A-state rotational transtions (MHz) for $CH_3OH\cdots H_2O$ and $CH_3OD\cdots D_2O$.

Transition	$CH_3OH\cdots H_2O$	$CH_3OD\cdots D_2O$
$1_{01} - 0_{00}$	7978.595	
$2_{12} - 1_{11}$	15470.231	14339.873
$2_{02} - 1_{01}$	15948.776	14754.546
$2_{11} - 1_{10}$	16440.191	15158.690
$3_{13} - 2_{12}$	23199.52	21504.37
$3_{03} - 2_{02}$	23903.12	22114.40
$3_{22} - 2_{21}$	23924.74	
$3_{21} - 2_{20}$	23953.78	
$3_{12} - 2_{11}$	24652.00	22730.18
$4_{14} - 3_{13}$	30919.68	28662.01
$4_{04} - 3_{03}$	31831.28	29453.22
$4_{23} - 3_{22}$	31888.30	
$4_{22} - 3_{21}$	31960.68	
$4_{13} - 3_{12}$	32855.04	30291.31
$5_{15} - 4_{14}$	38629.84	35811.19
$5_{05} - 4_{04}$	39726.96	36763.99
$5_{24} - 4_{23}$	39842.34	
$5_{23} - 4_{22}$	39986.38	
$5_{14} - 4_{13}$	41043.15	37838.34
$6_{16} - 5_{15}$	46326.26	42949.62
$6_{06} - 5_{05}$	47581.19	44040.89
$6_{25} - 5_{24}$	47784.42	
$6_{24} - 5_{23}$	48034.79	
$6_{15} - 5_{14}$	49215.09	45366.95
$7_{17} - 6_{16}$		50078.70
$7_{07} - 6_{06}$	55388.85	51277.76
$7_{16} - 6_{15}$		52870.37
$8_{18} - 7_{17}$		57187.88
$8_{08} - 7_{07}$		58472.93

Table 5.3: A-state rotational transtions (MHz) for $CD_3OH\cdots H_2O$, $CH_3OH\cdots$ DOH, and $^{13}CH_3OH\cdots H_2O$.

Transition	$CD_3OH\cdots H_2O$	$CH_3OH\cdots$ DOH	$^{13}CH_3OH\cdots H_2O$
$1_{01} - 0_{00}$	7384.830	7905.251	7840.351
$2_{12} - 1_{11}$	14312.672	15334.694	15200.679
$2_{02} - 1_{01}$	14760.490	15802.445	15672.362
$2_{11} - 1_{10}$	15214.723	16282.568	16157.644
$3_{13} - 2_{12}$			22794.393
$3_{03} - 2_{02}$	22117.889	23683.567	23487.755

Table 5.4: Fitted spectroscopic parameters for methanol-water isotopomers.

	$CH_3OH\cdots H_2O$	$CH_3OD\cdots D_2O$
A (MHz)	28264(27)	25695(48)
B (MHz)	4232.17(7)	3895.601(8)
C (MHz)	3747.01(7)	3485.454(6)
Δ_J (kHz)	49.8(4)	57.6(5)
Δ_{JK} (kHz)	314(7)	2746(4)
δ_J (kHz)	10.7(6)	23.0(3)

Table 5.5: Fitted spectroscopic parameters for methanol-water isotopomers, continued. Values of A marked with an asterisk were fixed to structural approximations.

	$CD_3OH\cdots H_2O$	$CH_3OH\cdots$ DOH	$^{13}CH_3OH\cdots H_2O$
A (MHz)	23300*	28000*	28000*
B (MHz)	3917.017(2)	4189.903(3)	4159.739(2)
C (MHz)	3468.056(2)	3715.525(3)	3680.816(2)
Δ_J (kHz)	61.1(1)	43.9(1)	50.3(1)
Δ_{JK} (kHz)	498(1)	205(2)	84.8(9)

Table 5.6: Tentative assignments for $CH_3OH\cdots H_2O$ E state rotational transitions.

Assignment	Frequency (MHz)
$1_{01} - 0_{00}$	7763.750
$2_{02} - 1_{01}$	15541.723
$3_{03} - 2_{02}$	23342.88
$4_{04} - 3_{03}$	31164.40
$5_{05} - 4_{04}$	39000.56
$6_{06} - 5_{05}$	46838.52
$3_{13} - 2_{12}$	23812.08
$4_{14} - 3_{13}$	31545.84
$5_{15} - 4_{14}$	39173.76
$6_{16} - 5_{15}$	46732.50
$3_{12} - 2_{11}$	24000.92
$4_{13} - 3_{12}$	32103.44
$5_{14} - 4_{13}$	40247.31
$6_{15} - 5_{14}$	48394.68

rent progress has given only a tenative assignment and no full asymmetric rotor fit. Evidence for the E state is most obvious in the NIST $J = 0 \rightarrow 1$ lines, where the lower frequency component has a first order Stark effect, consistent with an excited internal methyl rotor. A simple R-branch progression was found to be built upon this transition for $K_a = 0$. Assignment of the $K_a \neq 0$ E state components was complicated by the fact that the not-too-asymmetric top A symmetry state has nearly degenerate transitions for $K_a = 2$, which also have pseudo first order Stark effects at low values of J. After complete assignment of the A symmetry state data eliminated these as choices, two additional sets of E state lines were identified, each again fitting a separate R-branch progression. Stark shifts indicate that these two are characteristic of $K_a = 1$ states. The tenative assignments are given in Table 5.6. However, attempts at fitting more than one progression at a time to a standard internal rotor Hamiltonian were unsuccessful.

Several hydrogen-bonded methanol-containing complexes have been previously examined in the literature: $CH_3OH\cdots NH_2CHO$ [16], $CH_3OH\cdots CO$ [17], $(CH_3OH)_2$ [18], $CH_3OH\cdots Ar$ [19], and $CH_3O(H)\cdots HCl$ [20]. The first three have succeeded in using such an Hamiltonian in combined fits of A and E state data (and in the

case of $(CH_3OH)_2$, A, E, and G states.) For the last two, though, this approach has not yielded a combined fit. In the $CH_3OH\cdots Ar$ dimer, free rotation of the CH_3OH subunit, similar to that of H_2O in $Ar\cdots H_2O$, is suspected to couple to the overall rotation of the complex as well as the internal rotation; the E state spectra have yet to be solved for this complex. The results for the $CH_3O(H)\cdots HCl$ dimer are similar to the present situation for methanol-water dimer. Cope *et al.* found a series of A state transitions which were well fit to an asymmetric rotor Hamiltonian; a second R-branch progression was also observed to the red of the $K_a = 0$ lines. They ascribed this second set of lines to a low-lying vibrational state, and no Stark experiments are mentioned. Another similarity between those results and the present is the large change in $\bar{B} = (B + C)$: 67 MHz, or 1.43%, for $CH_3O(H)\cdots HCl$ and 215 MHz, or 2.69%, for $CH_3OH\cdots H_2O$ on the $J = 1 \rightarrow 2$, $K_a = 0$ transition. It is very possible that Cope *et al.* failed to find the other $K_a \neq 0$ components because they are far removed from the other lines, and in fact their low-lying vibrational state is most likely the E excited internal rotor state. They instead assigned the second state to the lone-pair interchange vibrational or tunneling state. This too is reasonable for both $CH_3O(H)\cdots HCl$ and $W\cdots M$ since the proton donors have such light reduced masses, compared with the other methanol complexes which do not exhibit this behavior. Taken together, the excited internal rotor motion coupled to the lone pair interchange is very similar to the combined $n = 1 \rightarrow 4$ and $n = 1 \rightarrow 10$ tunneling motions described by Ohashi and Hougen, and shown in Figure 5.3.

5.3.3 Structural analysis

As emphasized above, structure, especially the gross features which determine proton donor and acceptor roles, is of key importance in the MW study of this complex. The Euler-type angular coordinates, employed in the other analyses covered in this work, were not used in this structural analysis. As the subunits grow larger, these do not correspond well with logical intermolecular normal modes of the complex. Instead, the structure is parameterized in the internal coordinates developed by Thompson,

where each atom is specified by its orientation with respect to the last three atoms [21]. The coordinates consist of a bond length, a bond angle, and a torsional angle. Of course the first three atoms have a reduced number of coordinates. The structure fitting routine was again `STRFTQ`, written by Schwendeman and modified by Lovas [22], which allows multiple isotopomers to be fit simultaneously. There are several advantages to using the internal coordinate system in combination with this fitting routine. First, the number of parameters to be fit is reduced from similar programs using principal axis coordinates. Also, symmetry can be specified within a molecule. For example, if fitting the HCF angle in methyl fluoride, one could specify that all three hydrogen form the same HCF angle and that they be adjusted symmetrically during the fit. Finally, ghost atoms with zero mass can be used to simplify the inputted structure. For example, in methanol, the methyl group tilts 3.3° away from the hydroxyl group, meaning that the C_3 symmetry axis is not parallel with the C—O bond. The movement of all three methyl hydrogens can be accomodated in one parameter by first adding a ghost atom, bonded to the carbon atom, at the center of the triangle formed by the hydrogens; the hydrogens are then specified relative to the ghost atom.

The starting point for the fit, as well as the algorithm for the fit itself, contain some assumptions and are inherently subjective. Below are the assumptions and their justifications used in this structural analysis.

1. Assume ground state geometries for the monomer structures, as found in Harmony *et al.* [23].

2. Angle COH of methanol = 108.5° $\approx$ 109.5°, so assume starting geometry of C, H, *and* the two lone pairs about oxygen is tetrahedral.

3. Assume the intermolecular starting geometry of both complexes, M$\cdots$W and W$\cdots$M, are that of water-water dimer. For this geometry take that of Odutola and Dyke, structure I, since this has the lowest standard deviation and its low value of χ_a is consistent with assumption 2 [24]. See Figure 5.6.

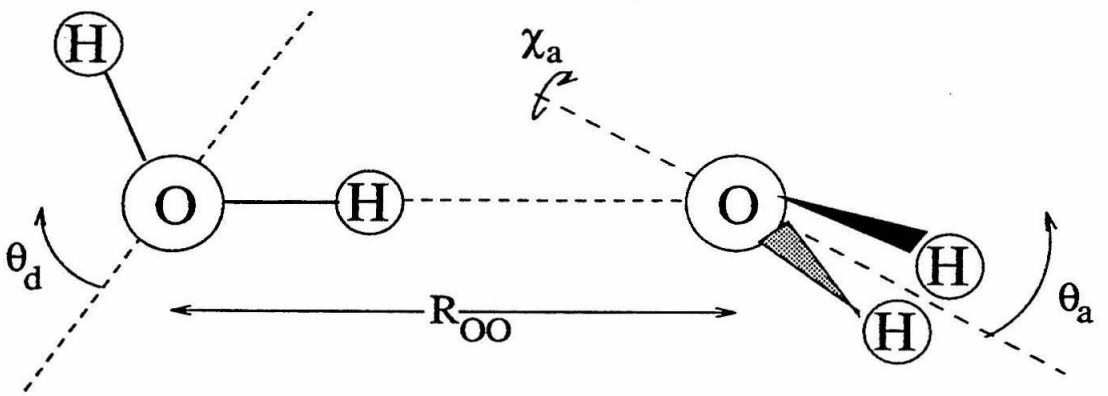

Figure 5.6: Odutola and Dyke water dimer structure I: $R_{OO} = 2.9768$ Å, $\theta_d = -53.0°$, $\theta_a = 59.7°$, and $\chi_a = 0.3°$.

4. Since we do not know *a priori* how the methyl group in CH_3OH affects the geometry of the lone pairs, use assumption 2 to determine θ_a for W···M, and use angle $O_1O_2H_5$ from W···M to fix angle $O_2O_1H_1$ in M···W (*i.e.*, 0.74°.)

A methanol geometry was first computed in internal coordinates, using the ghost atom as described above. Then the water subunits of the two different conformers were specified relative to the methanol geometry. The final so called Z-matrix for each conformer is given in Table 5.7.

A number of structural fits were run during the course of this work in order to obtain predictions for different isotopomers, and also to check preliminary findings for the donor/acceptor roles. In the fits, B and C rotational constants were used along with the well determined A rotational constants for $CH_3OH\cdots H_2O$ and $CH_3OD\cdots D_2O$. Three parameters were fit for the two different conformers: the hydrogen bond distance $R_{O\cdots H}$; the lone pair geometry of the acceptor oxygen, θ_O, to correct for the tetrahedral assumption; and the torsional angle of the water, ϕ_{H_2O}, about the hydrogen bond. These correspond to R_{OO} (less the O—H bond length, θ_a,

Table 5.7: Z-matrix coordinates for M···W and W···M.

Z-matrix coordinates for CH_3OH						
atom	atom#	connected to atom#	unit mass	r	α	β
H_1	1		1.			
O_1	2	1	16.	0.945		
C	3	2	12.	1.425	108.5	
G	4	3	0.	0.380	176.7	180
H_2	5	4	1.	1.026	90.0	0
H_3	6	4	1.	1.023	90.0	120
H_4	7	4	1.	1.023	90.0	-120
Z-matrix coordinates for M···W						
atom	atom#	connected to atom#	unit mass	r	α	β
O_2	8	1	16.	2.032	179.0	180
H_5	9	8	1.	0.972	122.0	-68.67
H_6	10	8	1.	0.972	122.0	68.67
Z-matrix coordinates for W···M						
atom	atom#	connected to atom#	unit mass	r	α	β
H_5	8	2	1.	2.005	109.0	120
O_2	9	8	16.	0.972	179.0	-60
H_6	10	9	1.	0.972	104.5	180

and χ_a in the water dimer structure.

All pairings of isotopomeric fits unanimously favored the the W···M conformer as measured by the residual error of the principal moments of inertia, giving definitive confirmation to the Ar matrix and IR photo-depletion experiments. The most conclusive example of the structural preference comes from the data for the $CH_3OH\cdots DOH$ isotopomer. Due to the similar positions of most of the atoms about the centers of mass for the two conformers, isotopic substitution produced small, but consistent, preferences for W···M. But the $CH_3OH\cdots DOH$ isotopomer substitutes singly the one atomic position most sensitive to the change in conformation—this D atom is either on the outside of the complex, > 2 Å from the center of mass in M···W, or it is on the inside (due to greater D-binding zero point energy) of complex, < 1 Å away from the center of mass. This is best shown in the following pair of fits. The other four isotopomers studied are fit to each conformer separately, with the residual of 0.243 amu Å^2 (units of inertia) for W···M, more than six times smaller than the 1.52 amu Å^2 for M···W. Even more conclusive is the prediction of rotational constants for the sensitive $CH_3OH\cdots DOH$ isotopomer. The error in $B + C$ is only 5.42 MHz for the W···M fit structure, while $B + C$ differ by 246.37 MHz for the M···W predictions.

The resulting structure is very similar to that of water dimer. The $R_{OO} = 2.997 \pm 0.009$ Å bond length is, surprisingly, longer, but only by 0.02 Å, than that for the water dimer, and the bond angle is nearly linear at $179 \pm 1°$. The torsional angle was not well fit, and on the average gave a structure close to bifurcation of the methanol COH angle, again much like water dimer.

5.3.4 Tunneling splittings

The PI theory, modified internal axis method, and estimates of Hougen and Ohashi predict four significant tunneling splittings for the M···W conformer and eight for W···M. The A-E splitting was very large, hundreds of MHz, and observable for all values of J and K measured. The NIST spectra also recorded a much smaller splitting, 30–100 kHz, for all A state lines of all isotopomers. This gives a total of only

four tunneling components, in seeming contradiction to the structural analysis results. However, these splittings were predicted to have "top-to-top, bottom-to-bottom" selection rules for a-type spectra, and so the effects of the splittings might not be apparent in the present data, as was the case for two of the tunneling components in the methanol dimer [18]. A search of up to 60 GHz, more than twice the structural value of A, turned up no identifiable b-type transitions. These spectra, which should have "top-to-bottom, bottom-to-top" selection rules, have a large dipole moment component, and should have many strong Q-branches. However, as we saw for $H_3N\cdots H_2O$in Equation (4.6), internal rotation can increase the frequency of the b-type ($\Delta K = \pm 1$) spectra to more than four times that predicted by structure alone.

5.4 Summary

Microwave spectra of $CH_3OH\cdots H_2O$ and $CH_3OD\cdots D_2O$ were recorded between 20 and 60 GHz, along with data from our collaborators at the National Institute for Science and Technology for $CH_3OH\cdots H_2O$, $^{13}CH_3OH\cdots H_2O$, $CH_3OH\cdots DOH$, $CD_3OH\cdots H_2O$, and $CH_3OD\cdots D_2O$ between 7 and 24 GHz. Because CH_3OH and H_2O are both capable of accepting and donating hydrogen bonds, there existed some question as to which donor-acceptor pairing of the molecules was the lowest energy form. This question is further emphasized by the ambiguity and variety present in previous experimental and computational results. Transitions arising from the methyl torsional A state were assigned for the various isotopomers. The fit of the structure to the rotational constants gave unambiguous confirmation that the only conformation observed in the supersonically cooled molecular beams corresponded to a water-donor, methanol-acceptor complex.

Bibliography

[1] M. Matsumoto, Y. Takaoka, and Y. Kataoka. Liquid-Vapor Interface of Water-Methanol Mixture. I. Computer Simulation. *J. Chem. Phys.*, 98:1464, 1993.

[2] H. Tanaka, J. Walsh, and K.E. Gubbins. Structure of Water-Methanol Binary Mixtures: Role of the Water-Water Interaction. *Mol. Phys.*, 76:1221, 1992.

[3] M.J. Elrod, R.J. Saykally, A.R. Cooper, and J.M. Hutson. Nonadditive Intermolecular Forces from the Spectroscopy of van der Waals Trimers—Far-Infrared Spectra and Calculations on Ar_2–DCl. *Mol. Phys.*, 81:579, 1994.

[4] L. Dore, R.C. Cohen, C.A. Schmuttenmaer, K.L. Busarow, M.J. Elrod, J.G. Loeser, and R.J. Saykally. Far-infrared Vibration-Rotation-Tunneling Spectroscopy and Internal Dynamics of Methane-Water—a Prototypical Hydrophobic System. *J. Chem. Phys.*, 100:863, 1994.

[5] S.G. Lias, F.J. Liebman, and R.D. Levin. Evaluated Gas-Phase Basicities and Proton Affinities of Molecules—Heats of Formation of Protonated Molecules. *J. Phys. Chem. Ref. Data*, 13:695, 1984.

[6] J.T. Hougen and N. Ohashi. Tunneling Splitting Patterns in Two Forms of the Methanol-Water Dimer. *J. Mol. Spec*, 159:363, 1993.

[7] F.C. De Lucia, E. Herbst, and T. Anderson. The Analysis of the Rotational Spectrum of Methanol to Microwave Accuracy. *J. Mol. Spect.*, 134:395, 1989.

[8] N. Bakkas, Y. Bouteiller, A. Bouteiller, J.P. Perchard, and S. Racine. The Water-Methanol Complexes. I. A Matrix Isolation Study and an *Ab Initio* Calculation on the 1-1 Species. *J. Chem. Phys.*, 99:3335, 1993.

[9] N. Bakkas, Y. Bouteiler, A. Bouteiller, J.P. Perchard, and S. Racine. The Water-Methanol Complexes. Matrix Induced Structural Conversion of the 1-1 Species. *Chem. Phys. Lett.*, 232:90, 1995.

[10] S. Kim, M.S. Jhon, and H.A. Scheraga. Analytic Intermolecular Potential Functions from *Ab Initio* SCF Calculations of Energies between CH_4, CH_3OH, CH_3COOH, and CH_3COO^- and Water. *J. Phys. Chem.*, 92:7216, 1988.

[11] F. Huisken and M. Stemmler. On the Structure of the Methanol-Water Dimer. *Chem. Phys. Lett.*, 180:332, 1991.

[12] J.E. Del Bene. Theoretical Study of Open Chain Dimers and Trimers Containing CH_3OH and H_2O. *J. Chem. Phys.*, 55:4633, 1971.

[13] Y.-C. Tse, M.D. Newton, and L.C. Allen. Theoretical Study of the O—Methyl Substitution Effect in —OH$\cdots$O Hydrogen Bonds. *Chem. Phys. Lett.*, 75:350, 1980.

[14] G. Bolis, E. Clementi, D.H. Wertz, H.A. Scheraga, and C. Tosi. Interaction of Methane and Methanol with Water. *J. Phys. Chem.*, 105:355, 1983.

[15] Sakae Suzuki. *Towards a More Quantitative Understanding of Intermolecular Interactions: Biologically Significant Intermolecular Clusters.* PhD thesis, California Institute of Technology, 1996.

[16] F.J. Lovas, R.D. Suenram, G.T. Fraser, C.W. Gillies, and J. Zozom. The Microwave Spectrum of Formamide-Water and Formamide-Methanol Complexes. *J. Chem. Phys.*, 88:722, 1988.

[17] F.J. Lovas, S.P. Belov, J. Ortigoso, and R.D. Suenram. The Microwave Spectrum and Structure of the CH_3OH-CO Dimer. *J. Mol. Spect.*, 167:191, 1994.

[18] F.J. Lovas, S.P. Belov, M.Y. Tretyakov, W. Stahl, and R.D. Suenram. The a-Type $K = 0$ Microwave Spectrum of the Methanol Dimer. *J. Mol. Spect.*, 170:478, 1995.

[19] R.D. Suenram, F.J. Lovas, G.T. Gillies, J.Z. Gillies, and M. Onda. Microwave Spectrum, Structure, and Electric-Dipole Moment of Ar-CH_3OH. *J. Mol. Spect.*, 137:127, 1989.

[20] P. Cope, A.C. Legon, and D.J. Millen. The Microwave Spectrum and Geometry of the Methanol-Hydrogen Chloride Dimer. *Chem. Phys. Lett.*, 112:59, 1984.

[21] H.B. Thompson. Calculation of Cartesian Coordinates and Their Derivatives from Internal Molecular Coordinates. *J. Chem. Phys.*, 47:3407, 1967.

[22] R.H. Schwendeman. *Critical Evaluation of Chemical and Physical Structural Information.* National Academy of Sciences, Washington, D.C., 1972.

[23] M.D. Harmony, V.W. Laurie, R.L Kuczkowski, R.H. Schwendeman, D.A. Ramsay, F.J. Lovas, W.J. Lafferty, and A.G. Maki. Molecular Structure of Gas-Phase Polyatomic Molecules Determined by Spectroscopic Methods. *J. Phys. Chem. Ref. Data*, 8:619, 1979.

[24] J.A. Odutola and T.R. Dyke. Partially Deuterated Water Dimers: Microwave Spectra and Structure. *J. Chem. Phys.*, 72:5062, 1980.

Chapter 6 Comparisons, Conclusions, and Future Directions

The vdW complexes discussed in this thesis span a wide array of binding energies, quantum mechanical phenomena, and chemical interactions, and it is thus challenging to make meaningful comparisons among them and draw unifying conclusions from their study. For example, the $Ar\cdots H_2O$ complex, used as a prototype for the work on other complexes, has a binding energy of 0.41 kcal/mol [1], while $H_3N\cdots H_2O$ has an estimated binding energy of 5.74 kcal/mol [2]. This 14-fold difference in bond strength is equivalent to the difference in energy between the dinitrogen and disodium molecules. One would not choose to use the results of experiments on Na_2 as a prediction of N_2 behavior under similar conditions even though they are both covalently-bonded, closed shell, homonuclear diatomics—primarily because there exist a host of better analogs. These analogs do not exist in great numbers, however, for vdW complexes, and comparisons must be made over much wider differences. As discussed in the first two chapters, technical obstacles have limited the high-resolution study of these complexes until recently, and the quantity of isolated complexes studied numbers a few hundred at most. Moreover, the number of complexes studied at energies which access the intermolecular vibrational modes, which define much of the IPSs, is less by an order of magnitude. The foregoing comments are not meant as discouragement, but simply as a caveat that these comparisons and conclusions are preliminary and that much work remains ahead before a thorough understanding of vdW bonding becomes quantifiable.

The complexes chosen for discussion in this thesis focus more narrowly on a subset of water-containing vdW dimers whose strongest interactions occur in a hydrogen-bonded geometry. The importance of studying these interactions and extending individual IPSs to larger systems have been covered in detail in the introductions to

previous chapters. The VRT spectra and analyses of several other water-containing dimers have been reported, and together with the present data, create an initial basis for examining the array of vdW interactions with water. Primary among these is water dimer itself, which was cited in Section 1.3. Among these reports are on-going VRT studies by Saykally and coworkers, begun by Pugliano, to understand the dynamics of water-water interactions [3, 4, 5, 6]. The most fruitful studies to date have been with clusters of D_2O, since the intermolecular vibrational modes for these isotopomers lie at lower, more accessible frequencies than those of the H_2O-containing species; the Blake lab has contributed to this study as well [7].

The three other FIR investigations of water-containing vdW dimers involve binding to hydrocarbon molecules, and the results of these studies provide the simplest molecular models of hydrophobic interactions. Dore *et al.* and Steyert *et al.* have examined complexes with methane and propane, respectively [8, 9, 10]. The methane-water complex was found to behave similarly to $Ar\cdots H_2O$, in that both subunits experience near free-rotation about their individual symmetry axes; however, because of the coupling of these internal rotations, the specific VRT origins of the spectra remain largely intractable. As with $N_2\cdots H_2O$ and $OC\cdots H_2O$, the propane-water complex revealed that the existence of even small, permanent dipole and quadrupole moments can dominate the long-range attractive forces of Equation (1.1), and the resulting anisotropy gives a definite minimum energy conformation. Steyert *et al.* found strong evidence for a hydrogen-bonded structure that has the water hydroxyl group forming a bond to the methylene carbon with all heavy atoms in a coplanar configuration. The FIR spectra, centered around 20 cm^{-1}, are consistent with a torsional motion of the free hyroxyl bond about the bound one. Lastly, Suzuki *et al.* have studied the complex of benzene-water, which probes the important interactions of hydroxl groups with aromatic π-electrons [11, 12]. Again, a hydrogen-bonded minimum is favored with the O—H bond pointed near normal to the benzene plane. However, the hydrogen bond acceptor in this case is not an atom or lone pair, but rather a delocalized system of six electrons spread over approximately 5 $Å^2$. This leads to low energy, large amplitude motions of the water subunit relative to the benzene plane.

Table 6.1: Estimated intermolecular stretching frequencies (cm^{-1}) and calculated *ab initio* binding energies (kcal/mol) for water-containing, hydrogen-bonded dimers.

	$\nu_{vdW} = (4B^3/D_J)^{\frac{1}{2}}$	D_e
$Ar\cdots H_2O$	35.8	0.4
$CH_4\cdots H_2O$	55.0	
$(CH_3)_2(H)_2C\cdots H_2O$	69.9	
$N_2\cdots H_2O$	50.8	1.23
$OC\cdots H_2O$	67.3	1.87
$C_6H_6\cdots H_2O$	78.8	1.9
$(D_2O)_2$	139.8	5.4
$H_3N\cdots H_2O$	171.5	5.74

The level of detail available in the study of these complexes is largely disparate. One unifying comparison can be made with their estimated vdW stretching frequencies, derived by extension of the Morse potential to rotational distortion, from their determined B and D_J constants:

$$\nu_{vdW} = \sqrt{\frac{4B^3}{D_J}}. \tag{6.1}$$

Table 6.1 summarizes these results. Equation (6.1) is a first order approxiamtion and typically overestimates the true frequency by 10–20%. The only experimentally determined value of ν_{vdW} is for $Ar\cdots H_2O$, 30.4 cm^{-1}. The resulting values for $N_2\cdots H_2O$ and $OC\cdots H_2O$ are questionably low, perhaps because of their unique near linear geometries, especially in light of the calculations of Sadlej *et al.* presented in Table 3.19. As the stretching frequency is proportional to the intermolecular bond strength, one can see that the trend shown in Table 6.1 corresponds well with estimates of relative bond strength made from electrostatic arguments. Interesting is the relatively strong bond formed between water and benzene, which calls into question the broad generalizations made about hydrophobic interactions. As noted by the authors of reference [11], aromatic groups have been shown to function as conduits for polar and ionic species in biological systems. Also shown are reliably determined *ab initio* values for D_e, with the exception of that for $Ar\cdots H_2O$, which has also been empirically determined.

Table 6.2: Tunneling splittings (GHz) and barrier heights (cm^{-1}) for water-containing clusters.

	Tunneling splitting	Barrier height
$Ar\cdots H_2O$		47
$N_2\cdots H_2O$	31.4	130
$OC\cdots H_2O$	16.7	225
$H_3N\cdots H_2O$	0.113	704

A phenomenon common to the FIR studies of clusters discussed in this thesis is quantum mechanical tunneling of the water hydrogens across a potential barrier which separates two chemically equivalent conformations. Table 6.2 summarizes these results in terms of the observed tunneling frequency as well as the height of the determined barrier. Note that in $Ar\cdots H_2O$, the pathway of the tunneling is largely about the water b-axis, while for the others tunneling was shown to occur about the water c-axis. Also, in $Ar\cdots H_2O$ there is no real tunneling, *per se*, as the zero point energy of the complex is above the barrier. Here, the barrier was determined from the global AW2 IPS. The tunneling splittings are another gauge of binding strength, and the trend is very apparent as the tunneling motion is nearly quenched—but not absent—in the strongly-bound $H_3N\cdots H_2O$ complex. As the molecule accesses higher energy states within the tunneling potential, the response of the tunneling splittings is an indication of the IPS rotational anisotropy. In the $OC\cdots H_2O$ and $H_3N\cdots H_2O$ dimers, for example, the tunneling splittings in the ~ 20 cm^{-1} $K = 1$ level is virtually unchanged from those of the ground state; more weakly bound and more isotropic $N_2\cdots H_2O$ experienced significant perturbations in tunneling splitting upon rotational excitation. Finally, we recall also from $N_2\cdots H_2O$ that, along with intermolecular vibrations, tunneling is not always a separable degree of freedom for these complexes.

As stated in Chapter 1, the overriding goal of all of these studies is to obtain useful and complete IPSs for vdW clusters which can in turn be incorporated into larger modeling routines. So where do we stand in achieving this goal? The three-dimensional AW1 and AW2 long stood (five years) as the most complex and complete

IPSs achieved; recently, a four-dimensional semi-empirical IPS has been calculated for $(HCl)_2$ [13]. Researchers seeking to extend AW2-like treatment to other complexes have faced a three-fold challenge. First, as more strongly-bound clusters are studied, the intermolecular modes are both higher in energy and more widely distributed in frequency. The nascent FIR technology described in this thesis has more limited coverage at higher frequencies, and coupled with slow scanning rates, this means that obtaining complete intermolcular vibrational spectra is a painstaking process. Morever, some modes lie in the 200–400 cm^{-1} nether region of the electromagnetic spectrum which has unproven coverage by FIR laser sideband spectrometers or Pb salt diode laser systems. Second, the recorded spectra present challenges in assignment. Because of the extreme anharmonicity of IPSs, the spectra often require tailor-made Hamiltonians to treat their eccentricities, such as the coupling of N_2 and H_2O tunneling modes in $N_2 \cdots H_2O$ and the coupling of internal rotor states in $CH_3OH \cdots Ar$, $CH_4 \cdots H_2O$, and $H_3N \cdots H_2O$. Useful structural rotational constants for excited vibrational states must first be decoupled from tunneling and internal rotor effects. Third, the degree of computational complexity in fitting IPSs to obtained VRT data scales as ν_{im}^3 or ν_{im}^4, meaning that more efficient algorithms are required.

Surely if the field is to progress beyond the rate of a handful of IPSs per decade, new techniques and methods must be developed. Advances in the Blake lab and elsewhere with GaAs-based photomixing of near-IR diode lasers to produce tunable FIR light are very promising. Recent results indicate that spectrometers based on these sources will have continuous scanning ranges of over 200 cm^{-1}, with power levels equivalent to or exceeding currently attainable FIR-MW sideband outputs. When employed, these systems could reduce current data acquisition times on the order of 10- to 50-fold, while the reduction in monetary investment will make this technology accessible to more researchers. With this expected increase in data availability, more practical approaches to data analysis will be needed as well. Currently, because of the dearth of available data, spectra are analysed in detail to extract as much information as possible. However, if the IPS production process is to scale-up, time consuming tailor-fit analyses of individual complexes must be streamlined. A more

practical approach might be to use easily-obtained MW rotational constants and dipole moments to fit the bottom of the IPS while fitting the higher energy portions with intermolecular vibrational frequencies alone, *i.e.*, without employing excited state rotational constants. At the current level of computational sophistication, these vibrational frequencies should be sufficient to constrain the important features of the IPS. Lastly, computational methods as well must be made more broadly applicable to the problem. The recent advances with DMC methods cited in Chapter 3 show great promise of accomodating this wealth of VRT information. These codes are already easily applied to ground state data, and the extension of these methods to vibrationally excited states promises to yield a robust supply of new and useful IPSs.

Bibliography

[1] R.C. Cohen and R.J. Saykally. Determination of an Improved Global Potential Energy Surface for Ar–H_2O from Vibration-Rotation-Tunneling Spectroscopy. *J. Chem. Phys.*, 98:6007, 1993.

[2] Z. Latajka and S. Scheiner. Structure, Energetics, and Vibrational Spectrum of $H_3N \cdots HOH$. *J. Phys. Chem.*, 94:217, 1990.

[3] N. Pugliano and R.J. Saykally. Measurement of the ν_8 Intermolecular Vibration of $(D_2O)_2$ by Tunable Far Infrared-Laser Spectroscopy. *J. Chem. Phys.*, 96:1832, 1992.

[4] N. Pugliano and R.J. Saykally. Measurement of Quantum Tunneling between Chiral Isomers of the Cyclic Water Trimer. *Science*, 257:1937, 1992.

[5] N. Pugliano, J.D. Cruzan, J.G. Loeser, and R.J. Saykally. Vibrational and K'_a Dependencies of the Multidimensional Tunneling Dynamics in the 82.6 cm^{-1} Intermolecular Vibration of Water Dimer-d_4. *J. Chem. Phys.*, 98:6600, 1993.

[6] K. Liu, J.G. Loeser, M.J. Elrod, B.C. Host, J.A. Rzepiela, N. Pugliano, and R.J. Saykally. Dynamics of Structural Rearrangements in the Water Trimer. *J. Am. Chem. Soc.*, 116:3507, 1994.

[7] S. Suzuki and G.A. Blake. Pseudorotation in the D_2O Trimer. *Chem. Phys. Lett.*, 229:499, 1994.

[8] L. Dore, R.C. Cohen, C.A. Schmuttenmaer, K.L. Busarow, M.J. Elrod, J.G. Loeser, and R.J. Saykally. Far-infrared Vibration-Rotation-Tunneling Spectroscopy and Internal Dynamics of Methane-Water—a Prototypical Hydrophobic System. *J. Chem. Phys.*, 100:863, 1994.

[9] D.W. Steyert, M.J. Elrod, R.J. Saykally, F.J. Lovas, and R.D. Suenram. Fourier Transform Microwave Spectrum of the Propane-Water Complex: a Prototypical Water-Hydrophobe System. *J. Chem. Phys.*, 99:7424, 1993.

[10] D.W. Steyert, M.J. Elrod, and R.J. Saykally. Far-infrared Laser Vibration-Rotation-Tunneling Spectroscopy of the Propane-Water Complex: Torsional Dynamics of the Hydrogen Bond. *J. Chem. Phys.*, 99:7431, 1993.

[11] S. Suzuki, P.G. Green, R.E. Bumgarner, S. Dasgupta, W.A. Goddard, and G.A. Blake. Benzene Forms Hydrogen-bonds with Water. *Science*, 257:5072, 1992.

[12] Sakae Suzuki. *Towards a More Quantitative Understanding of Intermolecular Interactions: Biologically Significant Intermolecular Clusters.* PhD thesis, California Institute of Technology, 1996.

[13] M.J. Elrod and R.J. Saykally. Determination of the Intermolecular Potential Energy Suface for $(HCl)_2$ from Vibration-Rotation-Tunneling Spectra. *J. Chem. Phys.*, 103:933, 1995.